Plasmofluidic Single-molecule Surface-enhanced Raman Scattering and Dynamic Assembly of Nanostructures

A thesis

submitted in partial fulfilment of the requirements

for the degree of Doctor of Philosophy

by

Partha Pratim Patra

(Reg ID: 2011-3129)

INDIAN INSTITUTE OF SCIENCE EDUCATION AND RESEARCH,

PUNE

Dedicated to

my parents

and my wife Sreyashi

CERTIFICATE

Certified that the work incorporated in the thesis entitled 'Plasmofluidic Single-molecule Surface-enhanced Raman Scattering and Dynamic Assembly of Nanostructures' submitted by **Partha Pratim Patra** was carried out by the candidate, under my supervision. The work presented here or any part of it has not been included in any other thesis submitted previously for the award of any degree or diploma from any other University or institution.

Pune
Date: August 16, 2016

(Dr. G V Pavan KUMAR)
Thesis Supervisor

DECLARATION

I declare that this written submission represents my research work in my own words and where others' ideas or works have been included, I have adequately cited and referenced the original sources. I also declare that I have adhered to all principles of academic honesty and integrity and have not misrepresented or fabricated or falsified any idea/data/fact/source in my submission. I understand that violation of the above will be cause for disciplinary action by the Institute and can also evoke penal action from the sources which have thus not been properly cited or from whom proper permission has not been taken when needed.

Pune
August 16, 2016

(Partha Pratim Patra)
ID: 20113129

“हिरण्मयेन पात्रेण सत्यस्यापिहितं मुखम्।
तत्त्वं पूषन्नपावृणु सत्यधर्माय दृष्टये॥”

“Hiranmayena patrena satyasyapihitam mukham,
tattvam pusannapavrnu satyadharmaya drstave.”

Isha Upanishad - Shloka 15

Truth lies concealed by golden vessel.
Do thou o Sun!
Open the entrance of that cover
So as the Truth you so concealed
be visible to me,
a devotee, who by nature is truthful,
in the light of your illuminating Grace.

Abstract

Single molecule detection and characterization is essential in several realms of science and technology to understand fundamental aspects of molecular dynamics. Surface-enhanced Raman scattering (SERS) has emerged as a unique and powerful technique with single molecule sensitivity and chemical specificity. The heart of this technique relies on the enhanced electromagnetic (EM) field from localized surface plasmon polariton (L-SPP), coupled oscillation of light and free electron at the surface of a metal nanostructure. Thus modulating the SPP towards maximum field intensity is the most important aspect to harness single molecule surface-enhanced Raman scattering (SMSERS). Also, to make this technique adaptable in various applications, the study of SMSERS involving various nanostructures in suitable microscopy system is an imperative prerequisite. The conventional fluid phase SMSERS experiments are commonly performed by using chemically aggregated Ag colloidal nanoparticles in focused field microscopy. Herein we investigate the two aspects of plasmofluidic (i.e. plasmonic field in fluidic environment) single-molecule SERS, (i) introducing new type of nanostructures to SMSERS and (ii) employing evanescent-wave microscopy for SMSERS. We further explore the plasmofluidic field to equip for patterned assembly of nanostructures.

First, we shall discuss on the single-molecule SERS sensitivity of Ag@Au bimetallic nanostructures in fluid phase with conventional focused field microscopy technique. We also refer these nanostructures to befit ultra-sensitive trace analysis.

Secondly, we shall dwell on how to harness evanescent-wave excitation to create electromagnetic hot-spots by assembling colloidal nanoparticles without any chemical means and to detect single molecule SERS signals with Ag@Au nanoparticles.

Lastly, we shall present that how the extension of above said technique can lead to a preamble of reconfigurable dynamic lithography of plasmonic nanostructures at metal fluid interface.

List of Publications

Included in thesis:

- Single Molecule Surface Enhanced Raman Scattering Sensitivity of Ag-core Au-shell Nanoparticles: Revealed by Bi-analyte Method; **Partha Pratim Patra** and G.V. Pavan Kumar*; ***The Journal of Physical Chemistry Letters*****, 4, 1167-1171 (2013)**.

- Plasmofluidic Single-Molecule Surface Enhanced Raman Scattering from Dynamic Assembly of Plasmonic Nanoparticles; **Partha Pratim Patra**, Rohit Chikkaraddy, Ravi P.N. Tripathi, Arindam Dasgupta, and G. V. Pavan Kumar*; ***Nature Communications*****, 5, 4357 (2014).**

- Large scale dynamic assembly of metal nanostructures in plasmofluidic field; **Partha Pratim Patra**, Rohit Chikkaraddy, Sreeja Thampi, Ravi P. N.Tripathi and G.V. Pavan Kumar*; ***Faraday Discussions*****,186, 95-106 (2016).**

Not included in thesis:

- Surfactant-free synthesis of anisotropic gold nanostructures: can dicarboxylic acids alone act as shape directing agents?; DV Ravi Kumar, SR Kumavat, VN Chamundeswari, **Partha Pratim Patra**, AA Kulkarni, BLV Prasad*; *RSC Advance*, 3 (44), 21641-21647 (2013).

- Subwavelength propagation and localization of light using surface plasmons: A brief perspective; G. V. Pavan Kumar*, Danveer Singh, **Partha Pratim Patra** and Arindam Dasgupta; *Pramana - Journal of Physics* (invited review article, NLS-21 issue), 82, 59-70 (2014).

List of Publications

- Redox-Induced Photoluminescence of Metal-Organic Coordination Polymer Gel; Barun Dhara, **Partha P. Patra**, P. K. Jha, S. V. Jadhav, G.V. Pavan Kumar, N. Ballav; *The Journal of Physical Chemistry C*,118 ,19287-19293 (2014).

- Geometry dependent anti-Stokes SERS radiation patterns from gold nanorod dimers; Aswathy V.G., **Partha Pratim Patra** and G. V. Pavan Kumar*; *Journal of Optics (IoP)*, 17, 114011 (2015).

- Directional emission of light from organic exciton-polariton mesowire in active and passive regimes; Ravi P.N. Tripathi, Arindam Dasgupta, Rohit Chikkaraddy, **Partha P. Patra**, Adarsh Vasista and G.V. Pavan Kumar*, *Journal of Optics(IoP)*, 18 (6), 065002 (2016).

- Plasmon-controlled Excitonic Emission from Vertically-Tapered Organic Nanowires; Rohit Chikkaraddy, **Partha P. Patra**, Ravi Tripathi, Arindam Dasgupta and G.V. Pavan Kumar*; *RSC Nanoscale, 8, 14803-14808 (2016)*

Acknowledgements

Pursuing PhD is not a very smooth journey; I could not have made it without the help and constant support from a few people. Today in the verge of the completion of my PhD, I would like to express my gratitude to all of them.

First of all I thank my supervisor, Dr. G V Pavan Kumar for giving me a chance to work with him. He has always been very supportive and encouraging to me. The immense freedom in the lab he has given, has helped me to build up an independent thinking capability.

The next person in the lab who taught me a lot is my senior and one of my best friends, (now) Dr. Arindam Dasgupta. He is a very uniquely nice person with down-to-earth nature. Not only in the lab but also in my personal life, for either joy or sorrow, he has always been there for me.

Another important person in my PhD life is our former undergraduate student Rohit Chikkaraddy. Though he was much younger to me I learnt many things from him. While working or discussing with him, in every moment it reminds me that, 'the whole world globes itself in a drop of dew'.

In addition to Arindam and Rohit, for the direct or indirect contribution to my PhD work, I wish to thank all my former and present lab members, Danveer Singh, Sreeja Thampi, Aswathy V. G., Ravi Tripathi, Adarsh Vasishta, Deepak Sharma, Dr. Debrina Jana, Mohit Raghuwansi, Sruthi Polali, Sreyash Tandon, Anjusha V. S., Abhijit Nair and Rajath Sawant. All of them together made a very nice and pleasant working environment in the lab.

I also acknowledge the members of my research advisory committee (RAC), Dr Nirmallya Ballav and Dr Shivaprasad Patil for their critical suggestions for my work.

Life during PhD would not have been lively without my hostel-friends, Abhik Mullick, Koushik Karmakar, Barun Dhara, Sudeb Ghosh, Avishek Karmakar, Sunil Kumar,

Supratik Sarkar and Maidul Islam.

I also thank my B.Sc. friend Suman Ray and M.Sc. friends Ritesh Haldar, Sukanta Mondal, Purnim Dhar, Akshay Dhayagude and Ashwini Thorat for motivating me towards research.

I acknowledge Ministry of Human Resource Development (MHRD), India, Department of Science and Technology (DST), India and IISER Pune for providing financial support during the period of research.

Last but most importantly, I would like to acknowledge my parents, parents-in-law, Mr. and Mrs. Pakrasi, elder sister, brother-in-law and my wife for their love, support and encouragement. Especially I thank my father who is my first teacher and the ideal of my life. And I thank Sreyashi Dasgupta for inspiring me in every step of my life.

Contents

Abbreviations

ATIR	attenuated total internal reflection
CCD	charge-coupled device
CSNP	core-shell nanoparticle
DC	direct current
EG	ethylene glycol
EM	electromagnetic
FDTD	finite difference time domain
HOMO	highest occupied molecular orbital
HPF	high pass filter
LASER	light amplification by stimulated emission of radiation
LUMO	lowest unoccupied molecular orbital
LR	lightning rod
L-SPP	localised surface plasmon polariton
LSPR	localised surface plasmon resonance
MPCA	modified principal component analysis
MW	molecular weight
NA	numerical aperture
NB	nile blue
Nd:YAG	neodymium yttrium aluminum garnet
NP	nanoparticle
NW	nanowire
OBL	objective lens
PCA	principal component analysis
PML	perfectly matched layer
PP	plasmon polariton
P-SPP	propagating surface plasmon polariton

Abbreviations

PVP	polyvinylpyrrolidone
RI	refractive index
RS	Raman scattering/spectroscopy
R6G	rhodamine-6G
SEM	scanning electron microscopy
SERS	surface-enhanced Raman scattering/spectroscopy
SERRS	surface-enhanced resonance Raman scattering/spectroscopy
SMSERS	single-molecule surface-enhanced Raman scattering/spectroscopy
SP	surface plasmon
SPP	surface plasmon polariton
TEM	transmission electron microscopy
TIR	total internal reflection
TM	transverse magnetic
UV	ultraviolet
2-NAT	2-naphthalene thiol

Chapter 1

Introduction

Single molecule detection and characterization is essential in several realms of science and technology to understand fundamental aspects of molecular dynamics. Surface-enhanced Raman scattering (SERS) has emerged as a unique and powerful technique with single molecule sensitivity and chemical specificity. The heart of this technique relies on the enhanced electromagnetic (EM) field from localized surface plasmon polariton (L-SPP), free electron oscillation on the surface of a metal nanostructure. Thus modulating the SPP towards maximum field intensity is the most important aspect to harness single molecule surface enhanced Raman scattering (SMSERS). Also to make this technique adaptable in various applications, the study of SMSERS involving various nanostructures in suitable microscopy system is an imperative prerequisite. In this thesis we shall mainly present the works towards the development of single-molecule SERS technique. However to provide a complete perspective we shall start from the beginning of this journey, the Raman scattering

1.1 Introduction to Raman Effect

Having been first observed in 1928, 'the new type of secondary radiation'[1] or 'the new radiation'[2] had created a history of its own in 1930 by achieving the Nobel prize and as well as opened the door to a new realm of research, 'the Raman Scattering' after the name of the discoverer. The phenomenon was first noticed with toluene followed by many other liquids (more than 70 samples) and the molecular interaction with light

had been assumed to be the plausible origin of such scattering. Till today Raman Effect has had a long-travelled path with many aspects in terms of the developments and applications.

The origin of Raman Effect is itself a vast area of research and beyond the scope of our discussion. In a very simplistic way, this effect can be illustrated as a scattering phenomenon due to light-matter interaction. When a beam of radiation interacts with matter, the scattered radiation consists almost entirely of the incident frequency (Rayleigh scattering) and in addition, certain discrete radiation of higher and lower frequency originates; this is referred to as Raman scattering. Raman scattering is actually the outcome of an inelastic light-matter interaction. For a specific example, when light (photon) interacts with a molecule, energy is exchanged; and according to the natural law, the total energy of the photon and molecule must be conserved. Thus, we can write,

$$\Delta E = E - E' = h(\nu' - \nu) \qquad \text{(Eq 1.1)}$$

where, ν and ν' are the frequencies of incident and scattered light respectively and similarly, E and E' are the initial and final energies of the scattered molecule.
On the basis of this equation the scattering process can be classified into three types schematically as shown in figure 1.1;
(i) **Rayleigh Scattering**, if $\nu = \nu'$, i.e. $\Delta E = 0$
(ii) **Raman Stokes Scattering**, if $\nu > \nu'$, i.e. $\Delta E < 0$
(iii) **Raman anti-Stokes Scattering**, if $\nu < \nu'$, i.e. $\Delta E > 0$

Now, we try to look into the phenomenon in the classical concept of its basics i.e. polarizability of a molecule. When a molecule experiences an electric field, it gets distorted due to the charge displacement. The separation of the charge centres causes an induced electric dipole moment, and such a molecule is said to be polarized. If E is applied electric field and μ being the magnitude of induced electric dipole moment, we may write,

$$\mu = \alpha E \qquad \text{(Eq 1.2)}$$

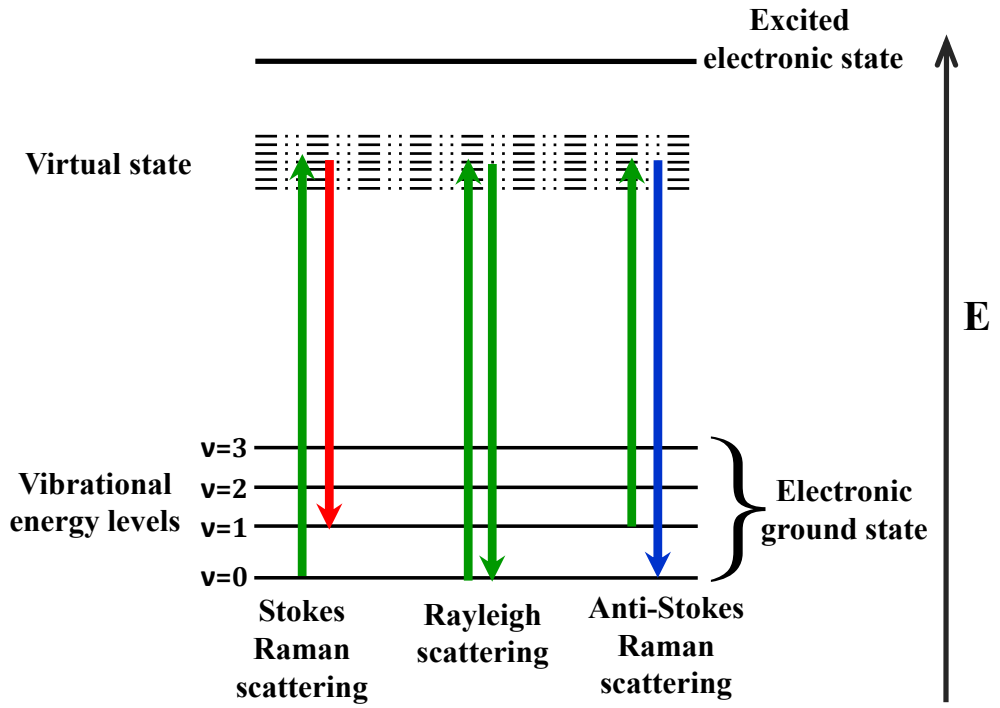

Figure 1.1: Simplified Jablonski diagram for schematic illustration of Raman scattering.

If a molecule interacts to an excitation beam of frequency ν, the electric field experienced by the molecule fluctuates as,

$$E = E_0 cos(2\pi\nu t) \qquad \text{(Eq 1.3)}$$

Therefore, the induced dipole also undergoes oscillation of the same frequency ν, i.e.

$$\mu = \alpha E = \alpha E_0 cos(2\pi\nu t) \qquad \text{(Eq 1.4)}$$

In addition, if the molecule undergoes any internal motion that changes the polarizability periodically, then the dipole oscillation couples to the oscillation of the molecular motion (i.e. rotation or vibration). In such a case, suppose a molecular vibrational frequency v causes the polarizability change then we can write,

$$\alpha = \alpha_0 + \left(\frac{\delta\alpha}{\delta q}\right)_0 q + \left(\frac{\delta^2\alpha}{\delta q^2}\right)_0 q^2 + ... \qquad \text{(Eq 1.5)}$$

where, α_0 is the equilibrium value of the polarizability tensor element, q is the displacement and

$$q = q_0 cos(2\pi vt) \tag{Eq 1.6}$$

Thus,

$$\mu = \alpha_0 E + \alpha' E + \alpha'' E + ... \tag{Eq 1.7}$$

here, α' denotes $(\delta\alpha/\delta q)_0$.

Now, combining equation Eq 1.3, Eq 1.6 and Eq 1.7 and neglecting the α'' term we get,

$$\mu = \alpha_0 E_0 cos(2\pi\nu t) + \alpha' q_0 cos(2\pi vt) E_0 cos(2\pi\nu t) \tag{Eq 1.8}$$

$$\Rightarrow \mu = \alpha_0 E_0 cos(2\pi\nu t) + \frac{1}{2}\alpha' q_0 [cos2\pi(\nu + v) + cos2\pi(\nu - v)] \tag{Eq 1.9}$$

Finally,

$$\mu = \alpha_0 E_0 cos(2\pi\nu t) + \frac{1}{2}\alpha' q_0 [cos2\pi(\nu + v)] + \frac{1}{2}\alpha' q_0 [cos2\pi(\nu - v)] \tag{Eq 1.10}$$

The first term of the equation Eq 1.10 signifies the elastic Rayleigh scattering with no energy exchange whereas the other two terms refer to the inelastic Raman scattering; second term accounts for anti-Stokes and third term for Stokes lines. So from the above discussion, it is evident that Raman scattering is a spontaneous process that gives spectroscopic insight of a material without requiring material-specific excitation (unlike fluorescence process) and thus Raman scattering technique can be used to probe various aspects in many disciplines of science and technology. Of late, with the help of the state-of-the-art microscopy systems along with LASER, this has emerged as one of the most powerful techniques in the field of optical spectroscopy and has applications almost in 'every' field of science, technology and industry.

Despite having such calibre, the normal Raman scattering technique cannot play much of a role beyond structure-analysis tool due to very low 'scattering cross section' ($\sim 10^{-29}$ cm^2)[3, 4]. Thus, ultra-sensitive trace analysis, light matter interaction at single particle/molecule level and many other fundamental aspects cannot be unveiled by normal Raman scattering. And hence, there was an imperative need to develop interest

in various modifications to Raman scattering both in linear and non-linear regime[5, 6]. One of the very important developments in Raman scattering technique to breach the weak signal issue is through Surface-enhanced Raman scattering (SERS).

1.2 Surface-enhanced Raman Scattering (SERS)

Surface-enhanced Raman scattering is about the amplification of Raman scattering of the molecules by several orders of magnitude. When a molecule in close proximity to a nanometallic surface interacts with light then the intensity of the Raman scattering of the molecule increases enormously. This phenomenon was first observed by Fleischmann et al. in 1974 for pyridine molecules adsorbed on electrochemically roughened silver electrode[7]. Though initially it was believed that the enhancement is due to the increased surface area but later on, Van Duyne's group[8] and Creighton's group[9] independently predicted that some additional factors, other than large surface area must be behind such huge signal-enhancement. King, Duyne and Schatz in 1978 first proposed the electromagnetic field enhancement theory of SERS[10, 11]. There are several mechanisms proposed for SERS enhancement which can be classified mainly as electromagnetic enhancement and chemical enhancement theory[12–15]. An overall scenario

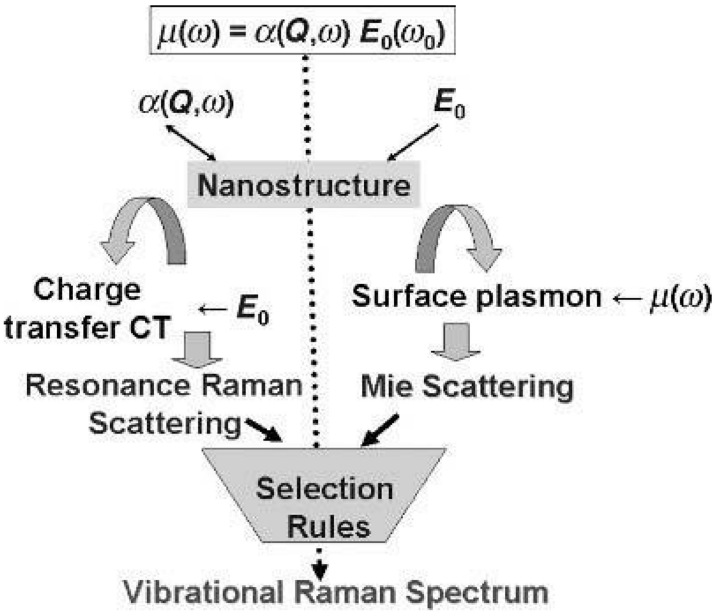

Figure 1.2: Flow-chart showing various conributions to the SERS enhancement factor[3].

of the SERS enhancement mechanism is nicely schematized in figure 1.2[3].

1.2.1 Electromagnetic enhancement

The heart of the electromagnetic theory of SERS is based on 'surface plasmon polariton (SPP)'[17–20], a very unique consequence of the light-metal interaction. When light interacts with the free-electrons (plasma) of a metal, they start oscillating with a distinct frequency and this free-electron oscillation is the origin of the plasmon polariton (PP). Now if the metallic substrate happens to be a nano-object then plasmon polaritons are located at the surface of the metal and these are termed as surface plasmon polaritons. Surface plasmon polaritons usually exist mainly in two varieties; one is the localised surface plasmon polariton (L-SPP) and other is the propagating surface plasmon polariton (P-SPP).

Localised surface plasmon polariton (L-SPP):

When the interaction of light with a metal nanostructure happens so that the SPPs are confined to a small volume of the nanostructure then these are termed as localised surface plasmon polaritons. A simple case of L-SPP can be described with the example of a metallic nanosphere. For a nanosphere with diameter very small compared to the wavelength (i.e. $d << \lambda$), the free-electron oscillates in phase with the interacting light. This results in the polarization of surface charge around the nanosphere leading

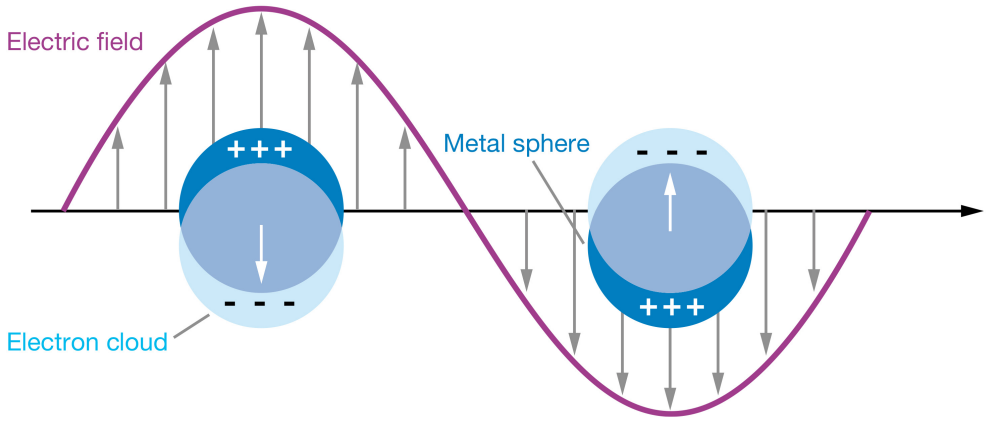

Figure 1.3: Schematic of localised surface plasmon polariton (L-SPP) in a nanometallic sphere[16].

to a Coulombic restoring force between the counter charges. Thus, an inherent oscillation of the conduction electrons originates with a distinct frequency and the energy of the oscillation remains confined at the surface, hence is called localized *surface* plasmon polariton (shown in figure 1.3). In a certain case if the frequency of the incident light matches with the natural frequency of L-SPP then resonance occurs and is called localised surface plasmon resonance (LSPR). In LSPR condition, the metal nano-sphere produces a strongly enhanced dipolar field at the immediate vicinity of its surface. This field enhancement is one of the core reasons of many enhanced optical phenomena including SERS.

To understand the SERS enhancement in terms of electromagnetic contribution through L-SPP, we first look into the parameters that determine the signal intensity of normal Raman scattering. Raman scattering being a spontaneous process, the power of the scattered radiation depends linearly on the intensity of the excitation beam. Thus the power of the Stokes Raman scattering can be written as,

$$P_s = N\sigma_{RS} I(\nu_L) \qquad \text{(Eq 1.11)}$$

Where N = number of molecules that undergo Raman scattering, σ_{RS} = Raman scattering cross-section; typical value of σ_{RS} is $\sim 10^{-29}/cm^2$[3]. $I(\nu_L)$=intensity of the incident laser of frequency ν_L.

When a molecule is adsorbed to a nanometallic substrate, it experiences a very high electromagnetic field due to LSPR which is the basis of the electromagnetic enhancement theory of SERS. Furthermore, the close proximity of the molecule to a metal substrate causes an interaction between them leading to chemical enhancement of SERS that we shall discuss later.

Now, in LSPR condition, the electromagnetic field enhancement factor is given by,

$$L(\nu) = \frac{E_{loc}}{E_0} \qquad \text{(Eq 1.12)}$$

where E_{loc} is the amplitude of the local electric field at the nanometallic surface and E_0 is the amplitude of the incident field.

Consequently, the power of the Stokes scattering radiation can be expressed as,

$$P_S(\nu_S) = N\sigma_{SERS}L(\nu_L)^2L(\nu_S)^2I(\nu_L) \quad \text{(Eq 1.13)}$$

where σ_{SERS} is the cross-section for SERS which is necessarily different than that of normal Raman scattering as the environment of the molecule has changed. $L(\nu_L)$ and $L(\nu_S)$ are the field localization enhancement factors for the incident beam (ν_L) and the Stokes scattered beam (ν_S) respectively.

Since the frequency of the incident excitation and the Stokes radiation are quite close, the value of $\Delta\nu$ is much lesser in comparison to the line-width of the SPP mode and thus can be assumed as $L(\nu_L) = L(\nu_S)$. Hence the electromagnetic enhancement factor (R) in SERS scales with the fourth power of field enhancement, i.e.

$$R = \left|\frac{E_{loc}}{E_0}\right|^4 \quad \text{(Eq 1.14)}$$

Here, the overall electromagnetic field enhancement depends on the two factors; (i) the resonant surface plasmon effect and (ii) the lightning rod effect, attributed to the geometry of the metal nanostructures[21–23]. Thus, for SERS enhancement the geometry of the nanometallic structures also plays a significant role.

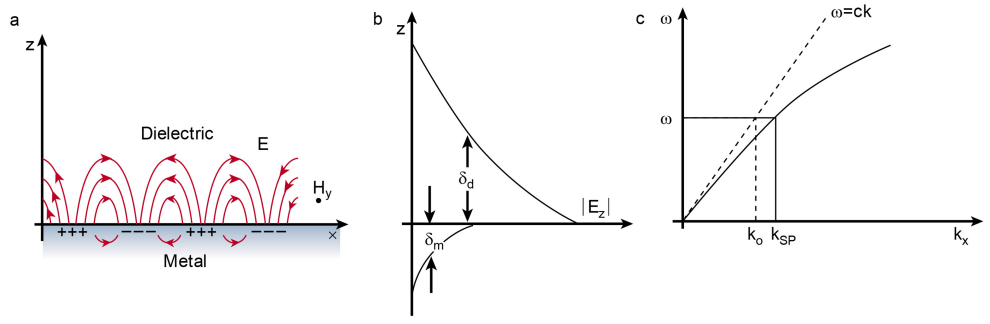

Figure 1.4: (a) Surface plasmon polariton at the flat metallic surface. (b) Evanescent field profile of assosiated with SPP in both the medium. δ_d and δ_m are the decay length in the dielectric and metal respectively. (c) The dispersion curve of the SPP[20].

Propagating surface plasmon polariton (P-SPP):

Another variety of surface plasmon polariton is propagating in nature[17–20]. When SPPs originate at the flat metallic surface, they create a dispersive longitudinal wave

that propagates along the metal-dielectric interface and exponentially decays into both media (figure 1.4a and b). A salient feature of such light-metal interaction is that the momentum of surface plasmon (SP) mode ($\hbar k_{sp}$) is always greater than the momentum of the free photon of same frequency, i.e. $\hbar k_{sp} > \hbar k_0$ (figure 1.4c), (where, $k_0 = \omega/c$ is the free space wavevector) and

$$k_{sp} = k_0 \sqrt{\frac{\epsilon_d \epsilon_m}{\epsilon_d + \epsilon_m}} \qquad \text{(Eq 1.15)}$$

where ϵ_m and ϵ_d are frequency dependent permittivity of the metal and dielectric. Since the momentum of surface plasmon polaritons is higher than that of the free-space photons it is impossible to excite the SPP mode at the flat metal surface by normal incidence of light. To overcome the momentum mismatch there are a few techniques:

- **Prism coupling:** In this case the momentum matching condition is achieved through

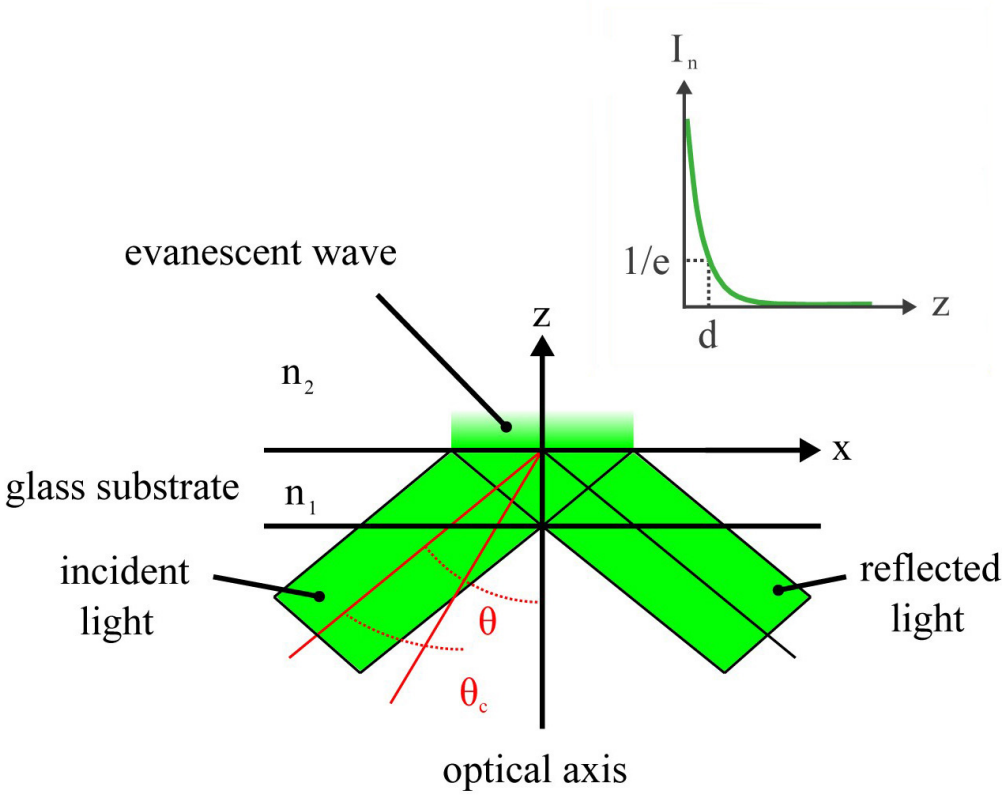

Figure 1.5: Schematic of total internal reflection (TIR) generating evanescent-field. Inset is the decay profile of the evanescent field that follows the condition of $I_z = I_0 e^{-z/d}$ where, penetration depth, $d = \lambda/4\pi(n_1^2 sin^2\theta - n_2^2)^1/2$ [24].

total internal reflection (TIR) at the prism-air interface through evanescent field[24–26]. It is known that when TIR occurs, at the media interface an exponentially decaying electromagnetic field generates which is called evanescent wave (figure 1.5). The evanescent-field can provide the momentum matching condition for the SPP excitation to a metal thin film placed on the prism surface and the resonance condition is given by,

$$k_{sp} = nk_0 sin\theta_0 \qquad \text{(Eq 1.16)}$$

In practice, two types of prism coupling configurations are used for SPP excitation on a metal film.

i. *Kretschmann configuration:*[27] In this case a thin metal film is placed on the prism surface without any gap between the glass and the metal film. Experimentally this is done by placing a metal coated glass slide on the prism using a refractive-index matching oil in between (see figure 1.6a). The evanescent wave by penetrating the metal film, excites the surface plasmons at the metal-air interface. Necessarily, the thickness of the metal film should be less than the skin-depth of the metal at the excitation wavelength. In chapter 4 and chapter 5 we shall discuss a few experiments which utilised the Kretschmann configuration.

ii. *Otto configuration:*[28] Here, the metal film is placed on the prism in such a way that a very small air gap remains and the evanescent field excites the surface plasmons at the same side of the film surface. See figure 1.6b.

Grating coupling: If a metal surface has grating structure on it then incident optical field can be coupled efficiently to excite the SPP of the film (figure 1.6c). In this case the period of the grating, a determines the magnitude of the reciprocal vector of the grating, g as, $g = 2\pi/a$. Therefore, the condition for SPP excitation is

$$K_{SPP} = k_0 sin\theta_0 \pm \nu g \qquad \text{(Eq 1.17)}$$

where ν is an integer number.

Defect on the film: A uniquely easy way to generate SPP on a metal film is through a

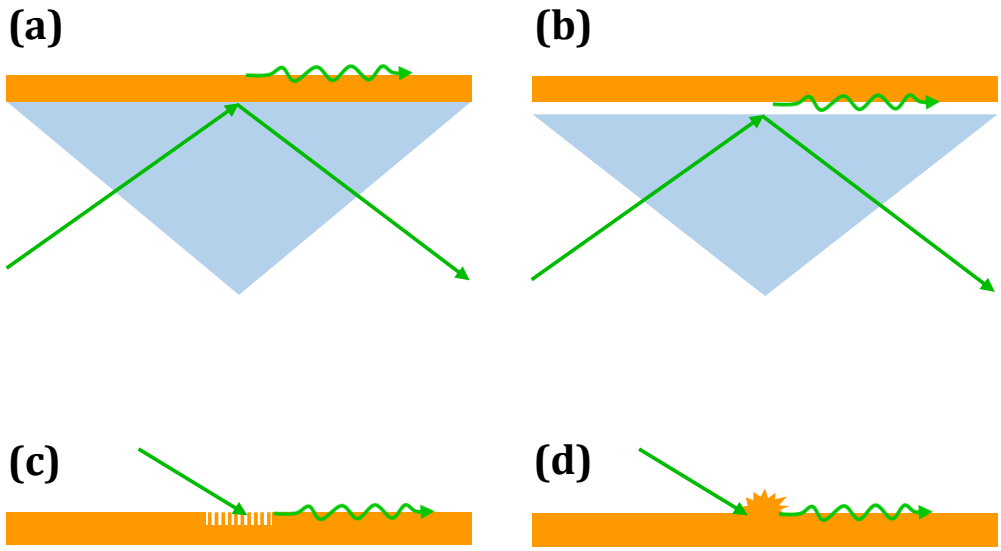

Figure 1.6: Various coupling mechanism for SPP: (a) Kretschmann configuration, (b) Otto configuration, (c) Grating coupling and (d) Coupling through surface defect.

deliberate defect on the film (figure 1.6d). The defect breaks the local symmetry on the film surface and provide SPP excitation requirements.

1.2.2 Chemical enhancement

Though the electromagnetic theory of SERS can explicate the signal enhancement, still a few observations[29–31] cannot be explained satisfactorily. Therefore, a second possible theory was proposed and that is chemical enhancement theory of SERS[12]. Interestingly the overall SERS enhancement is a convoluted effect of both the electromagnetic field enhancement and the interaction between the molecule and the nanometallic substrate. Thus, any of these two mechanisms alone cannot satisfactorily provide a general explanation of SERS enhancement.

However, the chemical enhancement factor is explained through the interaction (adsorption) of molecules to the nanometallic surface. Now, this interaction can happen through either physisorption (non-covalent) or chemisorption (covalent bond formation). In case of physisorption, the energy states of the adsorbate molecules get perturbed thus polarizability of the molecule changes. In such a case, the Raman scattering cross-section changes as well as the frequency of Raman modes. An example of such a phenomenon is factual for pyridine-metal interaction[32–34]. The other kind of

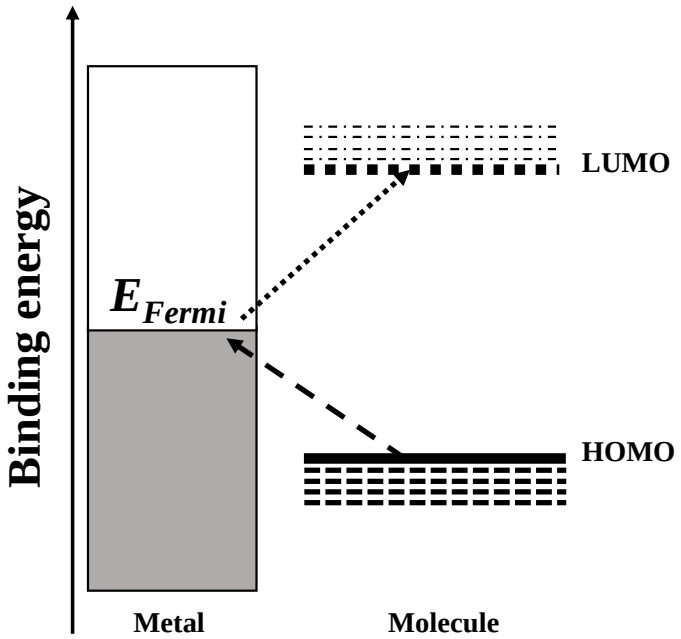

Figure 1.7: Schematic representation of charge-transfer mechanism. Here the metal-molecule complex is formed through the interaction between the metal and the molecular orbitals (either HOMO or LUMO) resulting in an intermediate energy state.

metal-molecule interaction is through charge transfer[35] resulting in an enhancement of SERS. According to this theory, the enhancement can be explained through resonance Raman effect. When a molecule is covalently adsorbed to the metallic surface the electronic interaction between molecule and metal surface results in the formation of a charge-transfer complex. For such interactions the electrons transfer from the metal to an unoccupied molecular orbital (LUMO) or electrons transfer from an occupied molecular orbital (HOMO) to the metal (figure 1.7). Thus an intermediate electronic energy state is formed which can provide a suitable condition for resonance Raman scattering resulting in the Raman signal enhancement by the factor of $\sim$10 to 100[12].

1.3 SERS as a Single-molecule Tool

Since Raman spectroscopy provides the fingerprint of molecular structure, most of the SERS applications utilize it only as an enhanced-spectroscopy technique. Although looking into the origin of SERS it is obvious that through SERS many fundamental aspects of molecular plasmonics can be addressed. Single-molecule SERS is one of the

very important areas of research in fundamental as well as analytical aspects. In general, single-molecule spectroscopy is a desired subject of research to understand various physical and chemical properties of an isolated molecule, while single-molecule SERS is more than that. A profound knowledge and a tight grip in SMSERS can be helpful to understand many other fundamental problems like, understanding the origin of SERS enhancement[36, 37], field distribution around a nanometallic object [38], SERS vibrational pumping[39–42], single-molecule electrochemistry[43] etc. Another facet of the SMSERS application could be to address biological problems. The contemporary single-molecule tool widely used in biology is based on fluorescence[44]. Though, SERS has many advantages over fluorescence technique[4], still as a single-molecule tool SERS has not been very popular. As SERS is a conjugated process depending on both the molecule and the nanometallic substrate, it is not always a straightforward method to be used as a single-molecule tool. Therefore, to make SERS a widely applicable single-molecule tool, two basic criteria should be achieved, (i) a reliable methodology to accomplish SMSERS and (ii) an efficient detection platform for SMSERS. In 1997, Nie and Emory first showed that SERS can be utilized as a single-molecule detection tool[46]. In the same year, Kneipp et al. independently provided the SMSERS proof with statistical evidence[47]. It was also realized that the SERS cross-section can be larger than that of fluorescence and can be a superior technique to address the single-molecule problems. However, to make SERS a viable single-molecule tool, in last two decades a lot of work has been done mainly on the two aspects that we mentioned above. About the methodology of SMSERS we shall discuss in a separate chapter (chapter 2) elaborately. Another important prerequisite for SMSERS is an efficient detection platform which mostly involves proficient SERS substrates along with appropriate microscopy techniques. Since the major contribution of the SERS enhancement comes from the electromagnetic field localization, silver and gold nanostructures have been known to be the best SERS substrates with optical wavelengths[4]. Although for the unique plasmonic property silver substrates produce very high electromagnetic enhancement[48] compared to gold and thus have been extensively used for SMSERS.

There are plenty of SERS substrates available in the literature but only very few of them can show single molecule sensitivity. Here we shall mainly discuss about the

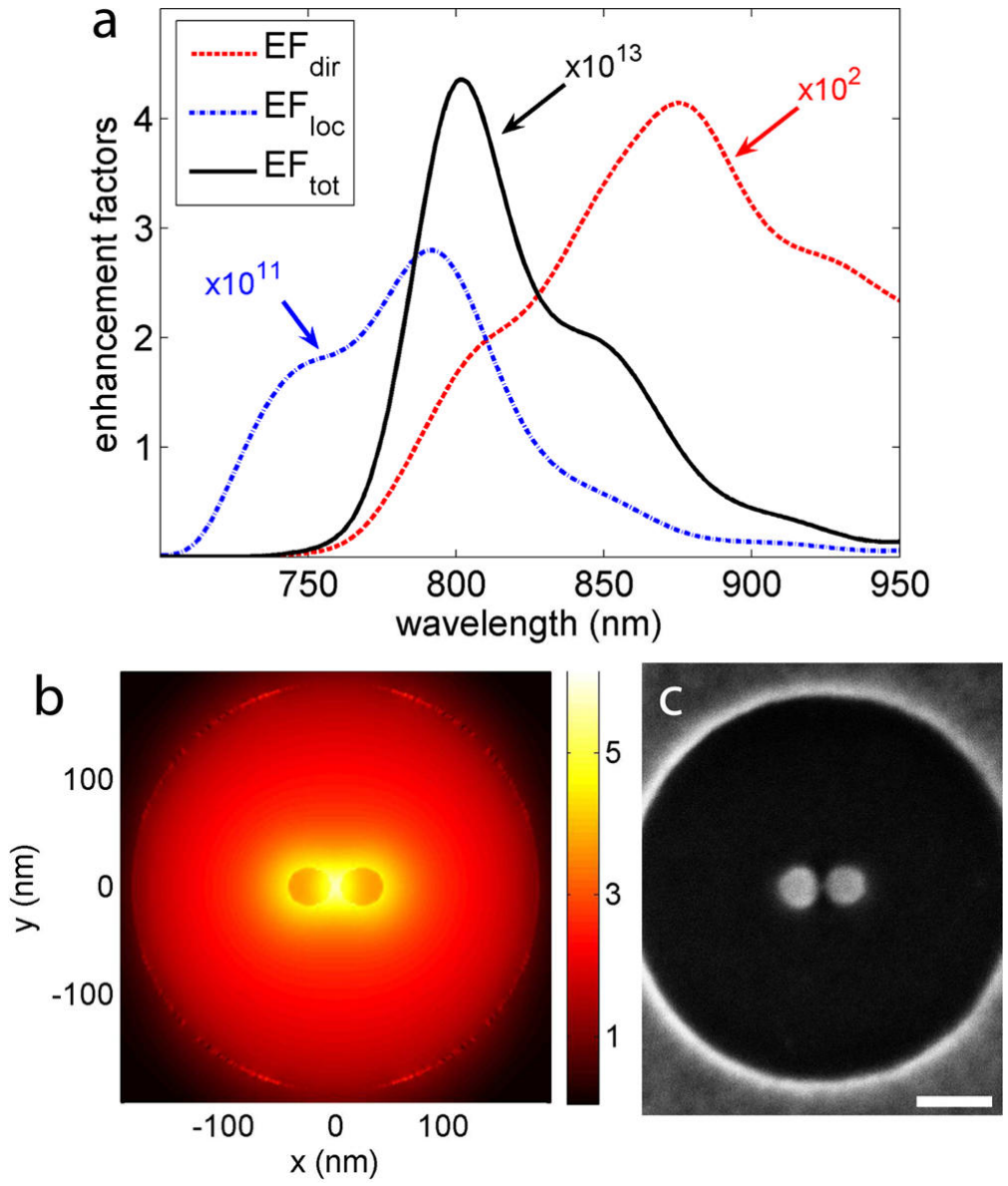

Figure 1.8: (a) Calculated enhancement factor from the electromagnetic field and directionality contribution for a gold nanoantenna. (b) Normalized electric field intensity for 785nm excitation (plotted in log scale). (c) Scanning electron microscopy image of the nanoantenna. Scale bar is 90nm[45].

single-molecule SERS substrates. The very first two individual SMSERS experiments were done by using silver colloidal nanoparticles[46, 47]. Later many other groups utilized the Ag nanoparticles for SMSERS study[50–54]. In all the cases, the colloidal nanoparticles were aggregated deliberately to attain optimum SERS enhancement. A very unique strategy to improve the field localization is by placing two nanoparticles

close to each other. The coupling between the L-SPPs of two nanoparticles facilitates a highly localized field at the inter-particle junction[12, 55]. Such junctions are termed as electromagnetic hot-spots. These hot-spots not only play a crucial role for single-molecule SERS but also utilizing them in a controlled geometry can lead to many interesting phenomena such as optical antenna effect[56–58], Fano resonance[59–64], chiral plasmons[65], nonlinear optical processes[66–69], plasmonic nanofocussing[70–72], transportation of light[73, 74], sensing[75, 76] and so on[77]. However, the formation of hot-spots in colloidal particles is mainly based on chemical means; thus, it is not much controllable. A precise way of creating plasmonic hot-spots is through nanofabrication with top-down approach. The advantage of such approach is that the hot-spot can be designed to act as an optical antenna as well as can increase the SERS enhancement by modifying the far-field emission pattern[45, 78–80]. Ahmed et al. showed that directionality of the hot-spots can improve SERS enhancement additionally by a factor of 100[45], shown in figure 1.8. Interestingly, they could harness gold based

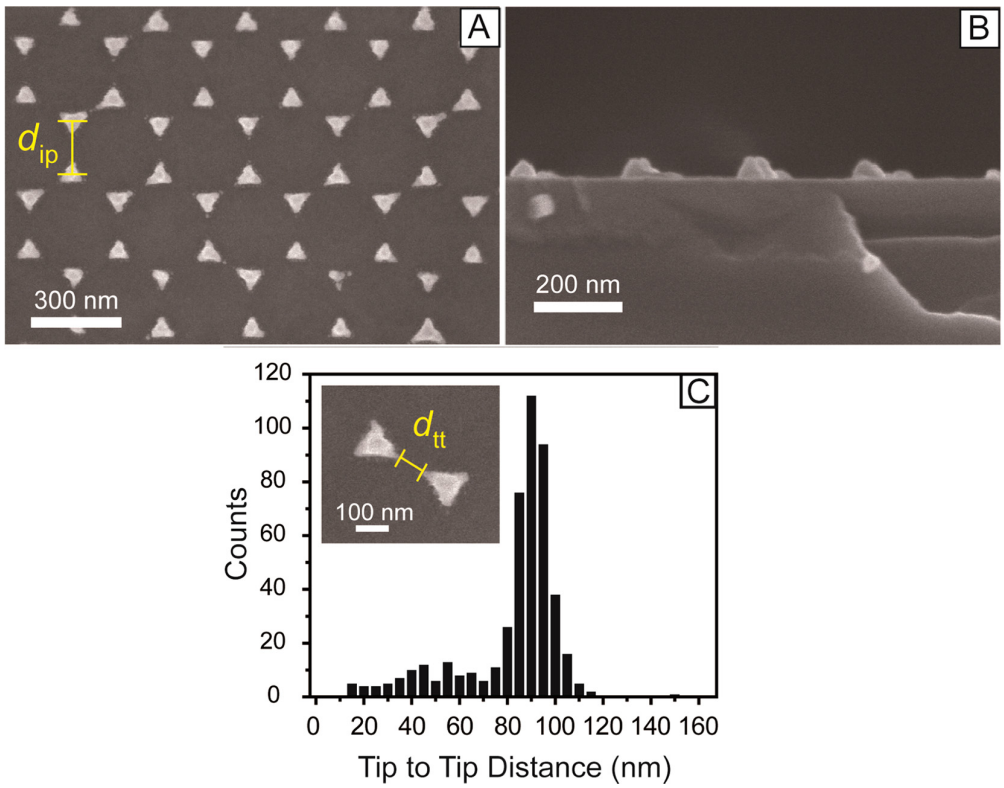

Figure 1.9: Scanning electron microscopy images of silver triangular nanopyramids prepared by nanosphere lithography[49].

nanoantenna for SMSERS study despite the fact that gold based structures do not produce high SERS enhancement. Another such directional SMSERS measurement was done by Crozier's group using silver based optical antenna[79]. The above examples of SMSERS we discussed, have utilized nano-gap based hot-spots for SERS enhancement, while Zrimsek et al. have shown that SMSERS hot-spots can be achieved even without a nano-gap by using precisely fabricated triangular nanopyramids (see figure 1.9)[49]. Thereby, we see that the efficient substrate development (with suitable methodology) made SMSERS a reliable 'fact than fiction'[81].

So far we have discussed the SMSERS evidences where dye molecules (resonant or pre-resonant) were used as probe. For such molecules, the SERS cross-section was large due to the resonance effect resulting in high enhancement factor. However, Blackie et al. showed that SMSERS can be achieved even with the non-resonant molecules which have relatively smaller SERS cross-section than that of the dye molecules[82]. This experiment is an important milestone in the path of SMSERS leading to be a widely applicable single-molecule tool irrespective of the probe molecule. Nevertheless, many more SMSERS evidences can be found in the literature, which also to some extent contributed to the progress in this field.

1.4 Scope and Outline of the Thesis

In the context of the earlier discussion, the development of the SMSERS field can be classified into two aspects, methodology and detection efficiency. In this thesis, first we shall discuss about the methodological development of SMSERS as this will help to understand the latter part of the thesis. Subsequently, we shall discuss our own work which is mainly a contribution to the development of SMSERS detection platform. Also our work can provide a nice platform to couple molecular plasmonics to various other fields like microfluidic-SERS, plasmofluidic metamaterial, catalysis, soft-matter physics etc. There are three facets of my thesis work (schematically shown in figure 1.10) - SMSERS with a new type of nanostructure, SMSERS with evanescent-field microscopy and a unique strategy for plasmofluidic assembly of nanostructures.

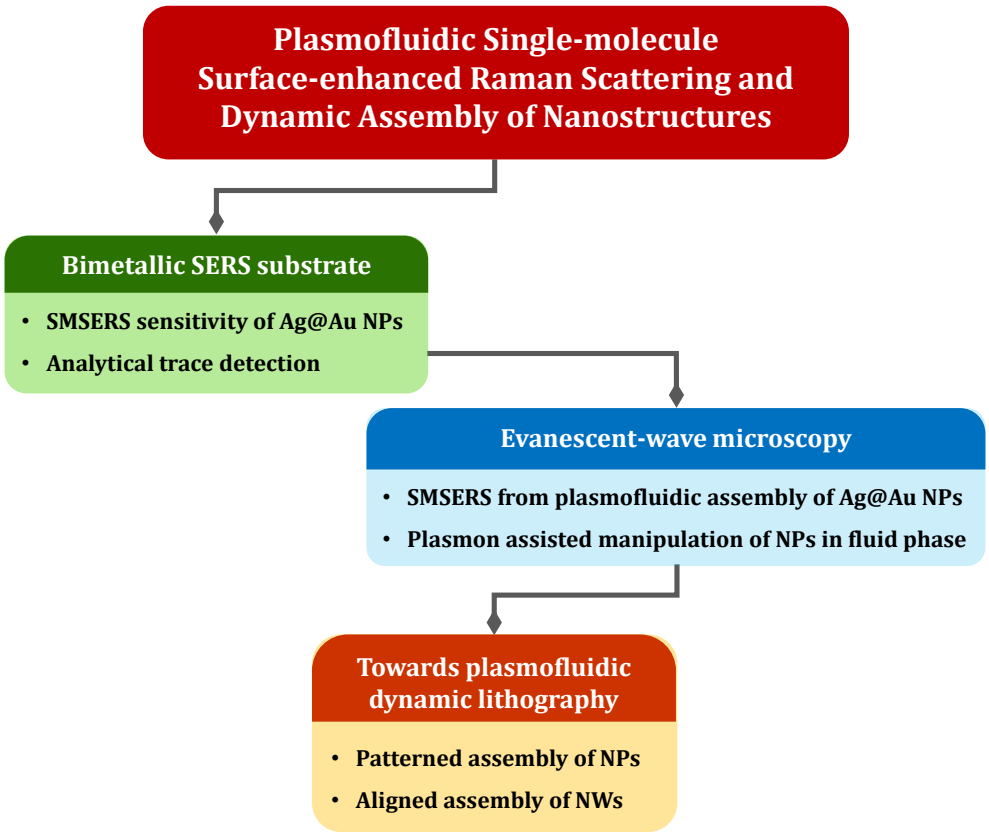

Figure 1.10: Outline of the thesis work.

Chapter 2: In this chapter the gradual evolution of the methodology of single-molecule surface-enhancement Raman scattering is described. To establish the SMSERS technique as a viable spectroscopic single-molecule tool, a consistent experimental approach is essential and fortunately SMSERS has already reached that 'matured stage'[83]. Here we shall first talk over the experimental strategies of SMSERS, specifically on the bi-analyte approach. Also statistical analysis methods viz. the Poisson statistics and modified principal component analysis (MPCA) associated with the SMSERS strategies will be discussed. This discussion will sufficiently help to understand the SMSERS results in the next two chapters.

Chapter 3: From this chapter onwards we shall discuss our own work. This part depicts mainly the single-molecule SERS sensitivity of a unique plasmonic nanostructure that is silver-core-gold-shell (Ag@Au) bimetallic nanoparticles. These nanoparticles can be an excellent alternative to the conventional silver colloidal nanoparticles for SMSERS with tunability of LSPR over visible to near infra-red regime. Furthermore,

these nanoparticles can be harnessed for analytical trace-detection at ultra-low concentrations.

Chapter 4: In this chapter a new microscopic platform is introduced for SMSERS. The microscopy is based on an evanescent-wave excitation through attenuated total internal reflection (ATIR). In such an excitation geometry, the SPP on a metallic thin-film can be produced very effectively and that can lead to many interesting phenomena such as reversible assembly of plasmonic nanoparticles, spatial manipulation of them in plasmofluidic (plasmonic field in fluidic medium) environment etc. Nonetheless, this plasmofluidic microscopy system can be an excellent platform for SMSERS detection.

Chapter 5: This chapter is mostly based on the extended work of the previous project. Here, to comprehend the mechanism of the plasmofluidic assembly process, few more experiments are shown. Interestingly, the assembly of the nanoparticles can be patterned to a certain extent by structuring the excitation. Also by using a stripped metallic thin-film, one-dimensional nanostructures can be assembled with a specific alignment.

Thereby, in this thesis we shall discuss about the brief methodology, unique plasmonic substrate and a new microscopic technique for single-molecule SERS and moreover a prospect of plasmofluidic dynamic lithography of nanostructures.

Chapter 2

Strategy and Statistics of Single-molecule SERS

Since surface-enhanced Raman scattering (SERS) is a process not dependent solely on molecular properties, (also on the plasmonic substrates) the single-molecule SERS spectroscopy appears with a unique challenge regarding experiment and analysis. To systematically argue the single-molecule detection evidence, a defined strategy is necessary. Historically, different approaches have been pursued to ascertain single-molecule SERS (SMSERS), and after years of debate on methodology, a general consensus has emerged in recent times. In this chapter we shall discuss briefly on SMSERS arguments in terms of the experimental approach and the statistics used for data analysis.

2.1 Strategy

Like every field of research, the road to single-molecule SERS detection has its own map in the history; as not being very old it is still developing and thus an active area of research. In the road map of the methodology, two consecutive phases of SMSERS are prominent; first phase came up with 'single-analyte' approach and the next with 'bi-analyte' approach. Here we shall briefly describe both the strategies to help in believing and understanding the SMSERS results in the next chapters.

2.1.1 Single-analyte approach

We shall start with few initial evidences of SMSERS which were mainly based on single analyte approach. The main strategy of this technique is to probe the analyte molecules in ultralow (pico/femto-molar) concentration. The basic assumption of this approach is that in such a low analyte-concentration there cannot be much more than one molecule per one nanoparticle or a cluster of nanoparticles. Here, the argument of SMSERS strictly depends on how the analyte-adsorbed nanoparticles are distributed in the probe volume. Thus sample preparation and signal collection technique play a critical role to reason the single-molecule SERS. Based on this, three different types single-molecule studies are found in the literature. (i) Amongst them large number of works were done with dried colloidal silver nanoparticles mixed with a resonant or pre-resonant dye[46, 50, 52, 84]. In this method the dye-adsorbed nanoparticles are sparsely immobilized on suitable substrates by different means and SERS signals from individual nanoparticles or clusters are collected and analysed. (ii) Another approach was to carry out the experiment in solution phase[47, 85, 86]. Here, SERS intensity fluctuations with time are studied and statistically analysed. In the single-analyte strategy the molecular concentration is chosen so low that the nanoparticle to molecule ratio comes as approximately 10:1, but such calculations are mostly done in the basis of assumption, hence it is difficult to quantify the dye adsorption very precisely at that concentration. (iii) The third approach solved the problem of unquantified adsorption with an alternative sample preparation method i.e. Langmuir-Blodgett monolayer technique[51, 87], where one can manipulate the spatial concentration of the analyte molecule.

However, the claim of single-molecule SERS evidences with this approach is not very satisfactory as this approach is prone to large errors due to many experimental reasons[81]. Also, using ultralow concentration of the analyte leads to very less probability of the SERS signals which is statistically unreliable due to insufficient sampling. Therefore, an alternative strategy is required for SMSERS to overcome the limitations of this method and bi-analyte approach of SMSERS suffices that.

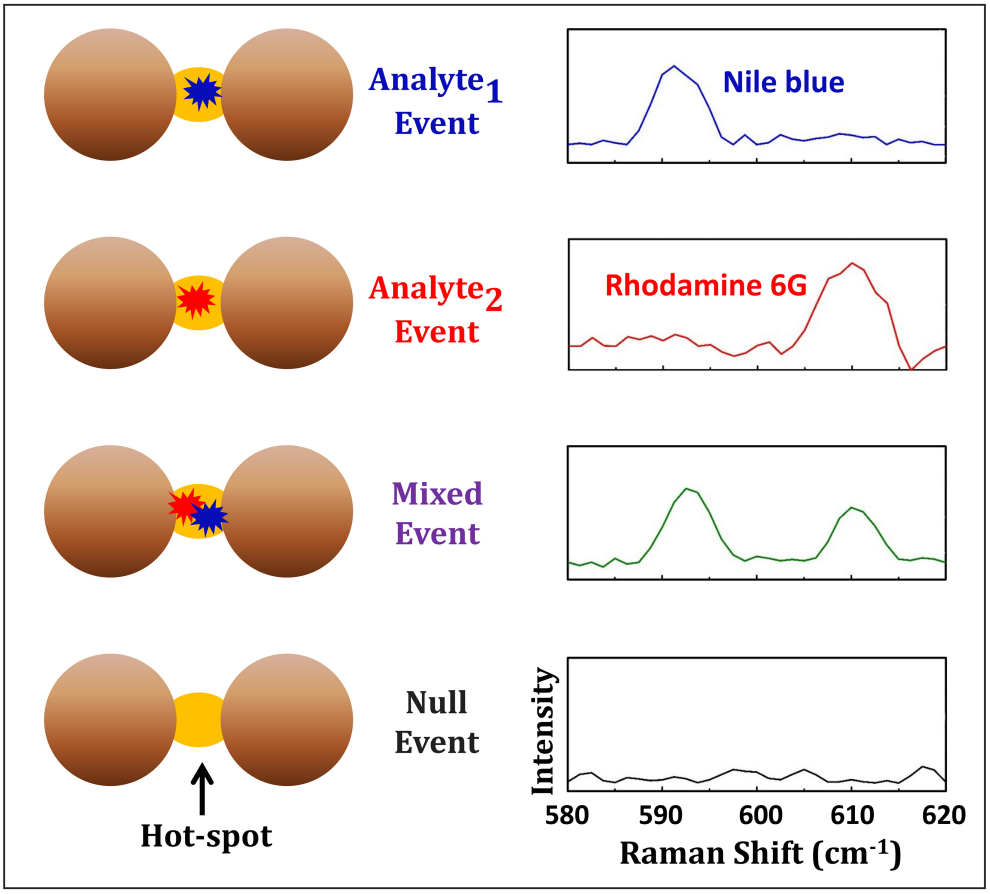

Figure 2.1: Schematic showing four possible events in bi-analyte single-molecule SERS experiment due to the molecular distribution of the two analytes in the electromagnetic hot-spots.

2.1.2 Bi-analyte approach

The bi-analyte approach to address SMSERS was first proposed by Eric Ru et al.[53] and till date this is the most reliable strategy of single-molecule SERS[45, 49, 54, 82, 88, 89]. In this approach the analyte concentration used is adequately high to serve enough sampling of SERS signals to argue single-molecule statistics. Also this technique relies on the molecule to hot-spot ratio, thus increases the signal probability. The electromagnetic hot-spots take an important part in this approach rather than the dispersed single nanoparticles, as only those hot-spots (created by aggregations of individual nanoparticles or any other means) can provide enough SERS enhancement[90, 91] to probe single molecules.

The basic principle of this method consists in measuring SERS signals from the

equimolar mixture of the two types of analyte molecules having distinct spectral signatures. The analytes are chosen by keeping the fact in consideration that both the molecular species have comparable SERS cross-sections for the excitation wavelength. In this experiment, a number of SERS signals are collected from the hot-spots distinguished either spatially or temporally and analysed statistically. The crux of the bi-analyte approach is that throughout the whole experimental scenario only four events arise (schematically shown in figure 2.1); viz. (i) the hotspot can contain either purely one type of analyte molecule (molecules) hence pure analyte$_1$ signal occurs, (ii) or purely another analyte molecule (molecules), resulting pure analye$_2$ signal, (iii) hot-spot containing mixture of both the analyte molecules, producing mixed signal (iv) and lastly, for a certain state there may not be any molecule in the hot-spot in the probe volume and no signal conceives.

The argument of single-molecule SERS comes from the probability distribution of purely one analyte SERS signals (i.e. either of the first two events shown in figure 2.1) measured experimentally. The logic is as follows. If only two molecules from each of the two types of analytes compete for a particular hot-spot then the probability of the pure signal event will be $1/2$. Now, if the signal originates from 2, 3 or N number of random molecules then the probability of pure signal will decrease down to $1/4$, $1/8$ or $1/2^N$ respectively. Hence it is clearly evident that getting purely one type SERS signals with a large probability indicates the single-molecule (or very few molecules) SERS signatures. Then, a concentration dependent bi-analyte SERS experiment (from higher to lower analyte concentration) should in principle reveal the crossover of the regime of many molecule to single-molecule SERS. At higher analyte concentration the probability of mixed signals are very high. By decreasing the concentration one can achieve the desired single-molecule detection regime where only pure signals of any of the two analytes are probable.

It is also factual that the analyte concentration used in this approach is much greater (in an order or two) than that used in ultralow concentration SMSERS approach. Thus, this approach can provide an alternative but direct proof of single-molecule evidence showing a path to better sampling of SMSERS statistics.

2.2 Statistics

We have discussed above the experimental strategies of single-molecule SERS. But this is actually the partial segment of the whole story. The other part of SMSERS is the analysis of the sampled SERS signals. In SMSERS, single-molecule character is not concluded from individual spectrum in isolation, rather, a detailed statistical analysis in involved in this journey. Hence a precise statistical approach is necessary. A very archetypal statistics used for single-molecule spectroscopy is Poisson distribution. Herein we shall briefly revisit the discussion reported by Eric Ru, et al. on whether the Poisson distribution is appropriate for SMSERS and any alternative statistics for SMERS[92]. This particular discussion is necessary in this moment as we shall be showing a detailed statistical analysis in the next chapter to conclude SMSERS results.

2.2.1 Poisson distribution for SMSERS

The Poisson distribution defines as a discrete probability distribution for the counts of events that occur randomly in a given interval of time (or space). If we let X equals to the number of events in a given interval and the mean number of events per interval is λ, then the probability of observing n events in a given interval is given by

$$P(X = n) = e^{-\lambda}\left(\frac{\lambda^n}{n!}\right) \qquad n = 0, 1, 2, 3... \qquad \text{(Eq 2.1)}$$

Where λ is the mean value of X.

Generally Poisson statistics is applicable for such situations where the events can be counted in whole numbers. In SMSERS the events are counted in terms of SERS intensity and there arises the ambiguity. While interpreting SMSERS through Poisson statistics, the obvious assumption is that every single molecule produces exactly same intensity. But in SMSERS the signal-intensity does not depend on the molecule solely rather on the electromagnetic hot-spots of the SERS substrate. The variation in SMSERS signal intensity for different events is attributed to many factors such as inhomogeneity of SERS substrate, non-uniform adsorption of the molecules to the substrate,

the spatial orientation and position of the molecules in hot-spot, the position of the hot-spot in the probe volume, radiation pressure or optical forces etc. and this results in a greater than 10-fold variability of signal intensity. Hence the authenticity of normal Poisson statistics is unconvincing for SMSERS.

To overcome this ambiguity a modified Poisson statistics i.e. 'Poisson Binomial Distribution' (for mainly bi-analyte SERS) was introduced by Van Duyne's group[93]. This is based on the rationale that at single-molecule regime (i.e. at a certain low concentration) the number of molecules adsorbed to the substrates follows the Poisson distribution and the probability of occurring either analyte's SMSERS signature is governed by binomial distribution; thus the overall probability goes as the product of both the distributions,

$$P(n_1, n_2, \lambda) = \frac{e^{-\lambda}\lambda^{n_1+n_2}}{(n_1+n_2)!} \times \frac{(n_1+n_2)!}{n_1!n_2!}\left(\frac{1}{2}\right)^{(n_1+n_2)} = \frac{e^{-\lambda}}{n_1!n_2!}\left(\frac{\lambda}{2}\right)^{(n_1+n_2)} \quad \text{(Eq 2.2)}$$

where, n_1 and n_2 are the number of the molecules of analyte$_1$ and analyte$_2$ respectively and λ is the estimated number of molecules adsorbed per substrate.

Another alternative and unambiguous statistical analysis of SMSERS is modified principal component analysis (MPCA), first proposed by Etchegoin et al.[94]. In our single-molecule SERS experiments we have used MPCA and hence we shall discuss only about modified principal component analysis.

2.2.2 Modified principal component analysis (MPCA)

This method is a revised extension of principal component analysis (PCA) method used for many analytical and spectroscopic applications[95]. In this section we dwell on the basic theory and algorithm of PCA and how the modified version (MPCA) connects to the bi-analyte SMSERS data analysis, based on a previous work by Etchegoin et al.[94]. This will help us to discuss our experimental SMSERS work in the next chapter. First we discuss the relevance of MPCA to the bi-analyte SMSERS problem. Like the Poison statistical approach, this method does not completely rely on the signal intensity, rather, it deals with the occurrence of the SERS signals. For two-analyte approach, PCA finds the two pure (one analyte) SERS signals distinctly and tells their statistical distribution.

In other words, it reveals the relative contribution of the analytes to the total signal in the form of probability histogram. It is true that in all concentrations, the single-molecule inference cannot be drawn by recognizing purely one analyte signal, but for a certain low concentration of analytes for a particular experimental system, the single-molecule signatures can be ensured. Next, we discuss about PCA, which is a very powerful statistical technique generally used for a large data set to reduce its dimension, without losing much information. It is a linear transformation that transforms the data to a new co-ordinate system in such a way that the new set of variables are linear functions of the original variables. It is done by simply finding the principal components of the whole data and for bi-analyte SERS data set, the two principal components are the two SERS signatures from the analyte molecules. PCA normally fits well for the data which are linear combination (additive) of relatively independent variables. And in bi-analyte SERS method, the analytes are chosen such that they compete for a particular hot-spot independently with equal probability. Also a crucial point is that the signature signals from each analyte specified for PCA analysis should not have any spectral overlap.

The first step of PCA starts with the spectral data set written in the form of a rectangular matrix. For that a specific spectral region is taken where both the analyte signatures are present. For simplicity of the calculation and presentation of the result, only two (one of each analyte) Raman bands are considered for a single data set. Let us denote the rectangular matrix as M, where

$$M = T(spectrum\ number) \times N(wavenumber) \qquad \text{(Eq 2.3)}$$

We assign each element of the matrix as the intensity at that particular wavenumber; thus we write M, elaborately as,

$$M = \begin{pmatrix} I_{t_1}^{\upsilon_1} & I_{t_1}^{\upsilon_2} & \dots & \dots & I_{t_1}^{\upsilon_N} \\ I_{t_2}^{\upsilon_1} & I_{t_2}^{\upsilon_2} & \dots & \dots & I_{t_2}^{\upsilon_N} \\ \dots & \dots & \dots & \dots & \dots \\ I_{t_T}^{\upsilon_1} & I_{t_T}^{\upsilon_2} & \dots & \dots & I_{t_T}^{\upsilon_N} \end{pmatrix} \qquad \text{(Eq 2.4)}$$

The second step is centering the matrix through mean subtraction. Mean subtraction

is crucial to find the principal components correctly; if centering is not done then mostly the first principal component may look like very similar to the mean of the data instead of describing the direction of maximum variance. Thus a mean of zero is required to find the basis which minimizes the mean square error of the approximation of the data. For this data, the mean of the row is calculated and subtracted from each row element. The new centered matrix now looks like,

$$\hat{M} = \left(\hat{I}_{t_i}^{v_j}\right) \tag{Eq 2.5}$$

where,

$$\hat{I}_{t_i}^{v_j} = I_{t_i}^{v_j} - \overline{I_{t_i}} \quad and \quad \overline{I_{t_i}} = \frac{1}{N}\sum_{j=1}^{N} I_{t_i}^{v_j} \tag{Eq 2.6}$$

Third step is the calculation of covariance matrix (V) for the N number of column vectors for the matrix $\hat{M}(T \times N)$. The covariance matrix, V is calculated as,

$$V = \left(cov(\hat{I}_t^{v_j}, \hat{I}_t^{v_k})\right) \tag{Eq 2.7}$$

where $cov(\hat{I}_t^{v_j}, \hat{I}_t^{v_k}) = cov(\hat{I}_t^{v_k}, \hat{I}_t^{v_j})$ is the covariance of the intensity columns at v_j and v_k, calculated using the unbiased estimator for the covariance given as,

$$cov(\hat{I}_t^{v_j}, \hat{I}_t^{v_k}) = \sum_{i=1}^{T} \frac{\left(\hat{I}_{t_i}^{v_j} - \langle \hat{I}^{v_j} \rangle\right)\left(\hat{I}_{t_i}^{v_k} - \langle \hat{I}^{v_k} \rangle\right)}{(T-1)} \tag{Eq 2.8}$$

the symbol $\langle ... \rangle$ denotes the time-average;

$$\langle \hat{I}^{v_j} \rangle = \frac{1}{T}\sum_{i=1}^{T} \hat{I}_{t_i}^{v_j} \tag{Eq 2.9}$$

We see that the covariance matrix comes out as a square matrix of size $(N \times N)$ i.e. in the dimension of the spectral data points (wavenumbers). The statistical accuracy relies on the large number of the spectra i.e. T.

Fourth step is to get the principal components of the data. In this step N numbers of eigenvalues and corresponding N number of eigenvectors are obtained from the covariance matrix. Since the covariance matrix is real and symmetric, all the eigenvalues

are positive real numbers. The eigenvectors corresponding to the greatest variances i.e. with largest eigenvalues are the most significant components and these are the principal components of the entire data matrix. For problems like bi-analyte SERS where only two distinct Raman band peaks are monitored for two analytes with a certain wavelength range of the spectrum, PCA finds mostly two principal components corresponding to the two peaks.We denote those two principal components as $f_1^{v_j}, f_2^{v_j}$ $(j = 1..N)$. For PCA method, it is advantageous to work with minimum numbers of eigenvectors to avoid complications in calculation. In bi-analyte SERS each individual spectrum (collected in time series) can be expressed as a linear combination of the two principal components i.e. $f_1^{v_j}$ and $f_2^{v_j}$.

Fifth step is to obtain a table of coefficients. To represent a particular spectrum two coefficients are needed which actually depict the linear combination of the principal eigenvectors for that very spectrum. The table of coefficients C can be acquired by following calculation,

$$C = \begin{pmatrix} \alpha_1 & \beta_1 \\ \alpha_2 & \beta_2 \\ \cdots & \cdots \\ \alpha_T & \beta_T \end{pmatrix} = \hat{M} \begin{pmatrix} f_1^{v_1} & f_2^{v_1} \\ f_1^{v_2} & f_2^{v_2} \\ \cdots & \cdots \\ f_1^{v_N} & f_2^{v_N} \end{pmatrix} \qquad \text{(Eq 2.10)}$$

In this step the conventional PCA ends, yielding all the sufficient parameters to reconstruct the data, viz. (i) the mean of each spectrum, $\overline{I_{t_i}}(T \times 1)$, (ii) two principal components,$f_1^{v_j}, f_2^{v_j}$ (each $1 \times N$) and (iii) the coefficients matrix C ($T \times 2$). Hence the reconstructed spectral data can be written as,

$$I_{t_i}^{v_j} = \alpha_i f_1^{v_j} + \beta_i f_2^{v_j} + \overline{I_{t_i}} \qquad \text{(Eq 2.11)}$$

Up to this we have applied the conventional PCA technique to the spectral data set. The main task is now to relate the PCA analysis to the real bi-analyte SMSERS problem.

The subsequent step is to first plot the C matrix in coefficient space which actually gives the distribution of the two analytes' SERS signals. For a typical bi-analyte SMSERS data (we shall see in the next chapter), two distinct SERS events spread with

a clear pattern of two main axes, where events along the axes in coefficient space are necessarily the pure analyte signatures differing by their total intensity and the events between the two axes are nothing but the mixed signals. Now to extract the spectroscopic significance of the analysed data we need, (i) the two eigenvectors to represent the actual SERS spectra i.e. with positive peak for each analyte, (ii) the coefficients matrix C to be composed of only positive coefficients and (iii) the relative intensities of the two eigenvectors to exactly denote the analyte concentrations. To achieve these three conditions the following transformation steps are done.

Step 1: To define two vectors, $\vec{e}_1 = n_1^x\vec{e}_x + n_1^y\vec{e}_y$ and $\vec{e}_2 = n_2^x\vec{e}_x + n_2^y\vec{e}_y$ as the unit vectors ($\vec{e}_1 \cdot \vec{e}_1 = 1$ and $\vec{e}_2 \cdot \vec{e}_2 = 1$) along the two principal direction signifying the two distinct analyte events in the coefficient space. Thus this step is not purely algorithmic, but is based on observations.

Step 2: To obtain two coefficients (α and β) by following the action,

$$(\alpha \quad \beta) = \left(\langle\hat{I}^{v_1}\rangle\ \langle\hat{I}^{v_2}\rangle\ ...\ \langle\hat{I}^{v_N}\rangle\right)\begin{pmatrix} f_1^{v_1} & f_2^{v_1} \\ f_1^{v_2} & f_2^{v_2} \\ \cdots & \cdots \\ f_1^{v_N} & f_2^{v_N} \end{pmatrix} \tag{Eq 2.12}$$

The α and β in fact tell that how much of the two eigenvectors ($f_1^{v_j}, f_2^{v_j}$) are needed to represented the average spectrum with zero mean intensity.

Step 3: To find linear transformation factor, R which rotates $\vec{e_1}$ into $\vec{e_x}$ and $\vec{e_2}$ into $\vec{e_y}$ with possible scaling factors. These scaling factors should include the analyte concentration factor if the concentrations are different in the real experimental condition. Then R can be written as,

$$R = \begin{pmatrix} k_1\, n_1^x & k_2\, n_2^x \\ k_1\, n_1^y & k_2\, n_2^y \end{pmatrix}^{-1} \tag{Eq 2.13}$$

where,

$$\begin{pmatrix} k_1 \\ k_2 \end{pmatrix} = \begin{pmatrix} c_1\, n_1^x & c_2\, n_2^x \\ c_1\, n_1^y & c_2\, n_2^y \end{pmatrix}^{-1} \begin{pmatrix} \alpha \\ \beta \end{pmatrix} \tag{Eq 2.14}$$

Step 4: To get the new rescaled and reoriented table of coefficients. The new set of

coefficients is now written as, $C = C\,({}^{t}R)$.

Step 5: To get transformed eigenvectors, $g_1^{v_j}$ and $g_2^{v_j}$ as;

$$\begin{pmatrix} g_1^{v_j} \\ g_2^{v_j} \end{pmatrix} = \left({}^{t}R\right)^{-1} \begin{pmatrix} f_1^{v_j} \\ f_2^{v_j} \end{pmatrix} \qquad \text{(Eq 2.15)}$$

The benefits of the above modification steps to PCA are twofold. Firstly, the two principal components i.e. the two eigenvectors ($f_1^{v_j}, f_2^{v_j}$) are now directly linked to the two analytes' Raman signatures. Secondly, the transformed coefficients directly provide the average number of each analyte producing the SERS signal.

The last step of the entire bi-analyte SERS data analysis is to get the probability distribution of the SERS events from the two analytes in the form of a histogram by discarding the noisy events. In this step a threshold intensity value is set to distinguish the signals from the noise. The threshold value can be decided with a variety of schemes but for our experimental results we utilised standard deviation calculation. We took only those events which had peak intensity twice above the standard deviation. Next, to get the probability histogram the logic is very simple. If I_1 and I_2 are denoted as SERS intensity of the two pure signal then, for a point in coefficient space with coordinates x and y has a total intensity, $I_{tot} = (xI_1 + yI_2)$. Now the fraction of analyte$_1$ in terms of signal intensity for a certain event is $xI_1/(I_{tot})$. However, the main aim of this calculation is to get the fraction in terms of the average number of the molecules contributing to a certain signal. Within the experimental framework where the cross-section and the concentration factors have been already taken care for, the probability of one analyte is,

$$p_1 = x/(x+y) = 1/(1 + abs(y/x)) \qquad \text{(Eq 2.16)}$$

The abs(y/x) is taken to avoid the negative values in practical situations. The data analysis of the bi-analyte SMSERS using modified principal component analysis technique completes here and the inference of the single-molecule evidence comes through combined experimental and statistical reasoning.

2.3 Summary

To summarize this chapter, we have briefly discussed on the development of the methodology of SMSERS experiments. We see that bi-analyte approach has evolved as the most adopted strategy for single-molecule SERS studies as it utilizes sufficiently high analyte concentration and thus can provide large sampling to build up a sound statistics to argue single-molecule SERS signature with high precision. Also we have discussed about modified principal component analysis, a 'reliable' statistical approach for SMSERS data analysis. Overall, in this chapter we have tried to give a brief overview of the strategy and statistics of SMSERS based on the literature over last 20 years.

Chapter 3

Single-molecule SERS using Ag@Au Bimetallic Nanoparticles

Chapter 3 is an adaptation of the research article, '*The journal of physical chemistry letters 4 (7), 1167-1171*'. The article describes the single-molecule SERS sensitivity of Ag-core Au-shell (Ag@Au) colloidal nanoparticles using bi-analyte methodology.

3.1 Introduction

In recent years, surface enhanced Raman scattering (SERS) has emerged as a plasmon-based spectroscopic tool with single-molecule sensitivity and excellent chemical specificity[4, 16, 83, 96]. Since the crux of this technique relies on the enhanced electromagnetic (EM) field from localized surface plasmon polariton (L-SPP), free electron oscillation on the surface of a metal nanostructure, plasmonic nanostructures play an important role to harness single-molecule surface-enhanced Raman scattering (SMSERS).

Conventionally, Ag nanoparticles are most commonly used in the solution-based SMSERS experiments[46, 50, 52, 84], but their usage is limited due to toxicity[97, 98] and oxidation issues. On the other hand, Au nanoparticles are relatively biocompatible[99–101] and stable SERS active substrates, but they do not facilitate large scale SERS enhancement factors, which is an important prerequisite for SMSERS. Under such constraints, silver-core gold-shell (Ag@Au) bimetallic nanoparticles can be an excellent alternative for SMSERS. Herein, we present the experimental evidence of SMSERS sensitivity of Ag@Au bimetallic nanoparticles by employing bi-analyte method. Additionally, by detecting resonant molecules at femto-molar concentrations, we show

that Ag@Au bimetallic nanoparticles can be harnessed for ultra-sensitive detection of molecules. The evidence provided will further motivate usage of such gold-shell based bi-metallic nanostructures for SMSERS in biological environments.

3.2 Experimental Section

3.2.1 Synthesis

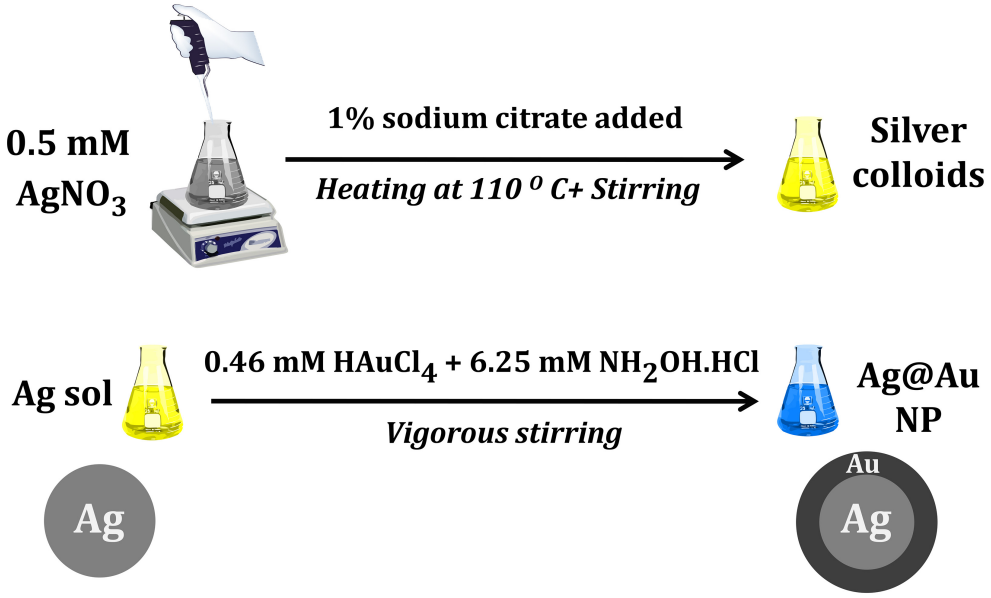

Figure 3.1: Schematic of the synthesis steps of Ag@Au bimetallic nanoparticles using citrate reduced Ag nanoparticles as seeds.

Silver and gold nanoparticles were synthesized by following Lee and Meisel's citrate reduction procedure[102].

• **Ag nanoparticles:** 250mL, 5.3×10^{-4}M aqueous solution of $AgNO_3$ was heated and brought to boiling using a magnetic stirrer cum hot plate. Then 5mL of 1% sodium citrate solution was added while stirring the solution and kept for $\sim$ 1 hour. A greenish yellow colour appeared gradually with the formation of the colloidal silver nanoparticles.

• **Au nanoparticles:** 250mL, 6.7×10^{-4}M aqueous solution of $HAuCl_4$ was heated and brought to boiling using a magnetic stirrer cum hot plate. Then 20mL of 1% sodium

citrate solution was added while stirring the solution and kept for ~ 1 hour. A wine-red colour appeared gradually with the formation of the colloidal gold nanoparticles.

• **Ag@Au nanoparticles:** Ag@Au nanoparticles were prepared by seed-growth method, using citrate-reduced Ag colloidal nanoparticles as seeds[103–105]; schematically shown in figure 3.1. 12.5mL Ag colloidal solution was diluted with 10mL of mili-Q water, and 'V' mL of 6.25×10^{-3}M NH_2OH;HCl and 'V' mL of 4.65×10^{-4}M $HAuCl_4$ were added drop wise (ca. 2mL/min) by two separate pipettes with vigorous stirring. The amount of $HAuCl_4$, here, governs the Au to Ag ratio. In our experiment we varied 'V' mL in different proportions starting from 2mL to 9mL to get different Ag@Au nanoparticles with different Au to Ag ratios. The stirring was continued for 45 min to complete the reduction. The colour change was noticeable during the experiment. We prepared six samples of Ag@Au colloidal nanoparticles with various Au to Ag ratio and they had different colours shown in the next section 3.3 (figure 3.5).

3.2.2 Characterization

The localised surface plasmon resonance (LSPR) of the colloidal nanoparticles were characterized by UV-Vis absorption spectrometer. For our SMSERS experiment we utilized the Ag@Au nanoparticles with LSPR of 490nm. The morphology of this particular batch of Ag@Au nanoparticles was studied through transmission electron microscope (FEI Tecnai F20, 200kV). Figure 3.2a shows transmission electron microscopy (TEM) image of an individual Ag@Au nanoparticle. The size of the nanoparticles was between 50nm to 80nm. The average thickness of the gold shell was between 6nm to 8nm. Figure 3.2b shows a cluster of Ag@Au nanoparticles from the same batch of synthesis. Figure 3.2c compares the normalized plasmon resonance of Ag@Au bimetallic nanoparticles with pure Ag and Au nanoparticles. The Ag@Au nanoparticles that we used having plasmon resonance around 490 nm which was in between the plasmon peaks of Ag (420nm) and Au nanoparticles (523nm).

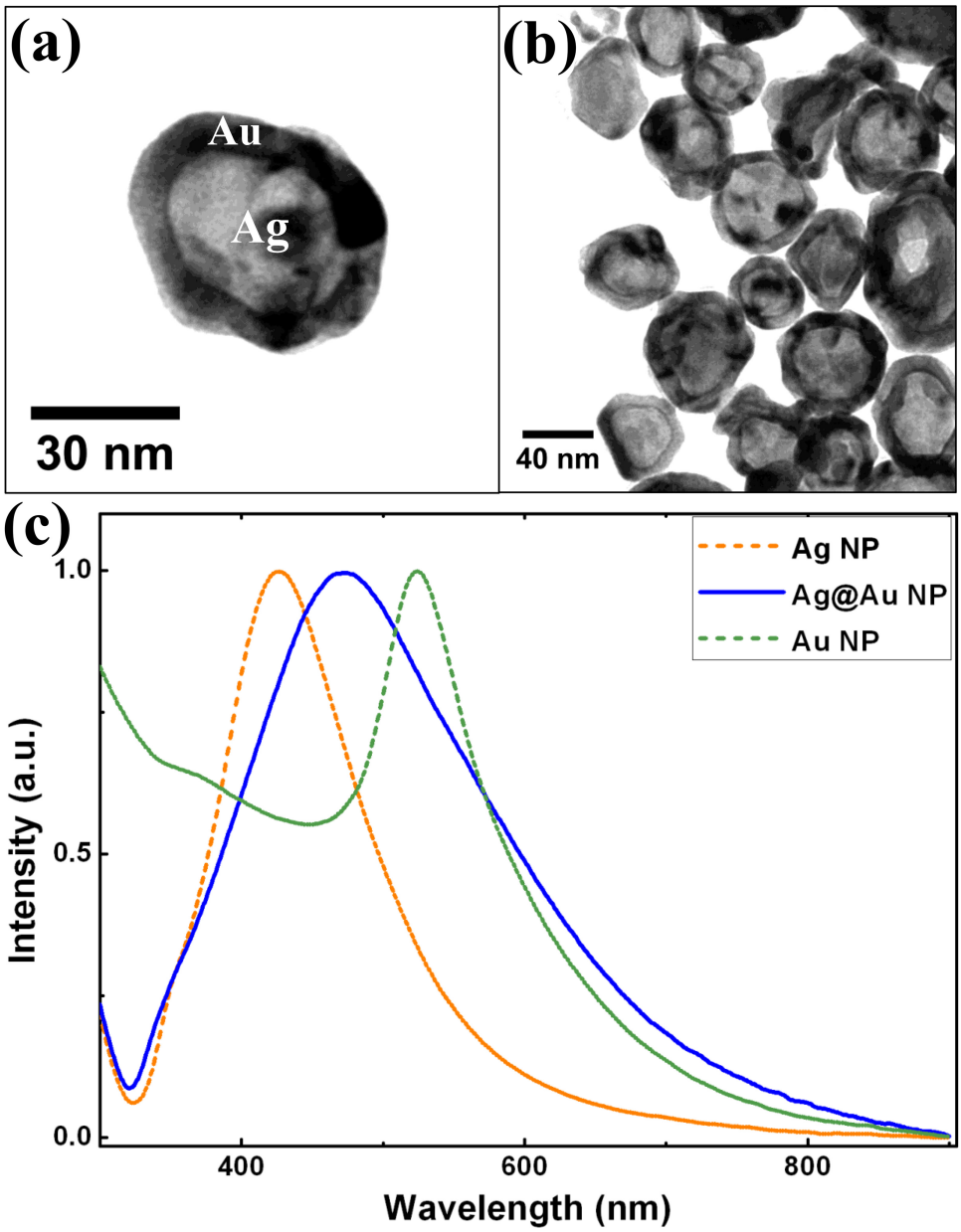

Figure 3.2: Morphology of Ag@Au bimetallic nanoparticles and their localized surface plasmon resonance (LSPR). (a) TEM image of single Ag@Au nanoparticle with Au shell thickness approximately equal to 8nm; (b) TEM image of cluster of Ag@Au nanoparticles used for SM-SERS; (c) LSPR of Ag@Au nanoparticles compared with Ag and Au nanoparticle prepared by citrate-reduction method. Ag@Au nanoparticles resonance is at 490nm. Ag and Au nanoparticless have resonance at 420nm and 523nm, respectively.

3.2.3 Sample preparation

In this experiment we utilized the solution based SERS measurements. To inspect the SERS enhancement of the prepared colloidal substrates, as a probe 2-naphthalenethiol

(2-NAT) molecule was mixed with all the nanoparticle solutions. The final concentration of the mixture solution was 1μM. For this experiment no aggregating agent was mixed to facilitate electromagnetic hot-spots.

The sample preparation plays a crucial role for bi-analyte single-molecule SERS[106]. We chose two dye molecules, Rhodamine-6G chloride (R6G) and Nile blue chloride (NB) as the two analytes and Ag@Au nanoparticles (with LSPR peak at 490nm) as the SERS substrate. For the experiment, equal volume of Ag@Au nanoparticles solution and 20mM KCl aqueous solution were mixed such that final KCl conc. was 10mM. This would reduce the Coulombic repulsion between the colloidal particles and trigger a partial aggregation of the colloidal particles to facilitate electromagnetic hot-spots[53, 107]. In such a condition, the colloidal solution remains stable for weeks. Now the partially aggregated solution was diluted with pure water three/four times to the initial volume. Then two analytes, R6G and NB were first premixed together and then added to the colloidal solution so that the final analyte-concentration remained 2nM. This solution mixture was then kept for at least $6-8$ hours to equilibrate the adsorption of the analyte molecules to the nanoparticles. Before every measurement the solution mixture was sonicated to homogenize.

3.2.4 Instrumentation and signal collection

All the SERS spectra were recorded in a focused field excitation geometry. For this purpose a high-resolution confocal Raman microscope (LabRam HR, Horbia Jobin Yvon, France) was used. A schematic diagram of confocal Raman microscope is shown in figure 3.3. In such Raman microscopes[108], a desired LASER line is focused through an objective lens on to the samples. The back scattered light is collected by the same objective lens and by passing through a confocal pin-hole, focused on the spectrometer. A highly sensitive charge-coupled device (CCD) photo-detector is used to detect the scattered photons. A long pass filter (i.e. Edge filter) or a band stop filter (i.e. Notch filter) is used to reject the high intensity Rayleigh scattered photons in order to detect Raman signals (either Stokes or anti-Stokes or both). The lateral (XY) spatial resolution depends on the diffraction limit of the objective lens for a given excitation wavelength, i.e. $d = \lambda/2NA$, where, lambda is the excitation wavelength and NA is the numerical

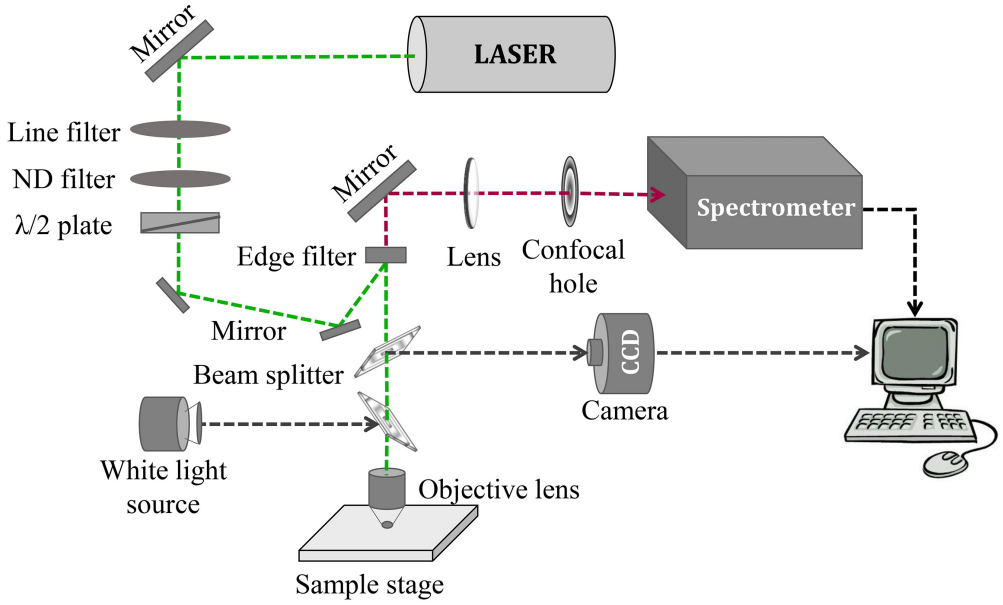

Figure 3.3: Schematic diagram of a confocal Raman microscopy system.

aperture ($NA = nsin\theta$) of the objective lens. The depth (Z) spatial resolution depends on the confocal design of the microscope[109, 110].

For our solution based SERS experiment, a $\times 60$ water immersion objective lens (NA=1) that was dipped into 40μL droplet of the sample solution on a ultra-clean glass slide. A 532nm laser line of 7.8mW power was used for SMSERS experiment as excitation source. The acquisition time for each spectrum for SERS enhancement calculation (using 2-NAT as probe molecule) was 1s. For SMSERS and trace detection experiment a series of SERS signals were collected with acquisition time of 100ms and dwell time between two consecutive spectra was 1s. The resolution of the spectrometer was approximately 0.1cm^{-1}.

3.3 Results and Discussion

3.3.1 Novelty of Ag@Au substrates

An important aspect of single-molecule SERS is the plasmonic substrate utilized to obtain large scale electromagnetic enhancement. In most of the single-molecule SERS studies, silver nanoparticles have been utilized because, at visible frequencies, Ag has

Table 3.1: SERS analytical enhancement factor(AEF) for gold, silver and Ag@Au(Au:Ag=0.1) bimetallic nanoparticles calculated using 1μM of 2-naphthlenethiol (2-NAT) as a probe with three different excitation-wavelengths. The LASER powers are indicated within brackets. All measurement were performed without aggregating agents.

$$\mathbf{AEF} = (\mathbf{I_{SERS}/I_{Raman}}) \times (\mathbf{C_{Raman}/C_{SERS}})$$

where $\mathbf{I_{Raman}}$ and $\mathbf{I_{SERS}}$ are intensities of a particular vibrational mode for normal-Raman and SERS experiments, respectively. $\mathbf{C_{Raman}}$ and $\mathbf{C_{SERS}}$ are concentrations of the probe molecule used in normal-Raman and SERS experiments, respectively.

Excitation wavelength	**Raman modes of 2-NAT**	**Analytical enhancement factor**		
		Gold(Au) nanoparticles	***Ag@Au nanoparticles***	***Silver(Ag) nanoparticles***
532nm (15mW)	C-H bending ($1080cm^{-1}$)	No SERS	4.0×10^7	3.1×10^7
	Ring streching ($1378cm^{-1}$)	No SERS	6.5×10^6	4.3×10^6
633nm (11mW)	C-H bending ($1080cm^{-1}$)	3.8×10^6	2.7×10^8	1.0×10^7
	Ring streching ($1378cm^{-1}$)	1.3×10^6	4.1×10^7	4.2×10^6
785nm (35mW)	C-H bending ($1080cm^{-1}$)	6.5×10^8	5.0×10^9	1.4×10^8
	Ring streching ($1378cm^{-1}$)	4.0×10^8	1.7×10^9	1.2×10^8

the best plasmonic enhancement[48]. Then why should one use Ag@Au bimetallic nanostructures for SMSERS over the conventional silver? The answer is as follows.

- **Large SERS enhancement with stability and non-toxicity**

The major problems with silver based nanostructures are oxidation and toxicity issue[97, 111]. As an alternative to this, well-prepared gold nanoparticles can be very stable, biocompatible and also SERS active, but their plasmonic enhancement is lesser than Ag nanostructures, and hence it is difficult to harness them for single-molecule SERS studies. If plasmonic nano-probes have to be utilized for single-molecule SERS detection in biological environments, then they need to satisfy two important criteria: (i) to facilitate large Raman enhancement factors for single-molecule sensitivity; and (ii) having surface properties that are compatible with bio-environment.

One such plasmonic nano-architecture that satisfies the above mentioned criteria is

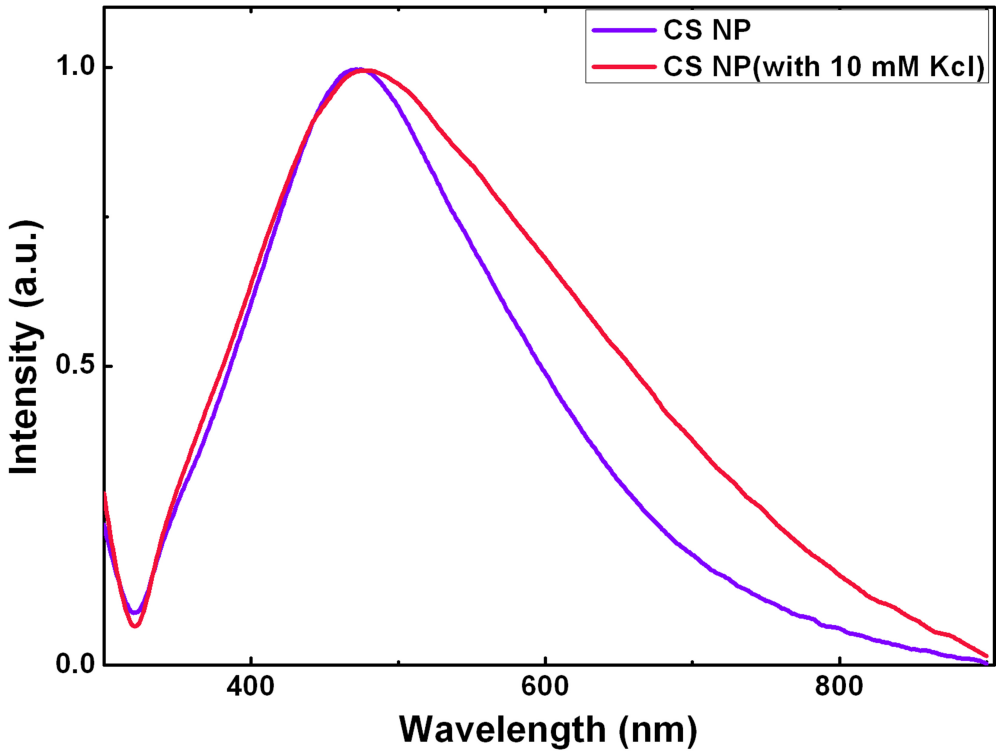

Figure 3.4: UV-Vis absorption spectra of core-shell nanoparticles (Au: Ag=0.1) solution with and without adding the aggregating agent, KCl (10mM aqueous solution).

silver-core gold-shell (Ag@Au) bimetallic nanoparticles[104, 105]. Since such nanoparticles have gold shell, they are stable and expected to be biocompatible and they also facilitate large scale Raman scattering enhancements comparable to Ag nanoparticles. A systematic comparison of SERS enhancement factors (without adding any aggregating agent to the colloidal nanoparticles) between bimetallic-Ag@Au, pure Ag and pure Au nanoparticles for three excitation wavelengths is charted in table 3.1. We observed that our prepared Ag@Au nanoparticles (LSPR, 490nm) are excellent candidates for SERS studies, and the average SERS enhancement factor (without nanoparticle aggregating agents) at 532nm excitation for C-H bending mode of 2-napthalenethiol was around 4×10^7, which was on par with Ag nanoparticles. In single-molecule SERS studies, as mentioned earlier (section 3.2.3), KCl is used for mild aggregation of the colloidal nanoparticles which triggers further enhancement of the SERS signal[53]. In our case, the effect of addition of 10mM KCl was to slightly red-shift the plasmon peak and broaden the full width at half maxima of the Ag@Au nanoparticles, as shown in figure 3.4. Addition of KCl obviously, further increases the SERS enhancement factor

by a order or two than that of unaggregated nanoparticles, which is sufficiently large for single-molecule SERS studies[90, 112].

- **Tuneable LSPR**

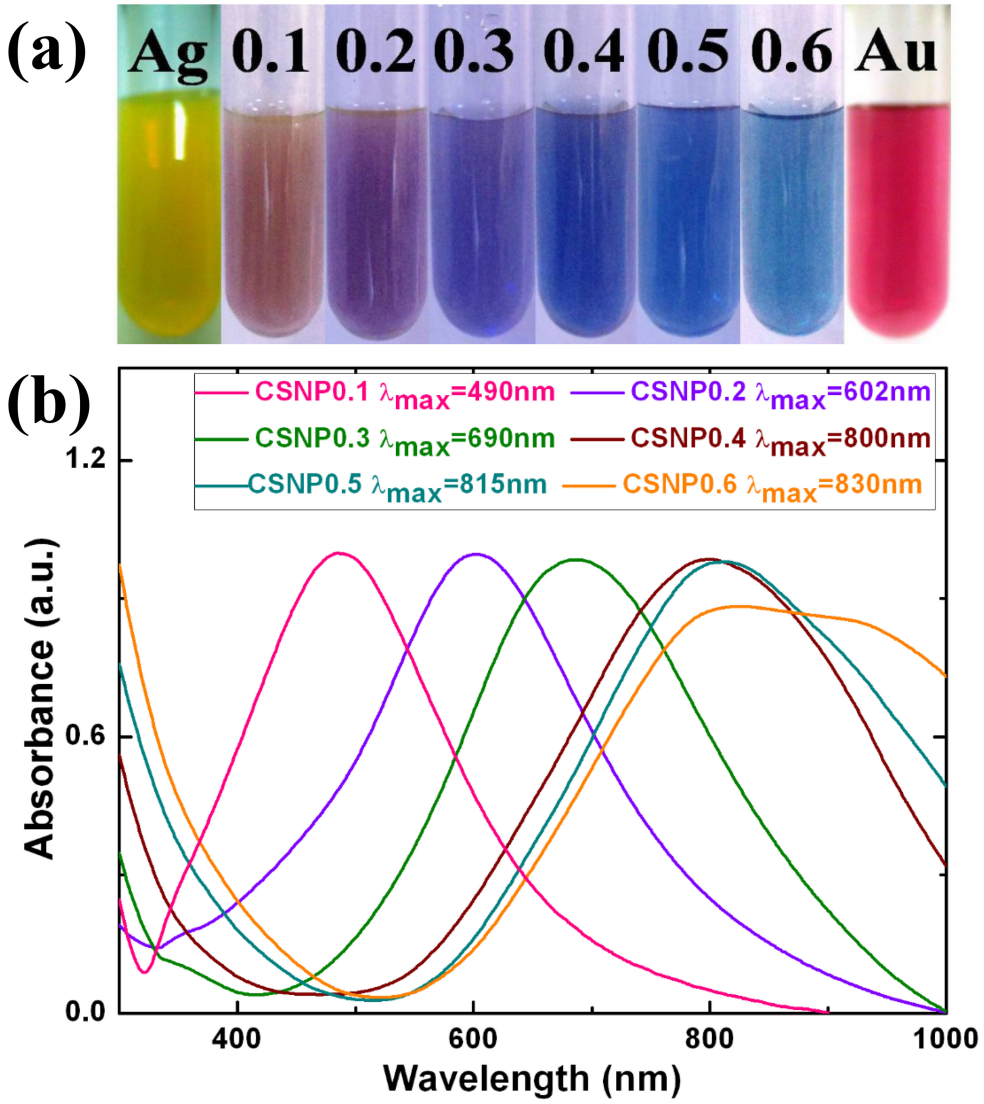

Figure 3.5: (a) Photographs of the silver (Ag), gold (Au) and Ag@Au core-shell nanoparticles (CSNP) colloidal nanoparticles solutions in test-tubes. (b) UV-Vis absorption spectra of core-shell nanoparticles with different Au to Ag ratio. The fractional numbers are written as per the amount of AuCl4 added to the Ag colloids. This increases the thickness of the Au shell.

One of the major advantages of Ag@Au nanoparticles is that by varying the thickness of the Au shell, one can systematically vary the plasmon resonance of nanoparticles as shown in the figure 3.5. We can see that the LSPR can be easily tuned from 490nm to 900nm. Such wide range LSPR tuning is very difficult to achieve utilizing pure silver

or gold zero-dimensional nanostructures, even by changing the shape.

- **Intra-band transition**

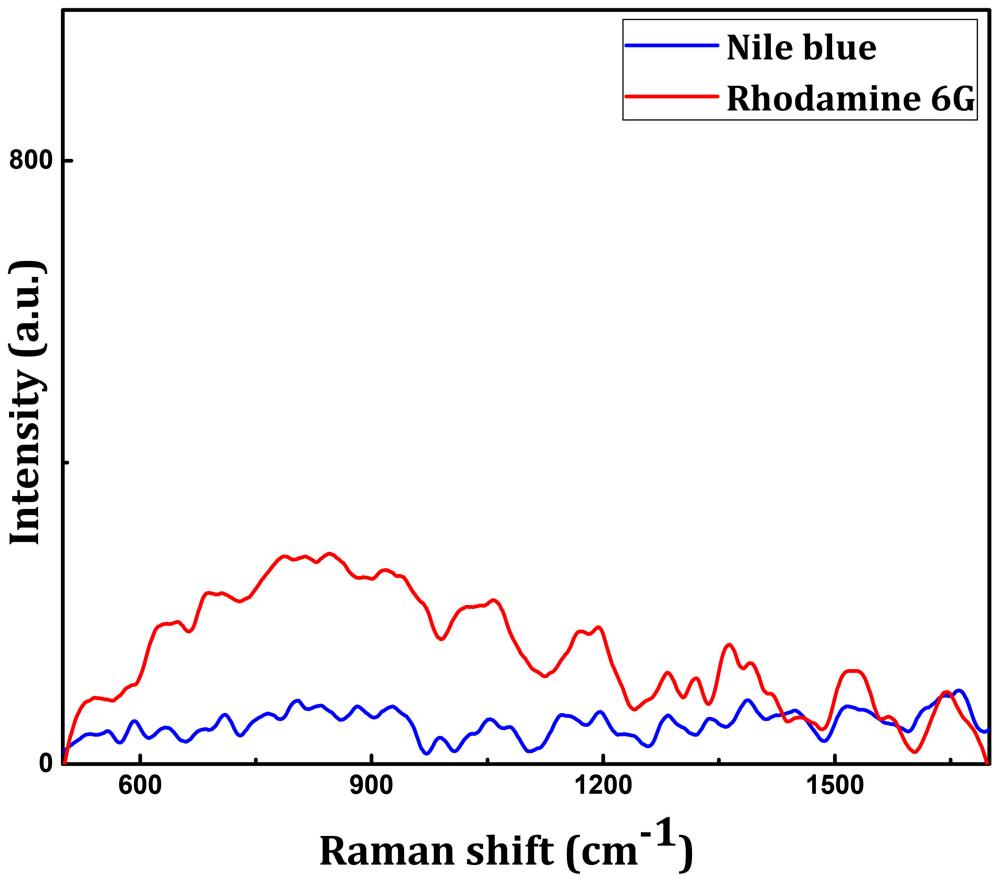

Figure 3.6: SERS spectra of 0.05μM Nile blue and Rhodmine-6G with gold colloids at 532nm excitation; 10s accumulation time. No signal was evident. The hump in the R6G spectrum is due to the mild unquenched fluorescence from the molecules, since at 532nm R6G has an electronic transition.

Another important point to note is that Ag@Au nanoparticles are SERS active at 532nm excitation, whereas pure gold based nanostructures do not exhibit SERS due to intra-band electronic transitions[48] as indicated in figure 3.6. Thus, Ag@Au nanoparticles can provide a gold environment to the analytes as well as a SERS detection capability at a wavelength below 600nm, where gold nanostructures are not viable due to intra-band transition.

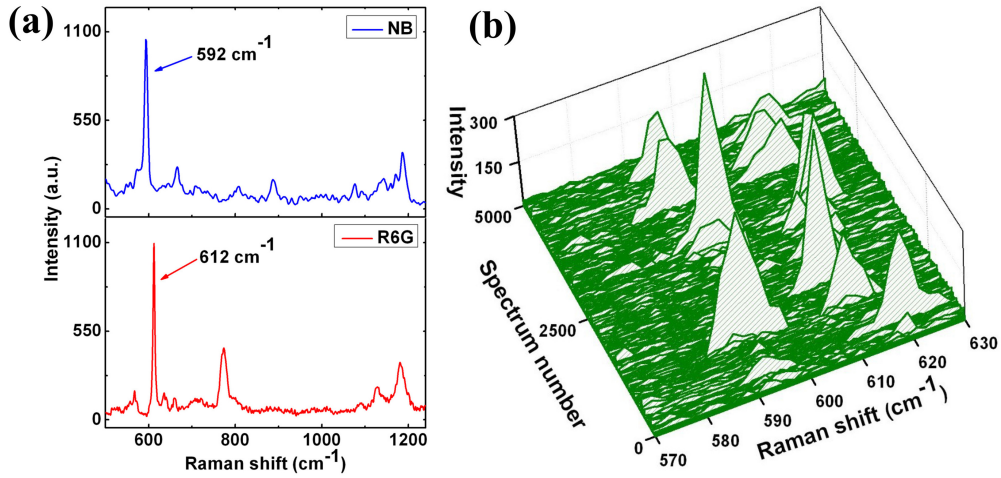

Figure 3.7: (a) Individual SERS spectrum of Nile blue (NB) and Rhodamine 6G (R6G) collected with Ag core Au shell nanoparticles at concentration equal to 50nM. Signal acquisition time = 10 sec. For the single-molecule SERS analysis with bi-analyte approach, the two indicated modes: 592cm^{-1} in NB and 612cm^{-1} in R6G were chosen; (b) Series of bi-analyte SERS spectra recorded using bi-analyte method. Only 5000 spectra out of the 15000 are displayed. The concentration of NB and R6G were 2nM. Signal acquisition time = 0.1 second. Fluctuations in the intensity of the above mentioned modes were clearly observed. All the experiments were performed using 532nm excitation.

3.3.2 Bi-analyte single-molecule SERS

We utilized Ag@Au nanoparticles for single-molecule SERS detection using bi-analyte method developed by Etchegoin and Ru [53, 94] as discussed in chapter 2, section 2.1.2. Precisely, bi-analyte single-molecule SERS method uses two different analytes, and is a contrast-based spectroscopic technique that does not rely on the ratio of number of analytes to nanoparticles[53]. Furthermore, this method facilitates reliable statistics from a large spectral sampling-size for single-molecule analysis. For the present case, the two types of dye molecules, Nile blue (NB) and Rhodamine 6G (R6G) were used along with Ag@Au nanoparticles to perform the experiments. The individual SERS spectra separately recorded for each dye at 532nm excitation are shown in figure 3.7a. The two closely-spaced modes at 592cm^{-1} in NB and 612cm^{-1} in R6G were used for the bi-analyte single-molecule SERS experiments. Figure 3.7b shows a series of bi-analyte SERS signals of the above mentioned modes in combination (each molecule at 2nM concentration, accumulation time = 0.1sec, 532nm excitation). It was clearly evident from figure 3.7b that signals from two molecules fluctuate as a function of time.

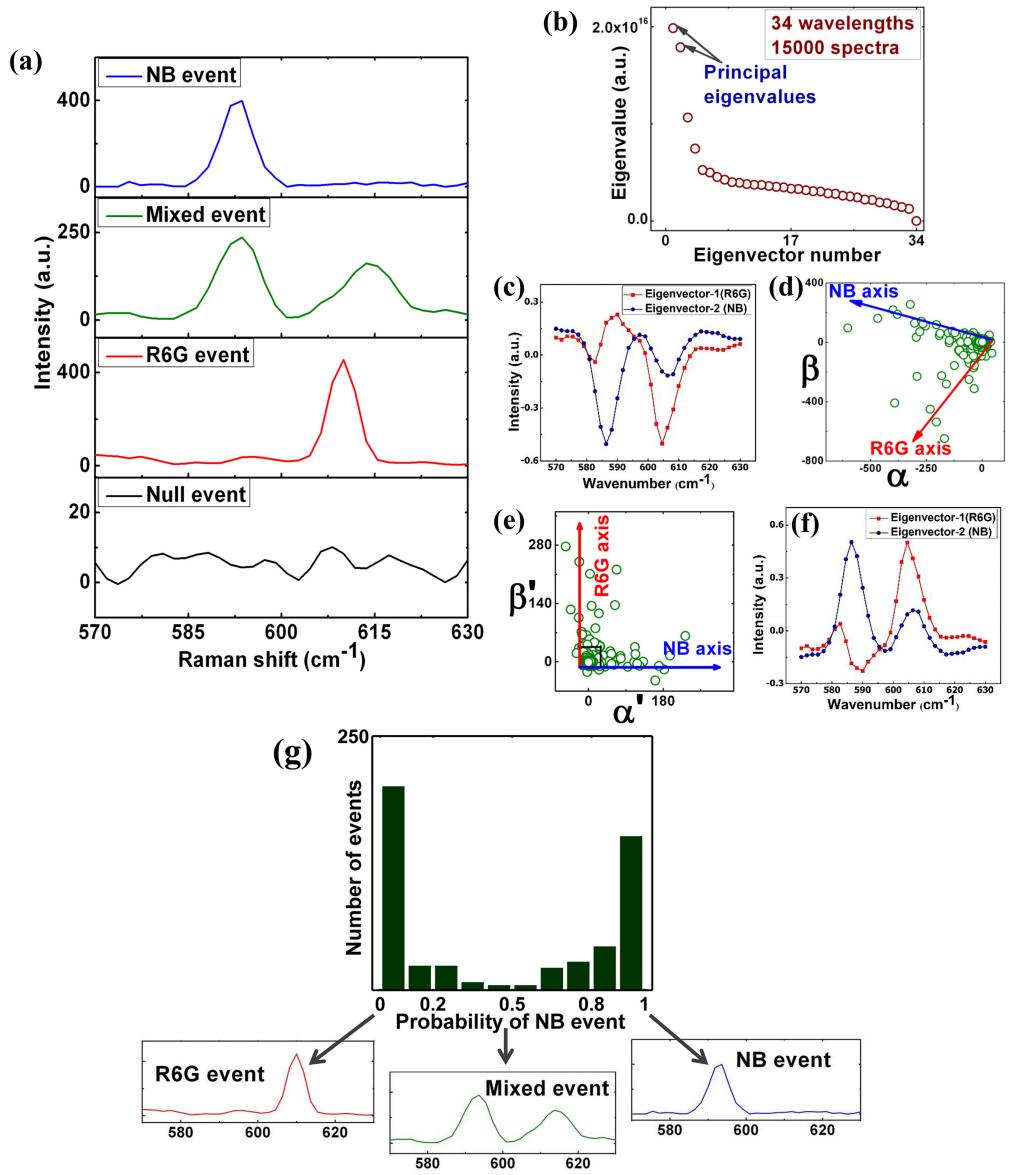

Figure 3.8: Analysis of bi-analyte single-molecule surface enhanced Raman scattering with Ag@Au NPs as substrates. (a) Four possible bi-analyte SERS events from 15000 spectra (acquisition time 0.1s) for two dyes at 2nM concentration with Ag@Au NPs at 532nm excitation. (b) Eigenvalues (in decreasing order) obtained from PCA analysis of 15000 spectra consisting of 34 wavelengths containing the 592cm^{-1} and 612cm^{-1} mode of NB and R6G, respectively. (c)Plot of two principal eigenvectors as a function of wavenumber, denoting actually the SERS signatures of R6G and NB dyes but in a new coordinate system (d) Plot showing the distribution of the covariant matrix coefficients obtained from PCA analysis. e) Coefficient-plot after linear transformation along the axes. Note that the axis is now orthogonal and rescaled. (f) Eigenvector vs. wavenumber plot after transformation. (g) Probability of NB events retained from 15000 spectra after discarding the noisy events. The cut-off is indicated by a black square in (e).

Next, we analysed the collected data (sample size=15000 spectra) by modified principal component analysis to ascertain single-molecule detection capability of Ag@Au

nanoparticles. Figure 3.8a shows the four probable spectral event that one obtains in bi-analyte approach, mentioned earlier (chapter 2, section 2.1.2). The bottom spectrum pertains to no signal from either of the molecules. The next spectrum shows a pure R6G event. Stacked on this spectrum is a mixed event where signals from both R6G and NB was clearly evident, and the top-most spectrum indicates a pure NB event.

To statistically prove single-molecule sensitivity, we followed the modified principal component analysis method developed by Etchegoin and co-workers[94] (discussed in chapter 2, section 2.2.2): (1) All the collected spectra (15000) were condensed into a rectangular matrix M of T rows and N columns, where T and N are the number of spectrum and wavenumber, respectively. (2) For each row of the matrix, the mean intensity was subtracted to obtain the zero mean intensity matrix ($\hat{M}$). This is a standard procedure of principal component analysis. (3) The covariance matrix V was computed for the matrix $\hat{M}$. (4) The eigenvalues and eigenvectors of the covariance matrix V were computed. These are plotted in figure 3.8b. In the context of bi-analyte method, the two eigenvectors with maximum eigenvalues from the covariance matrix are important (figure 3.8b). These two eigenvectors are the principal components of our data, which actually represent the two analytes' SERS signatures but in a transformed coordinate (figure 3.8c). (5) The next step was to obtain the coefficient matrix C by a matrix operation equivalent to scalar product of spectra with first two eigenvectors. (6) Further, the matrix C was plotted in the co-efficient space as shown in figure 3.8d, where each point in the plot represents an event. Each axis (α or β) in the plot represents pure spectra of either R6G or NB. (7) A linear transformation is applied to rescale and reorient the axis in co-efficient space (with new axes α' and β') as shown in figure 3.8e. This is done to obtain only the positive coefficients that represent the actual spectra of the analytes (figure 3.8f). The new axes (α' and β') are now orthogonal to one another, and the transformed coefficients are direct representation of average number of the molecules participating in the events. (8) The final step was to obtain the probability histogram (figure 3.8g) that represents the relative contribution of the number of molecules to the total signal (the plotted histogram is for NB). This is given by $p_{analyte_1} = 1/(1 + y/x)$ where (x, y) are the co-ordinates in figure 3.8e. We introduced a cut-off to remove the background noise, and it was verified that the retained signal was well above the noise

limit.

Figure 3.8g is the central result of this letter. The main contribution to the distribution in histogram (figure 3.8g) is from NB events whose probability is either 0 or 1. The edge regimes of the histogram indicate single-molecule events with high probability. This result therefore, implies that Ag@Au nanoparticles are sensitive enough to detect spectroscopic signatures at single-molecule regime.

3.3.3 Trace detection

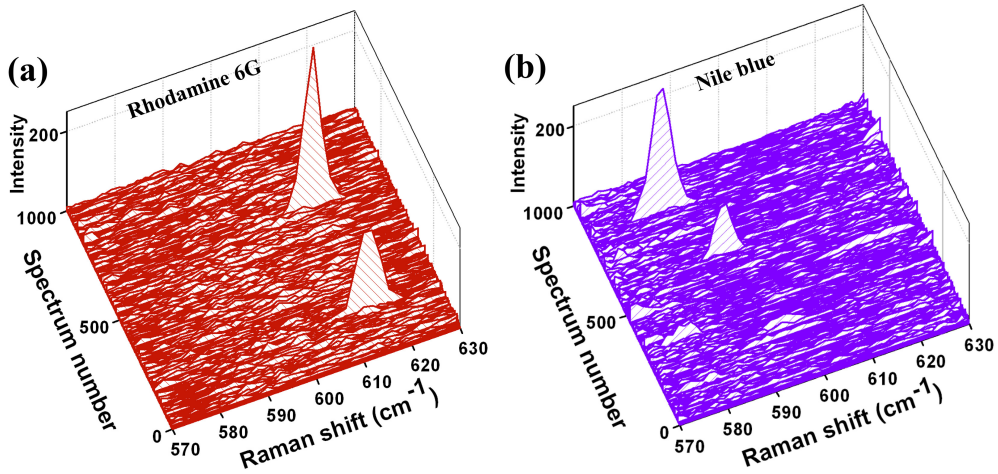

Figure 3.9: (a) 1000 SERRS spectra collected from 5fM R6G with Ag@Au NPs at 532nm excitation (which is in resonance with electronic transition of R6G dye) at 7.8mW power; (b) 1000 SERRS spectra collected from 5fM Nile blue with Ag@Au NP at 633nm excitation (which is in resonance with electronic transition of NB dye) at 5.8mW power. Acquisition time for each spectrum was 0.1 s for both the cases.

Can Ag@Au NPs be harnessed for ultra-sensitive detection of molecules? To answer this question we performed a 'proof of principle' experiment, where we utilized surface-enhanced *resonance* Raman scattering (SERRS) instead of regular SERS. In SERRS experiment the excitation laser wavelength must be in resonance with the electronic absorption of the analyte molecule[51, 87, 113, 114]. Thus, we utilized 532nm excitation for R6G dye molecules and 633nm excitation for NB molecules. Figure 3.9 shows the data collected from a sample of 1000 spectra for the two dyes. Out of this sampling size, we could detect two high intensity spectral events for each analyte with clear signature of both R6G (612cm^{-1}) and NB (592cm^{-1}) molecules. All these data

further corroborate excellent sensitivity of Ag@Au nanoparticles at extremely low concentrations of molecules and at multiple wavelengths. Such ultra-sensitive gold-shell based nanoparticles can be excellent candidates to be used in biological systems.

3.4 Summary

To summarize, in this chapter we have provided, to the best of our knowledge, the first experimental proof of single-molecule SERS sensitivity of Ag@Au bimetallic nanoparticles using bi-analyte strategy. Since these bimetallic nano-shell based ultrasensitive probes have Au on their surface, they can be further chemically-functionalized with various biomolecules and harnessed as single-molecule SERS probes in biological environments such as cells and tissues. Importantly, the plasmon resonance of Ag@Au nanoparticles can be easily tuned from visible to near-IR, making them versatile nanostructures for multi-wavelength bio-imaging. Furthermore, these nanostructures can be adapted to prepare plasmonic nano-constructs with sequestered molecules[115, 116]. Such innovations can be of great use in quantitative single-molecule SERS studies.

Chapter 4

Single-molecule SERS using Evanescent-field Microscopy

Chapter 4 is an adaptation of the research article, '*Nature Communications, 5, 4357 (2014)*'. The article dwells on how to harness a single evanescent-wave excitation to create electromagnetic hot-spots by assembling colloidal nanoparticles without any chemical means and simultaneously to detect single molecule SERS signals from them.

4.1 Introduction

In the previous chapter, we have discussed about the solution phase single-molecule SERS sensitivity of Ag@Au bimetallic nanoparticles in focused field excitation. There, our main goal was to modulate the localised surface plasmon polariton (L-SPP) towards maximum electromagnetic field intensity to sense single molecules through SERS with a desired composition of the plasmonic substrate. Besides L-SPP, as we have discussed earlier (chapter 1 section 1.2.1), there is another variety of surface plasmon polariton, called propagating surface plasmon polariton (P-SPP) and can be produced on a variety of platforms e.g. films, nanowires etc[117]. In this chapter, we shall talk about the SMSERS experiment which utilizes both L-SPP and P-SPP.

One of the objectives of this work was to integrate SMSERS with plasmon-assisted optical assembly of nanoparticles in solution. This integration is advantageous, especially in the context of optofluidics[118], for the following reason. In most of the solution-phase SMSERS experiments[50, 53, 83, 119] the plasmonic hot-spots are facilitated by adding chemical aggregating agent such as NaCl or KCl. These chemicals

agglomerate the nanoparticles irreversibly, and hence the aggregates cannot be further used as uniformly dispersed, plasmonic nanoscale entities. Also, such a procedure of aggregation is not conducive for micro/nano-fluidic environments, where a relatively small aggregate can block the flow of the liquid. Therefore, there is an imperative need to temporarily assemble nanoparticles in a controlled way, and re-disperse them back in the fluid after SMSERS interrogation.

Here, we discuss how to combine single-molecule SERS with plasmon-assisted assembly and manipulation of metal nanoparticles without the use of aggregating agents. Importantly, a single evanescent-wave optical excitation was used to achieve both plasmonic assembly and single-molecule SERS, simultaneously. To the best of our knowledge, this was the first work on solution-phase SMSERS experiments on dynamic assembly of metal nanoparticles by evanescent-wave excitation of plasmons. By harnessing the optical fields created by SPPs in a metal film, we create large-area assembly of metal nanoparticles, and further utilize the combination of P-SPP and L-SPP fields to capture single-molecule SERS signatures at metal-fluid interface. In addition to this, we show the potential of our method to achieve dynamic, large-area lithography of nanoparticles at metal-fluid interface by employing dual-optical excitation in total-internal reflection geometry.

4.2 Experimental Section

4.2.1 Materials preparation and characterization

Preparation of metal thin films:

Plasmonic thin films were prepared using direct current (DC) sputtering process. This type of material deposition is attained by passing a high voltage electric current through an inert gas (e.g. argon) environment. The high energy plasma created causes rapidly accelerated ions to strike the target material (in our case Gold or Silver), displacing its atoms. The donor atoms then strike and adhere to the substrate (in our case Glass Coverslip) at an atomic level and create a very thin and smooth film with a desired thickness. The inert gas ambience is maintained at very low pressures, typically down

to 0.5mTorr. A negative DC high voltage is then applied to the recipient material via a magnetron. This negative charge attracts the donor atoms displaced by the gas plasma. By this technique, very smooth thin films can be deposited on various materials with a high precision of thickness.

For plasmonic thin film substrates, glass coverslips were used as the base material. The glass coverslips were first cleaned thoroughly with acetone and isopropanol and dried in a desiccator. Then DC sputtering technique was employed to deposit 40nm thick gold or silver on the glass-cover slip at very slow rate (ca.0.1 Å per second) to get a smooth thin film. The thickness of the metal film was $40(\pm 5)$nm.

Preparation of metallic nanoparticles:

In this work silver, gold and silver-core gold-shell (Ag@Au) bimetallic nanoparticles were utilised. The preparation and characterization of the nanoparticles were described in the previous chapter, section 3.2.1.

The prepared nanoparticles were characterized with same techniques as discussed in chapter 3, section 3.2.2.

4.2.2 Sample preparation

Single-molecule SERS experiments:

Ag@Au nanoparticles were mixed with two equimolarly premixed dye molecules, Nile blue chloride (NB) and Rhodamine 6G chloride (R6G) such that the final concentration of dye molecules was 5nM. The solution mixture was kept for 6-8 hours to equilibrate the adsorption process. *It is to be noted that there were no external aggregating agents used for activation of hot-spots*.

For concentration dependent SERS measurements, all the parameters of the experiments were held same as single molecule SERS studies except the molecular concentration. Four such experiments were done using dye concentration of 200nM (bi-analyte), 50nM (R6G), 10pM (R6G) and 1fM (R6G).

Nanoparticles-assembly experiments:

For nanoparticles assembly experiments, two metal films (gold and silver) and three types of nanoparticles (Ag, Ag@Au and Au) were used for comparative study. As per

the synthesis protocol the number density of the colloidal nanoparticles in solution for the three types, Ag, Au and Ag@Au nanoparticles might differ from each other. Thus, the colloidal nanoparticles were diluted in water such that the number of nanoparticles/mL remained almost same for every colloidal solution used in different experiments. The metal film thickness was kept constant to 40nm for both silver and gold films.

4.2.3 Instrumentation and signal collection

In this work we have used the confocal Raman microscopy (LabRam HR, 789mm focal length) but haven't utilised the focused-field excitation geometry attached with the system. Here this microscopy was used only for signal collection purpose. For the excitation we employed evanescent-waves, based on total internal reflection (TIR) geometry. A schematic diagram and a photograph of the evanescent-wave combined Raman microscopy are shown in figure 4.1.

Figure 4.1a shows the optical schematic of the set-up used for plasmon-assisted assembly of metal nanoparticles and SMSERS measurements. We used a Dove prism (N-BK7, refractive index$= 1.519$), on to which a silver-coated glass cover-slip was adhered through an optically-matched oil. The excitation source was a 532nm, continuous-wave, frequency doubled Nd:YAG laser (power=up to $200mW$) which was p-polarized by a $\lambda/2$-plate and routed into the prism for total internal reflection by weakly focusing lens L ($focallength = 150$mm). The angle of incidence at the interface was 72.70° from the normal to the surface.

For SMSERS experiments, 80μL of sample solution was drop casted on glass cover-slip pre-deposited with 40nm thick silver film. Series of SERS spectra were collected with the acquisition time of 0.1s for each spectrum; the refresh time for two consecutive spectra was 1s. The laser power was 20 mW before entering the prism. The signal collection spot was fixed to 5μm by keeping the confocal hole size as 400μm. Water immersion $\times 60$ objective lens (NA$= 1$) was used for signal collection. The captured light was routed into the high resolution, confocal Raman spectrometer (789mm focal length) for analysis.

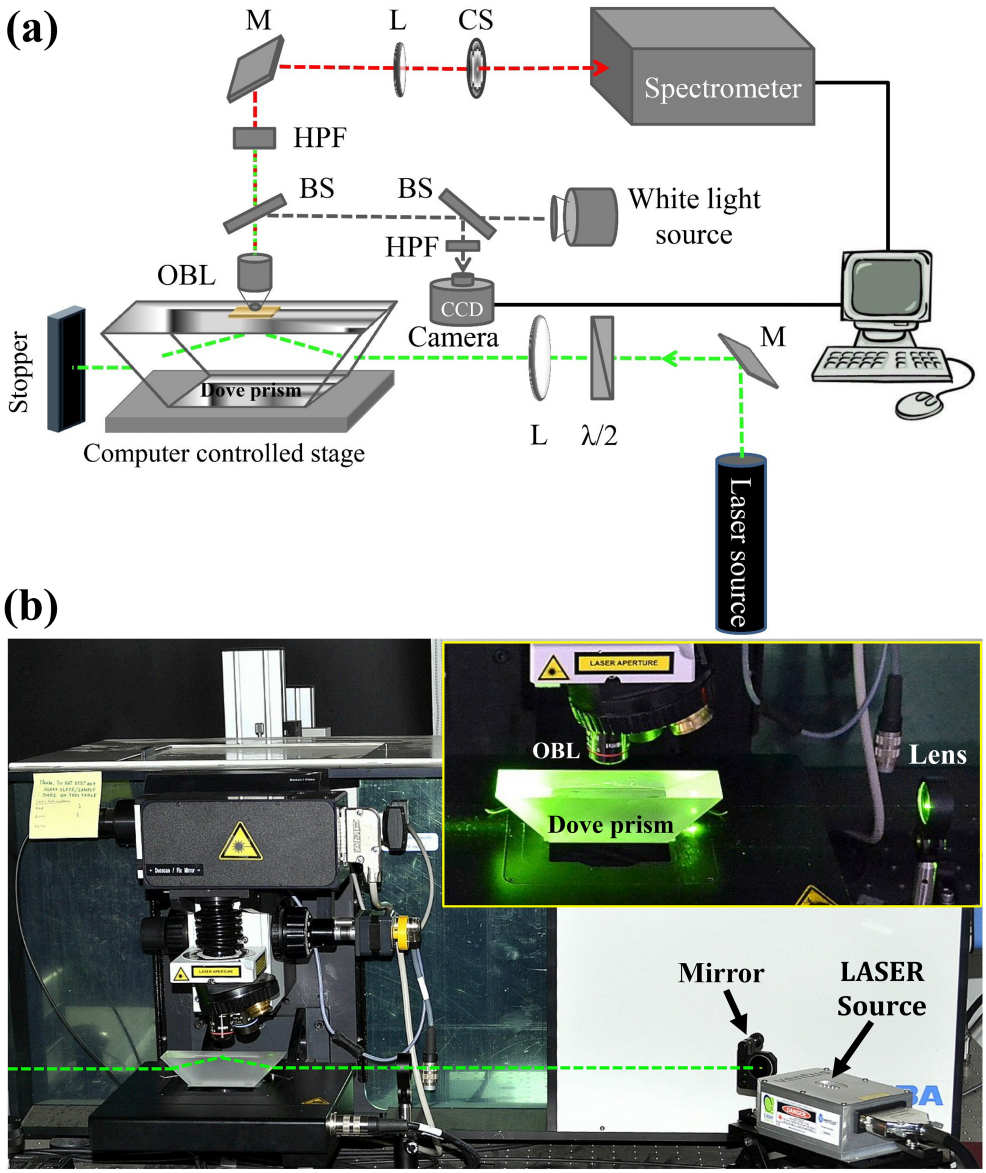

Figure 4.1: (a) Optical set-up of confocal Raman detection microscope coupled with Dove-prism based plasmon excitation. (b) Photograph of the same set-up. Inset is a close-up view of the Dove-prism and objective lens.
The acronyms are, M-mirror, HPF-high pass filter, L-lens, CS-confocal slit, BS-beam splitter, OBL-objective lens, CCD - charged-coupled device, $\lambda/2$- half wave plate

For assembly experiments, 80μL colloidal solutions were dropped on to the metal film to observe the phenomena. The LASER power was kept 37mW before entering the prism throughout all trapping experiments. Videos and images were collected using $\times 4$ objective lens (NA$= 0.13$) and the captured light was routed towards the camera.

4.3 Results and Discussion

4.3.1 Combining plasmon-assisted assembly of nanoparticles with confocal SERS microscopy

We first addressed the issue of how to effectively employ a *single* evanescent-wave optical excitation at metal-fluid interface to *simultaneously* assemble plasmonic nanoparticles and perform Raman scattering. For this, we utilized total-internal reflection (TIR) based plasmonic excitation of an unstructured metal film in Kretschmann geometry[26, 27]. This plasmon-polariton excitation created an optical potential, which was further used to assemble and manipulate nanoparticles. Importantly, the same TIR illumination was also utilized for exciting SERS scattering from nanoparticles assembly.

In figure 4.1 we have shown the combination of confocal Raman microscopy and evanescent-wave excitation through TIR geometry utilizing a Dove-prism. Now the question arises that why this microscopic combination is so important for such assembly of nanoparticles. To answer this, we have to first investigate about the significance of the angle of excitation of a plasmonic thin film. Thus, we analytically calculated the angle dependent optical absorption for silver and gold thin film (40nm), shown in figure 4.2. Calculations are based on solving Fresnel's equation for TM waves in Kretschmann configuration. MATLAB code given by Etchegoin et al.[4] was implemented for calculation. We see that for silver thin film at the angle of incidence of 72.7° there is the maximum absorption at 532nm wavelength (figure 4.2a). Also for gold film the absorption at 532nm line is pretty high at this excitation angle (figure 4.2b).

Therefore, when a droplet of nanoparticles solution was placed on a thin plasmonic film and optically excited as per the above said excitation geometry, the nanoparticles got assembled at the metal-fluid interface very efficiently (shown in figure 4.3). Figure 4.3 depicts the plasmon-assisted assembly of Ag@Au bimetallic nanoparticles on a 40nm silver film upon excitation through the p-polarized Gaussian beam. The beam creates an elliptical projection upon total internal reflection at the metallic surface, which was imaged in figure 4.3b(left). This particular excitation profile acts as an optical potential, which was harnessed for plasmofluidic trapping and SMSERS measurements.

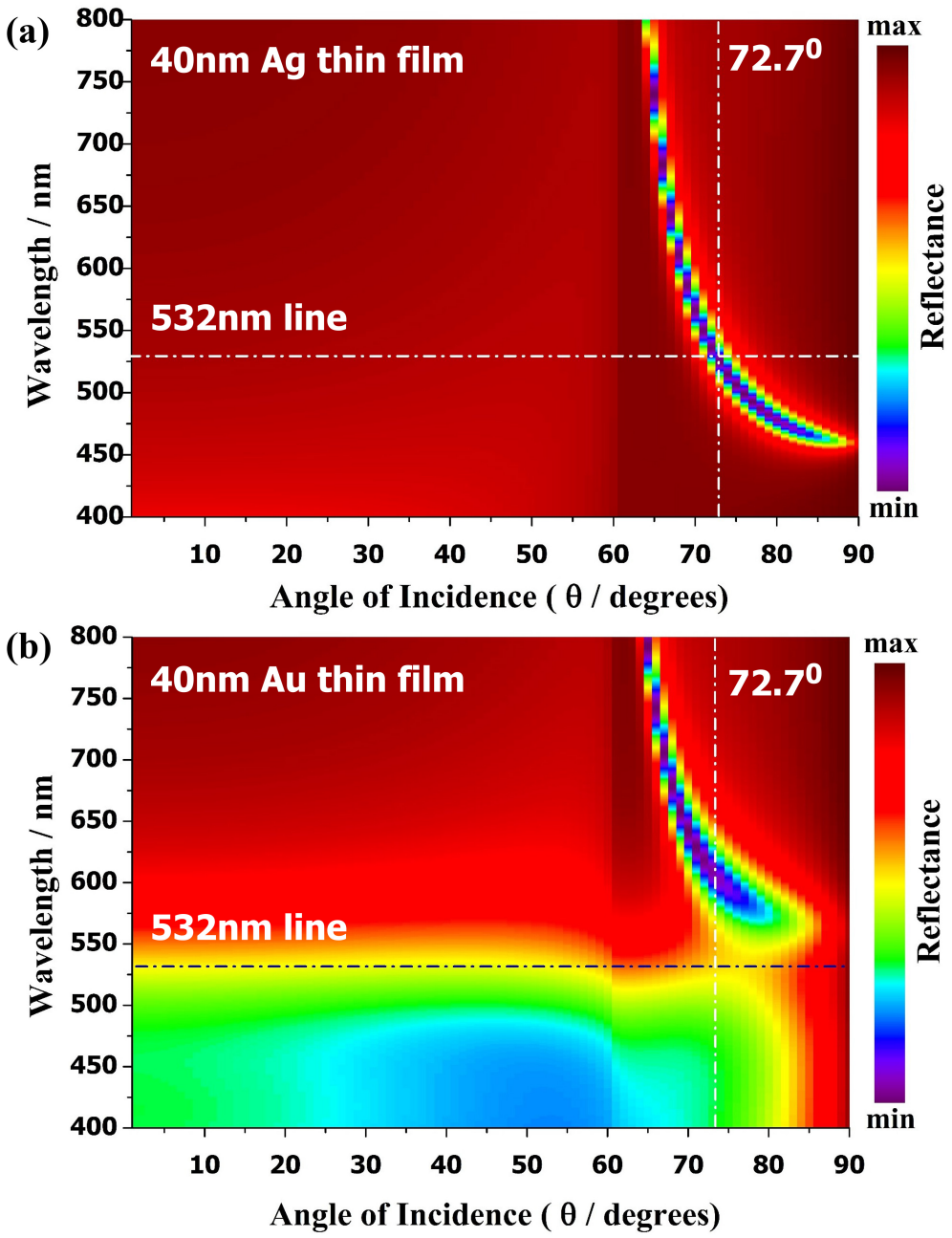

Figure 4.2: The angle dependent absorptions of 40nm silver film and 40nm gold film, calculated for the wavelength range from 400nm to 800nm. (a) For silver film, at fixed wavelength 532nm (indicated by a horizontal white line) which is used for our study, the absorption maximum is around 73° (indicated by a vertical white line) which matches with our experimental excitation geometry. (b) For gold film, at fixed wavelength 532nm (indicated by a horizontal grey line) which is used for our study. Though the absorption is not maximum at 73° (indicated by a vertical white line) for 532nm, still the value is quite high and sufficient for causing assembly of nanoparticles.
Calculations are based on solving Fresnel's equation for transverse magnetic (TM) waves in Kretschmann configuration. 40nm thick silver film was placed on N-BK7-glass-dove prism (RI= 1.519) and water (RI= 1.33) was the surrounding environment.

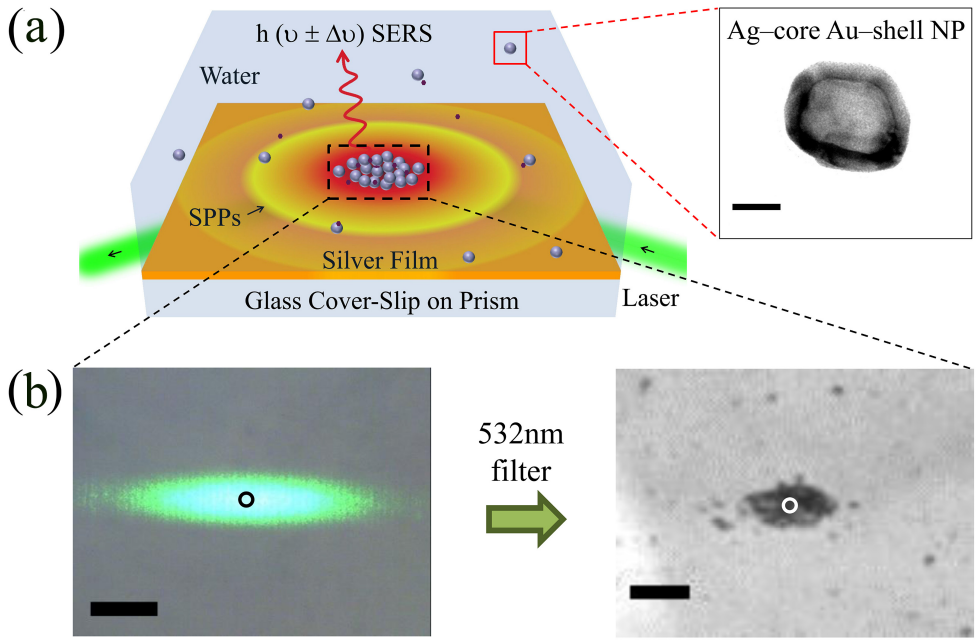

Figure 4.3: (a) Schematic illustration of the simultaneous plasmonic assembly of nanoparticles and SERS. Black arrows indicate the direction of 532nm laser (green beam) used for SPP excitation of the metal film deposited over glass coverslip. Grey spheres are the metal nanoparticles dispersed in the water medium and red dots indicate the SERS-active molecules. Inset on the right shows the TEM image of Ag@Au bimetallic nanoparticle used in this experiment. Scale bar is 20nm (b) On the left is an unfiltered optical bright-field image of 532nm elliptical excitation on the metal film; the right side image shows the plasmon-assisted assembly of nanoparticles in the excitation region (532nm light was rejected using filter). The open circles in (b) indicate the area from which SERS signals were collected. Scale bar is 80μm.

Upon introducing bimetallic core-shell nanoparticles solution (80μL) on to the Ag surface, the nanoparticles slowly (within 15min) assembled at the location of the elliptical spot. One such assembly of nanoparticles is shown in figure 4.3b by filtering the incident laser beam. The open circle shown in figure 4.3b(right) was the location from where the SERS signals were captured.

4.3.2 Choice of the metal films and nanoparticles

Trapping of plasmonic nanoparticles on metal film is extremely sensitive to three parameters: surface plasmon (SP) resonance of the nanoparticles, SP resonance of the film and excitation wavelength. In figure 4.4 the surface plasmon resonances (SPR) of various metal films and nanoparticles are plotted. We found that if the resonance

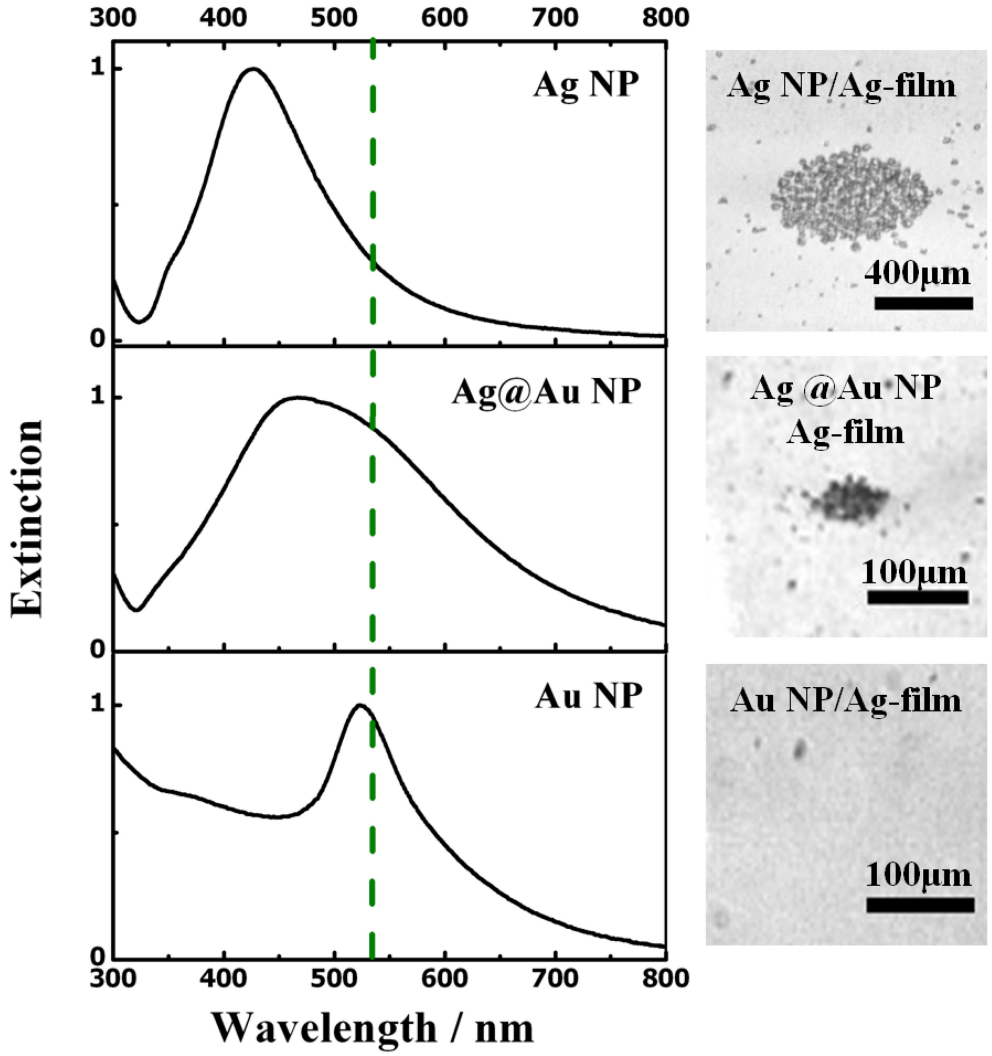

Figure 4.4: Comparison of trap sizes of different nanoparticles: Silver nanoparticles having LSP resonance far from the excitation wavelength give rise to a larger trap size, whereas core-shell particles having LSP resonance partially overlapping with excitation wavelength results in moderate trap size. In contrast to this, gold nanoparticles won't get trapped since their LSP resonance overlaps with excitation wavelength

of nanoparticles has a large overlap with the excitation wavelength, as in case of Au nanoparticles at 532nm, then nanoparticles usually escape from the trap, and were not suitable for our experiments. Such propulsion of Au nanoparticles in SPP field has also been reported by various researchers[120–122]. As an alternative to Au nanoparticles, we used Ag-core Au-shell (Ag@Au) bimetallic nanoparticles. In the previous chapter (section 3.3.1) we have already discussed that Ag@Au nanoparticle architectures are excellent substrates for single-molecule SERS experiments at visible frequencies.

There are at least three advantages[105, 119] of using such nanoparticles: 1) they facilitate optical near-fields comparable to Ag nanoparticles and better than Au nanoparticles; 2) by varying the thickness of the gold shell, one can systematically tune the surface plasmon resonance from visible to infra-red wavelength; 3) since these particles have gold shell, they provide biocompatibility and stability compared to Ag nanoparticles. With this hindsight, we utilized the similar batch of Ag@Au nanoparticles solution that had a plasmon resonance at around 490nm (figure 4.4). This value was slightly off-resonance from the 532nm excitation and hence suitable for both plasmonic assembly and SMSERS experiments.

Next we looked at the SPR of gold and silver thin film-water interface which was calculated solving Fresnel's equation and plotted in figure 4.5. We observed that the SPR absorption value for gold thin film at 532nm wavelength is slightly higher than that of silver film. And this has a clear impact on the assembly process which we shall discuss later (4.3.3, figure 4.7).

4.3.3 Assembly of Ag@Au nanoparticles in plasmofluidic field

Figure 4.6a shows the time series images of the assembled Ag@Au nanoparticles on a metal film in presence of 532nm p-polarized evanescent-wave excitation. We observed a gradual aggregation of nanoparticles spanning over a time period of 30 minutes. Between 06 minute and 16 minute, there was a steady increase in the number of nanoparticles assembled in the illuminated spot, but after 20 minute, we found that the number of nanoparticles in the illuminated region reached a saturation point, and thereafter the assembly reached a steady state. Figure 4.6b shows the assembly-growth kinetics of the nanoparticles in the dotted ellipse region. We captured the scattering intensity coming out of the elliptical region as a function of time, and the points in figure 4.6b represents the experimental data. The experimental growth kinetics fitted well with the least-square Boltzmann equation,

$$y = \frac{A_1 - A_2}{1 + e^{(t-t_0)/dt}} + A_2 \qquad \text{(Eq 4.1)}$$

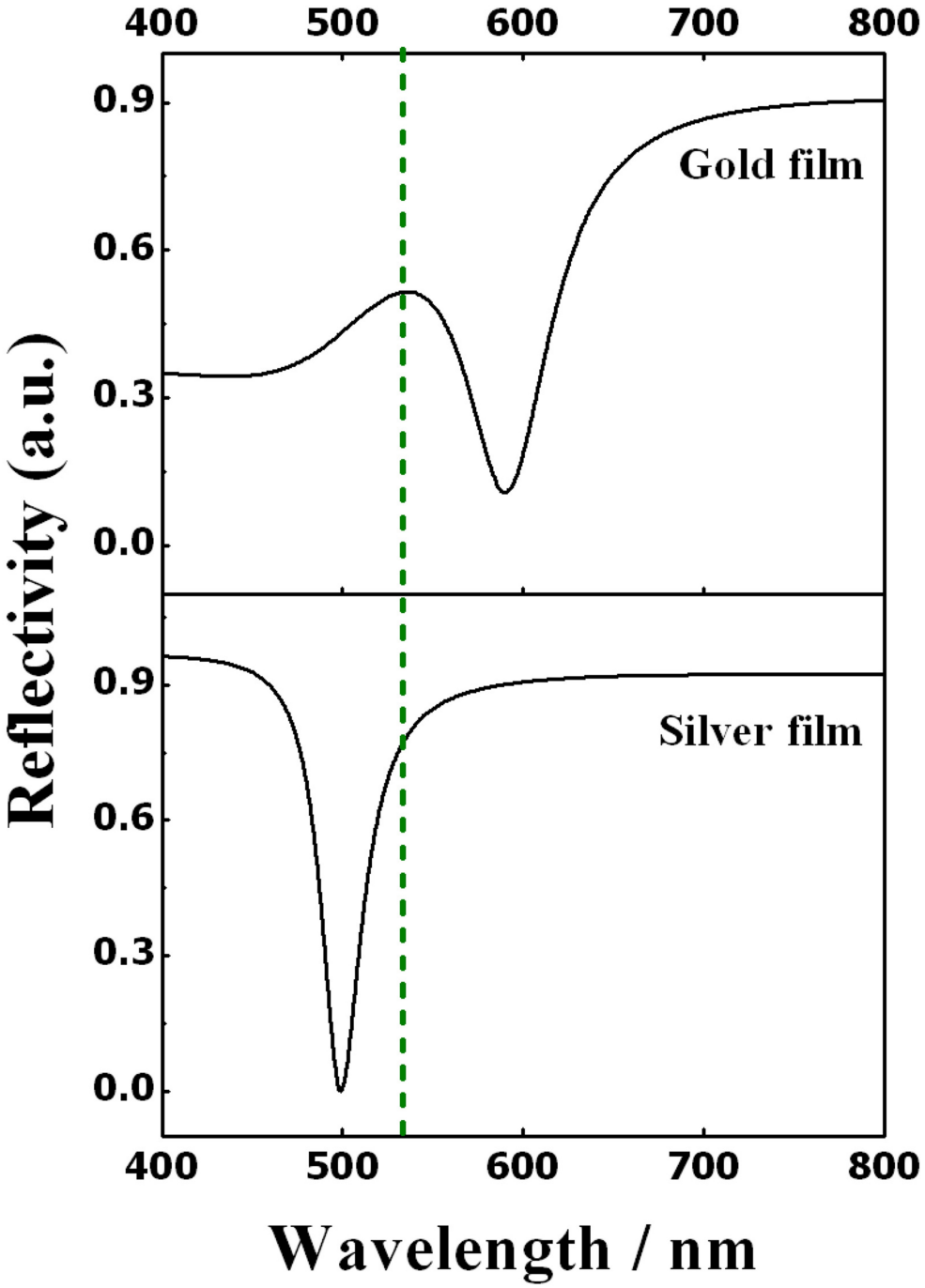

Figure 4.5: Wavelength dependent reflectivity spectra for 40nm gold and silver films, calculated solving Fresnel's equation for TM waves in Kretschmann configuration.

where, A_1, A_2 define the initial and final values of y (i.e. actually the grey scale intensity). t_0 is the value of $t(time)$ at $y = (A_1 + A_2)/2$, which can be extracted from the fit of the experimental data points. Rate of trapping was calculated by measuring the slope

at t_0 which is given by,

$$rate\ of\ trapping = \frac{A_2 - A_1}{4dt} \qquad \text{(Eq 4.2)}$$

To describe the assembly process we see that there are three different phases involved in this equation; 1) Lag Phase: Value of y is almost constant during initial time period (t). During this phase, the number of nanoparticles in the trap is almost zero. This is due to the fact that finite amount of time is needed for convection to start, which brings the nanoparticles into the laser illuminated region. 2) Exponential Growth Phase: Value of y grows exponentially with time t. During this phase, the number of nanoparticles within the illuminated region increases exponentially. 3) Saturation Phase: Value of y reaches a saturation point and doesn't change with time t. During this phase, the number of the nanoparticles remains almost constant.

The accumulation of nanoparticles in the illuminated region was mainly due to the combination of fluid convection and SPP forces experienced by the nanoparticles. Similar kind of plasmofluidic assembly of dielectric microspheres on a gold nano-film has been reported by Garces-Chavez et al.[123]. The excitation of SPP on the film creates a gradient of temperature just above the illuminated region. The temperature distribution in the surrounding water medium is governed by the following equation[124],

$$\rho c[\rho_t T(r,t) + \nabla \cdot (T(r,t)V(r,t))] - \kappa \nabla^2 T(r,t) = 0 \qquad \text{(Eq 4.3)}$$

where, $V(r,t)$ is the fluid velocity and $\nabla \cdot (TV)$ is the nonlinear convective term. κ, ρ, c are the thermal conductivity, mass density, and specific heat capacity of water at constant pressure, respectively. The temperature gradient creates convection in the fluid, and the nanoparticles move from the cooler region of the fluid into the hotter region, i.e. towards the illuminated spot. Furthermore, the same convection current will try to drive the nanoparticles away from the hotter region, but the gradient force of SPP holds them back from escaping out, thereby trapping them at the illuminated spot.

It is to be noted that the LSP resonance of plasmonic nanoparticles plays an important role in this assembly process. Trapping was feasible only when LSP resonance wavelength of nanoparticles was far from the excitation wavelength (532nm). Apart

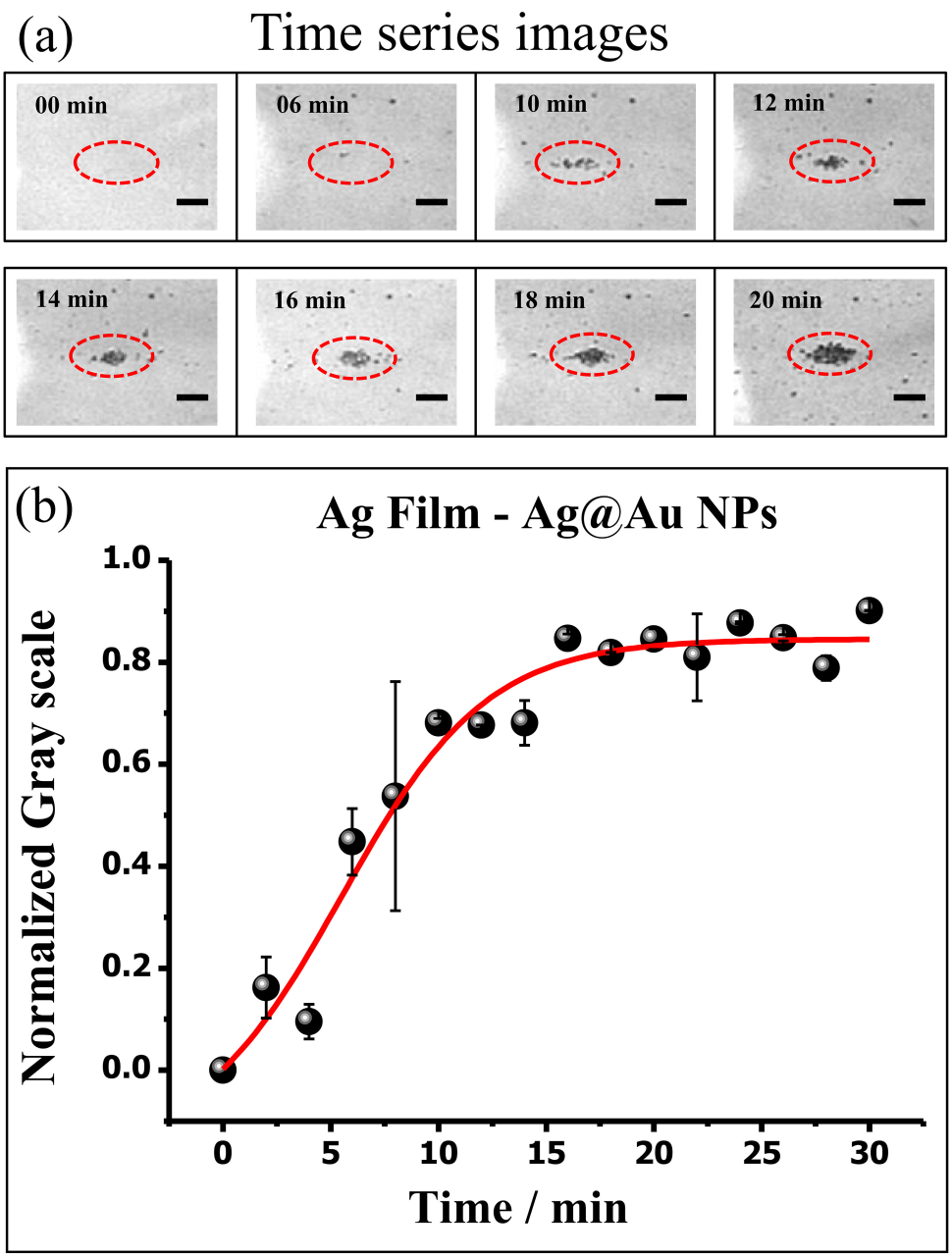

Figure 4.6: Plasmon-assisted assembly of Ag@Au nanoparticles at metal-fluid interface. (a) Time series images of gradual-accumulation of Ag@Au nanoparticles on silver-film in evanescent optical field indicated by dotted-ellipse in red. (b) Variation of particle density in the abovementioned field as a function of time, extracted from the images. Solid red-line represents the least-square Boltzmann fit to the experimental data. Error bars on the experimental data points represent the variation (standard deviation) in determining the grey scale values across the optical images obtained throughout the experiment.

from Ag@Au nanoparticles, we tested this hypothesis for Ag nanoparticles (LSPR =

$\backsim$ 420nm), and found excellent trapping capability. Interestingly, Ag nanoparticles assembled in the trap at a faster rate compared to Ag@Au nanoparticles (shown in figure 4.7). Not only has the SPR of the nanoparticles an active role in the assembly process but also the SPR of the film. From figure 4.7d, it is evident that the rate of the assembly for both the nanoparticles is higher at the gold film-water interface. The cause might be attributed to the higher value of absorbance of gold thin film at 532nm excitation, shown in figure 4.5.

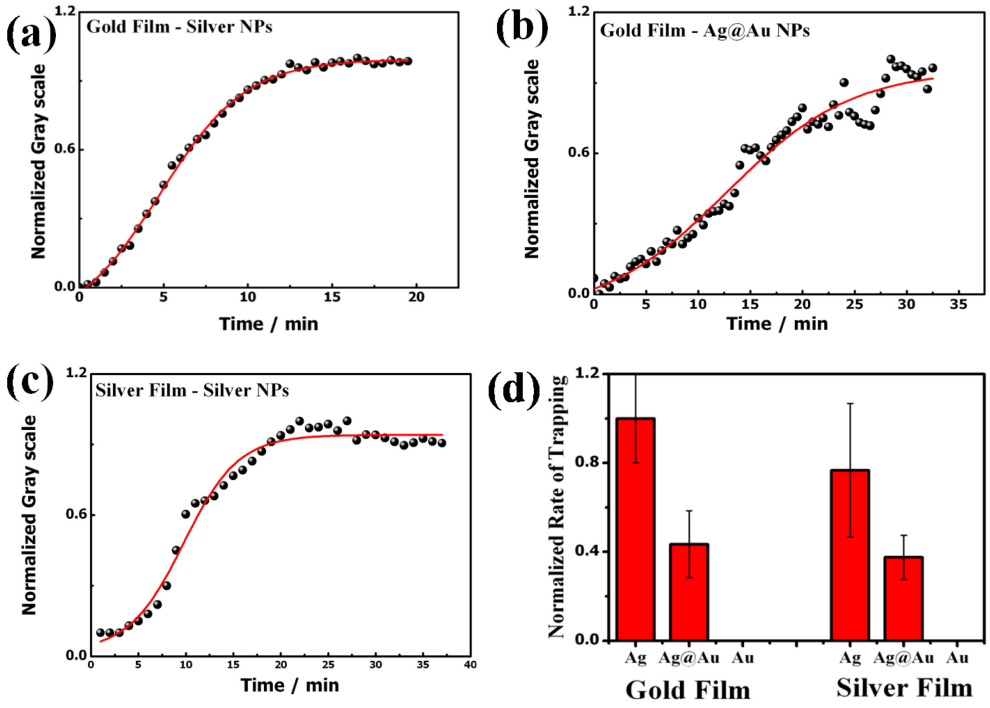

Figure 4.7: Comparison of trapping kinetics for different nanoparticles on different films. Variation of nanoparticle density in optical potential was monitored as function of time. Particle density was calculated by measuring the grey value from the optical images captured at different times. (a) Time dependent trapping of Ag nanoparticles on gold thin film; experimental data points (solid black spheres) have been fitted with Boltzmann curve (solid red line) to calculate the time required for trapping and rate of trapping. Similar measurements were done for (b) Ag@Au nanoparticles on Au film and (c) Ag nanoparticles on Ag film. We observed experimentally that Au nanoparticles were NOT assembled either on gold film or on silver film. (d) Graph comparing the rate of trapping for different nanoparticles on different films. Error bars represent the fluctuations in the trapping rate throughout the experiment.

Furthermore, we tested the reversibility of the nanoparticle assembly, by switching-off the evanescent-field excitation and later switching it on again after a few minutes. Figure 4.8 shows the optical images of two such cycles of reversible-assembly

of Ag@Au nanoparticles where the excitation fields were alternately switched on and off. We tested this process over multiple cycles and we found excellent consistency in terms of reversible assembly of nanoparticles at the illuminated location.

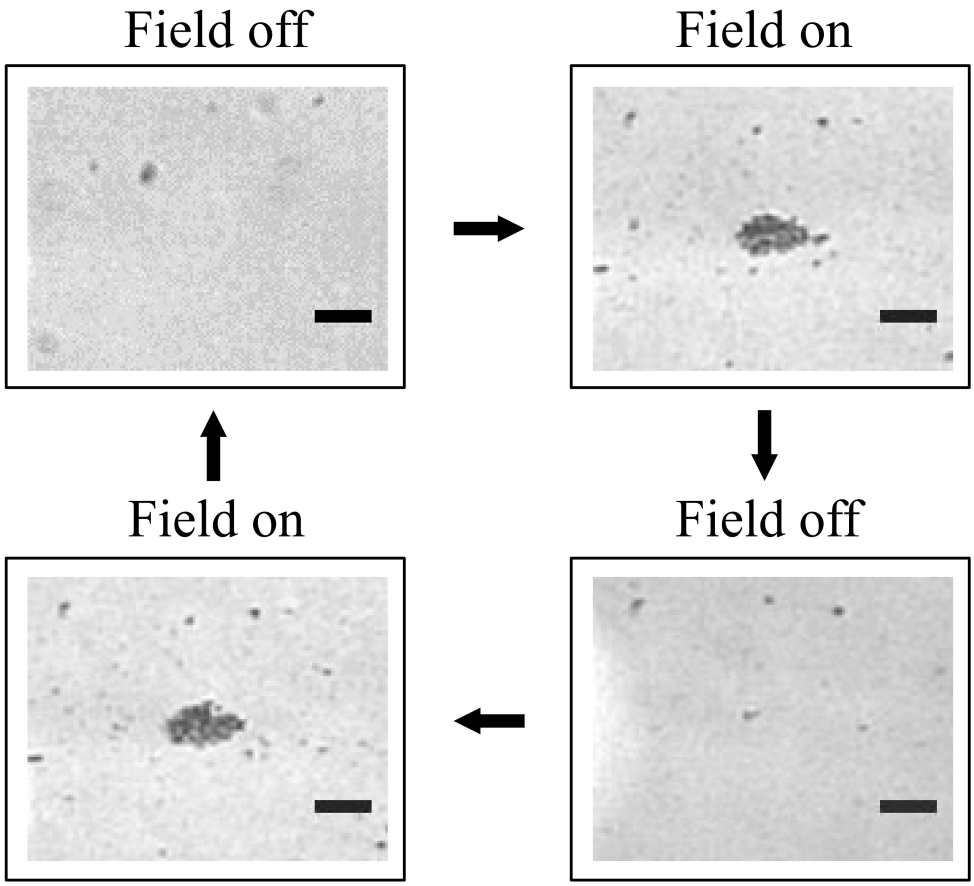

Figure 4.8: Optical bright-field images showing capability to repeat the assembly and release of nanoparticles in the presence and absence of plasmonic field at metal-fluid interface. Scale bar is 80μm for all figures.

4.3.4 Single-molecule SERS from plasmon-assisted assembly of Ag@Au nanoparticles

Since many nanoparticles are packed into an assembly on the metal surface, one would expect multiple plasmonic hot-spots in this confinement. Such hot-spots are ideal for SERS experiments[83, 90]. Furthermore, the same optical excitation which is assembling these nanoparticles should also be able to excite SERS signatures of the molecules

in the hot-spot. Can these hot-spots be sensitive enough to detect single molecule Raman signatures?

To answer this question, we employ bi-analyte single molecule SERS method developed by Etchegoin and Ru[53, 94] (discussed in chapter 2). This technique is based on spectroscopic contrast between two different kinds of SERS-active molecules, and importantly, does not rely on the ratio of number of molecules to the nanoparticles used in the experiments. From a large data set of SERS experiment, reliable single molecule signatures can be extracted by rigorous statistical analysis based on modified principal component analysis (MPCA)[94]. The two analytes used for our experiments were Nile blue (NB) and Rhodamine 6G (R6G) at 5nM concentration. For SMSERS experiments, we choose 592cm^{-1} and 615cm^{-1} Raman modes of NB and R6G, respectively.

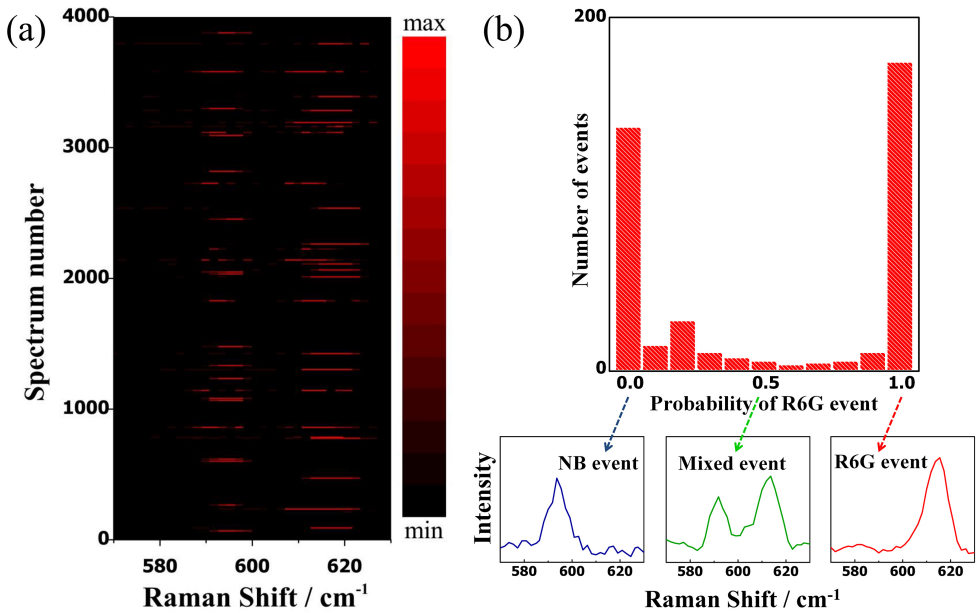

Figure 4.9: Single-molecule SERS from plasmon-assisted assembly of Ag@Au nanoparticles on Ag film. (a) Bi-analyte (Nile blue (NB) and Rhodamin6G (R6G)) SERS time-series spectra recorded from the open circle region shown in figure 4.3b. The concentration of both the analytes was 5nM. For modified principal component analysis (MPCA), 592cm^{-1} mode of NB and 615cm^{-1} mode of R6G were considered. 4000 spectra (out of 7000) have been displayed to show spectral fluctuation of single molecules in plasmonic field. Signal acquisition time was 0.1 second. All the data were collected using 532nm evanescent excitation wavelength (20mW power before entering the prism) (b) Single-molecule probability histogram derived from MPCA. Maximum event at 1 and 0 of abscissa confirms single molecule SERS signal from R6G and NB, respectively. The insets show spectral signatures for three different probabilities.

Figure 4.9a shows time evolution of bi-analyte SMSERS signal captured from the plasmofluidic trap of core-shell nanoparticles (see the open circle in figure 4.3b). The total number of spectra collected was 7000, the acquisition time for each spectrum was 0.1s, and the dwell time between consecutive accumulations was 1s. We further processed this data using MPCA to find the principal eigenvalues of the signals generated. All the details of the MPCA analysis have been discussed in chapter 2 section 2.2.2. The result of the MPCA analysis is shown in figure 4.9b, where the probability of single molecule signature is plotted in the form of a probability histogram, and accompanying them are the relevant bi-analyte spectra for three different probabilities of single molecule events (0 corresponds to single NB event, 0.5 for mixed event and 1 for single R6G event; the probability for detection of R6G single molecule is slightly greater than NB because electronic resonance of R6G is closer to 532nm excitation). The histogram clearly indicates a large probability of single R6G and single NB molecules' spectral signatures arising from the plasmofluidic assembly of nanoparticles. *This data is the central result of this work.*

As we have introduced a new kind of microscopy technique to SMSERS, we have further confirmed it with a concentration dependent study. For SMSERS experiments when we shift to higher concentration of analytes, actually we enter into the many molecule SERS regime; in such a case the probability histogram turns into a Gaussian distribution[47, 94]. In contrast, as we go to lower analyte concentrations beyond single molecule regime then only the probability of signals goes down; the nature of the distribution does not change much. Figure 4.10 shows the concentration dependent SMSERS experiments. Here we have shown the many-molecule SERS probability distribution with 200nm analyte concentration (figure 4.10a). The lower concentration SERS studies are done using only R6G dye. We performed time-series SERS experiments at three different concentrations of R6G: 50nM, 10pM and 1fM, as in the figure 4.10 (b), (c) and (d). This lower-concentration SERS study in another sense is a test bed of the detection limits of our method. We observed that if we go down to the lower concentrations, the SERS intensity fluctuates and importantly, the occurrence of the signals decreases drastically.

However, we emphasize that the single molecule SERS excitation is arising from

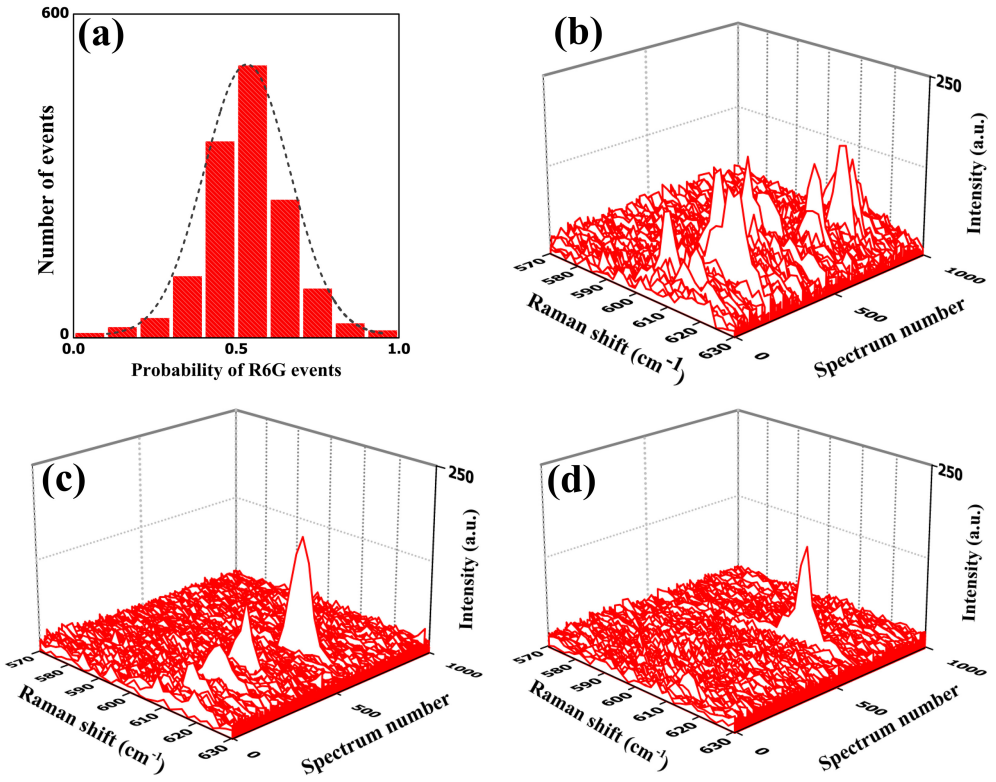

Figure 4.10: Concentration dependent study: (a) Probability histogram of the signals acquired from higher bi-analyte dye concentration (200nM). In this case, events with probability around 0.5 were more likely to occur which means at higher dye-concentration, events due to both NB and R6G signals are dominant. Here we used 200nM concentration for both the dyes, which implies that $\backsim$ 960 molecules of each analyte reside per one nanoparticle. 1419 events were extracted from collected total 3000 signals using MPCA. The above histogram can be contrasted to the extreme probability distribution in figure 4.9b of the main manuscript. (b), (c) and (d) are time series surface-enhanced resonance Raman spectra (SERRS) of R6G at three different concentrations. (b) Signal fluctuation at 50nM R6G concentration (i.e. $\backsim$ 240 molecules of each dye per one nanoparticle). Here most of the events give the dye signal. (c) At 10pM dye concentration (i.e. one molecule of each dye per $\backsim$ 200 nanoparticles) number of signals decreased as the number ratio went down by order of three. (d) The signal fluctuation at ultra-low concentration (10fM) of the analyte. Here the number ratio is like, one molecule of each dye per $\backsim 2 \times 10^5$ nanoparticles, still we could detect the molecule but with a lower probability.

the same source which is assisting us in assembling the nanoparticles. To the best of our knowledge, this is the first report where both plasmofluidic assembly and single-molecule SERS has been concomitantly achieved using a single evanescent-wave excitation. Thus our method not only creates multiple plasmonic hot-spots in a nanoparticle assembly but also probes the single molecule spectral signatures simultaneously.

In our experimental configuration, there are two kinds of plasmonic fields: one is the

P-SPP field created by the metal film and the other is the L-SPP of the nanoparticles. Importantly, the P-SPP of the film can couple to the L-SPP of the nanoparticles[125–132]. This combination of the P-SPP and L-SPP can facilitate large electric fields thereby creating plasmonic hot-spots at two locations: junction between film and nanoparticles, and the junction between individual nanoparticles. Furthermore, nanoparticles assemble in both horizontal and vertical direction, leading to multiple hot-spots in the illuminated region of metal-fluid interface. We further corroborated this hypothesis with 3dimensional-finite different time domain (3D-FDTD) calculations (figure 4.11), which indicated near-field electromagnetic enhancement to arise due to film-particle coupling and particle-particle coupling. The FDTD calculations were done using commercially available software package (Lumerical Solutions, Inc.). Figure 4.11a shows the simulation configuration for FDTD calculations. The metal nanosphere was made of Ag@Au (45nm silver-core and 5nm gold-shell)bimetallic nanoparticle and kept 2nm above on the 40nm thick silver metal film. The dielectric constant of silver and gold was taken from Johnson and Christy[133]. A p-polarized 532nm Gaussian-profile laser beam was incident from a far-field regime through N-BK7 glass medium (RI$=1.519$) at an angle of $^{*}76.70^{\circ}$ to create an evanescent-field excitation geometry. The fluidic environment of the Ag@Au nanoparticle was kept as water medium (RI$=1.33$) to mimic the experimental set-up. The electric field distribution in the plane of particle and film was calculated with the mesh size of $(0.5 \times 0.5 \times 0.5)$ nm^3. $52,500$ iteration-time-steps were used to ensure the stability of the calculated solutions. We can see very high electromagnetic field at the junction of the nanoparticle-nanoparticle junction as well as film-particle junction. Such multiple hot-spots at metal-fluid interface can facilitate large scale enhancement, and our experimental result of single molecule spectroscopic detection is one such important consequence due to the near-field coupling between the molecules and nanoparticles.

*For FDTD simulations, the angle of incidence of excitation beam was mistakenly defined as 76.70° instead of 72.70°. Since at 72.70° incidence angle, the SPR absorbance of Ag film (40nm) is very high (greater than that of 76.70°) at 532nm excitation beam (shown in figure 4.2), the simulated electromagnetic field intensity in such hot-spots can be larger than the reported one.

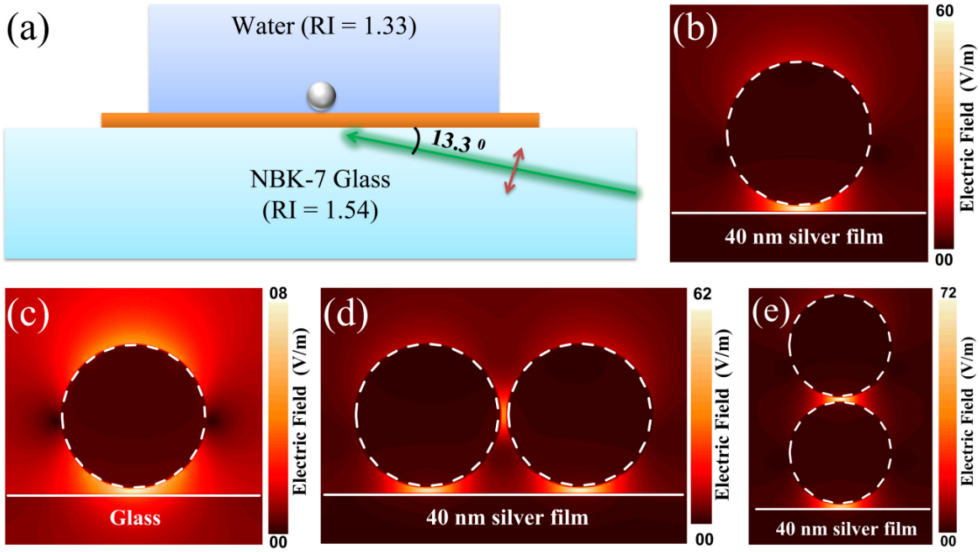

Figure 4.11: Finite domain time difference (FDTD) calculations: (a) 3D-FDTD simulation configuration: Green line is a p-polarized 532nm Gaussian profile laser incident from a far-field regime through N-BK7 glass medium (RI= 1.519) at an angle of incidence, *76.70°. Grey coloured sphere is a silver-core gold-shell nanoparticle in water medium (RI= 1.33) placed 2nm above the 40nm thick silver metal (orange slab). (b) Electric field distribution in the plane containing core-shell nanoparticle and silver film; film-particle junction shows maximum electric field concentration of 60V/m; (c) Electric field distribution for a core-shell particle placed 2nm above on the glass film. (d) Electric field map for two nanoparticles clustered horizontally on the metal film with 2nm gap between the particles. Film-particle junction has higher field electric field concentration compared to particle-particle junction. (e) Electric field distribution for two core-shell nanoparticles clustered vertically on the metal film with 2nm gap between the particles; film-particle gap was also 2nm. Particle-particle junction has higher field concentration compared to particle-film junction.

4.3.5 Plasmon-assisted manipulation of Ag@Au nanoparticles assembly

Having shown the capability to perform single-molecule SERS at metal-fluid interface, we asked whether we can systematically manipulate the trapped assembly of nanoparticles, such that they can be utilized as optically addressable, single-molecule SERS substrate in a fluid. To answer this, we probed the effect of moving the elliptical excitation beam on the plasmonic nanoparticle assembly. Figure 4.12 shows the optical images (time series) of plasmonic nanoparticles transport at metal-fluid interface. The different locations - P, Q and R in figure 4.12 indicate the three parking points of elliptical excitation beam. We first started with a plasmonic assembly at P. Next we moved

the excitation beam to the location Q, and after a few seconds we observed gradual migration of the plasmonic nanoparticles into new location, Q. About 40 seconds later, we changed the location of optical excitation from Q to R, and within a few seconds, the nanoparticle assembly followed the excitation beam. This experiment revealed two important aspects of the trap: a) capability to accurately manipulate a large assembly of nanoparticles in fluid by plasmon-assisted excitation without structuring the metal surface, and b) the robustness to overcome the Brownian motion of nanoparticles during the movement of the assembly. These advantages can be further harnessed in plasmon-assisted micro- and nano-fluidics with an added capability of single molecule detection sensitivity.

It is to be noted that our methodology is versatile and can be applied to different combinations of metal films and plasmonic nanoparticles. Table 4.1 compares a variety of such combinations for 532nm excitation. Parameters such as nanoparticle assembly time, assembly-size and the SERS signal retrieved from such assemblies are compared. Specifically for SMSERS studies, we found Ag@Au nanoparticles and Ag nanoparticles on Ag film to be suitable. Also, other combinations of film and particles can be harnessed for conventional SERS studies.

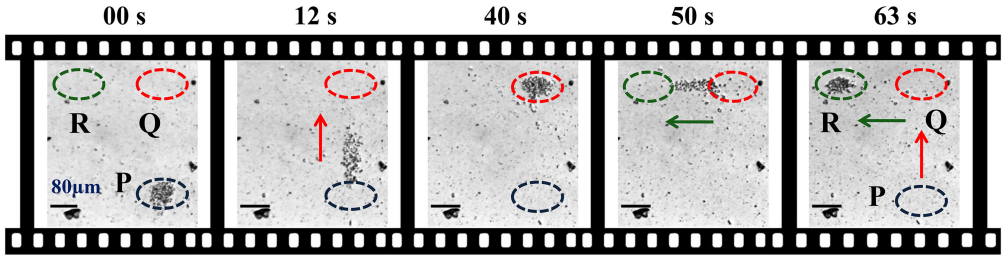

Figure 4.12: Plasmon-assisted manipulation of Ag@Au nanoparticle assembly at metal-fluid interface. Time series images showing transportation of nanoparticle assembly from initially trapped area P to final area R via point Q. The manipulation involves a right-angled turn which was achieved by careful movement of evanescent excitation beam. The assembly of nanoparticles was accurately transported over a distance of 300μm within few seconds. Note that the manipulation was achieved on an unstructured metal-fluid interface. Scale bar is 80μm.

Table 4.1: Comparison of nanoparticles-assembly and SERS signal intensity between 6 different combinations of metal film and plasmonic nanoparticles tested for 532nm excitation.

532nm evanescent field Excitation	**1 Ag-film +Ag NP**	**2 Ag-film+ Ag@Au NP**	**3 Ag-film +Au NP**	**4 Au-film +Ag NP**	**5 Au-film + Ag@Au NP**	**6 Au-film +Au NP**
Assembly time	Fast (10min)	Moderate (17min)	No assembly	Fastest (7min)	Moderate (15min)	No assembly
Assembly size	Large (400μm)	Moderate (60μm)	No assembly	Large (500μm)	Moderate (70μm	No assembly
SERS signal (1s acquisition)	Intense	Intense (5000counts)	Lowest	Moderate	Moderate	No signal

NP, nanoparticles; Ag@Au NP, Silver-core gold-shell bimetallic NP; SERS, surface-enhanced Raman scattering.

4.3.6 Towards large-area dynamic assembly of nanoparticles at metal-fluid interface

Can we utilize this method in dynamic lithography of dispersed nanoparticles at metal-fluid interface, such that they can be temporarily assembled in a specific geometry and further re-dispersed in the fluid? To answer this question we performed experiments with Ag nanoparticles on Au film (combination 4 in Table 4.1) with a dual 532nm evanescent-wave excitation in counter-propagating geometry. Figure 4.13a shows the optical schematic of dual-excitation trap. Two beams were introduced into the Dove prism from opposite ends. The optical image of the two elliptical excitations in the same line is shown in figure 4.13b, where the distance between the centres of two beams were approximately 340μm. These excitations further created assemblies of Ag nanoparticles at metal-fluid interface. Interestingly, when these two assemblies were in close proximity, we found interaction between assemblies leading to a linear chain of nanoparticles between them.

Figure 4.13c shows optical image (after rejecting the laser light) of the two plasmonic assemblies, with a thin line of Ag nanoparticles between them. We also observed similar kind of Ag nanoparticle linear-chains when two assemblies were created in an parallel geometry (see figure 4.13d). The resulting nanoparticle assembly is shown in figure 4.13e. Since the assemblies are now closer (compared to the case shown in figure 4.13c), the nanoparticle bridge formed is thicker in size. It is to be noted that all

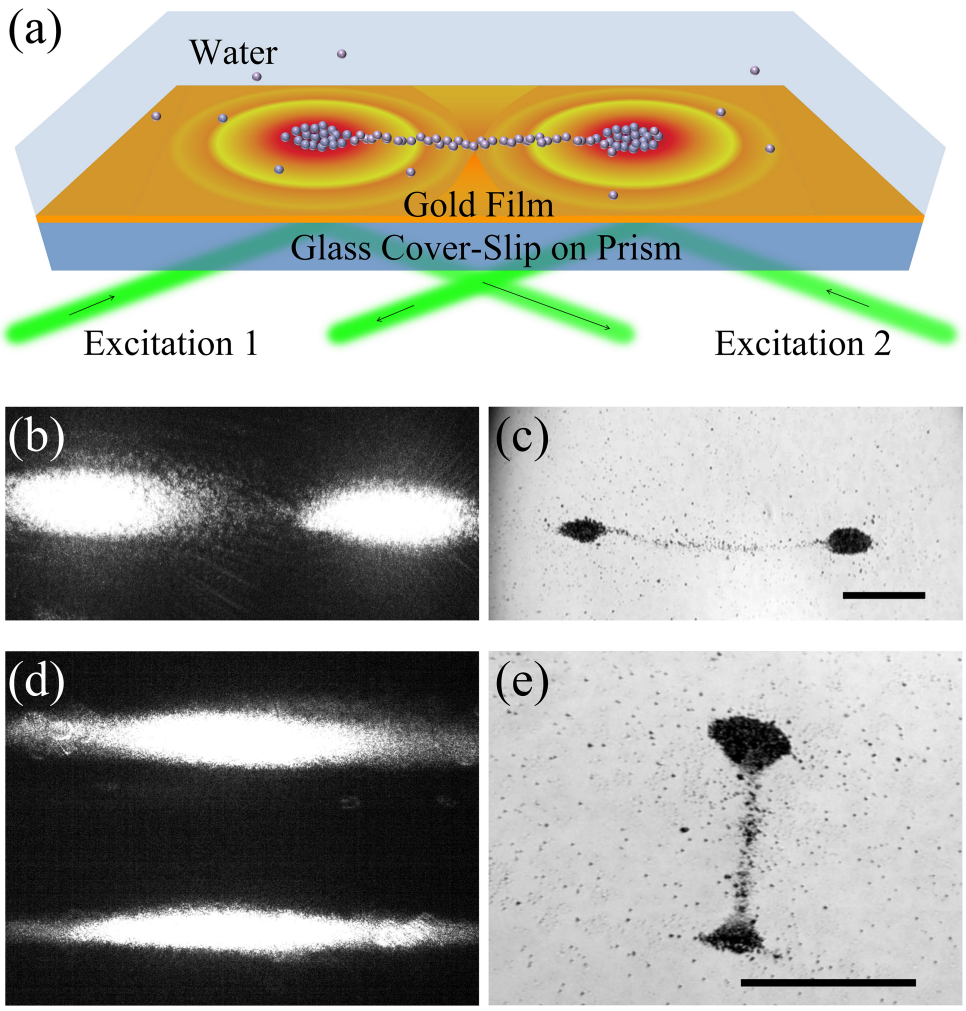

Figure 4.13: Interaction between dynamic assemblies of plasmonic nanoparticles at metal-fluid interface. (a) Schematic representation of dual assembly of Ag nanoparticles on Au film coupled to a prism: green lines are the two laser beams of 532nm introduced at two opposite ends of the prism. Black arrows indicate the direction of the laser beams. Optical images of dual laser excitation in (b) collinear geometry with opposite k-vectors and (d) parallel geometries with opposite k-vectors. (c) and (e) are optical images (532nm-rejected) of Ag nanoparticles assembly due to excitation in shown in (b) and (d), respectively. A thin line of nanoparticles bridging the two assemblies are evident. Note that all these assemblies are at metal-fluid interface, and hence can be further manipulated to achieve dynamic lithography. Scale bar= 100μm for both (c) and (e).

this manipulation discussed herein is at the metal-fluid interface. If the excitation beam was switched-off, the entire nanoparticle assembly re-dispersed into the solution. This method is reversible over multiple cycles, and can be an excellent preamble to create dynamic assembly of nanoparticles at metal-fluid interface, and can be further harnessed for large-area, dynamic, optical lithography of nanoscale objects.

4.4 Summary

In this chapter, we have discussed that how an unstructured metal film and plasmonic nanoparticles can be utilized to form a sensitive molecular detection platform using evanescent-wave microscopy. To practise such experiments, the sample preparation is easy to reproduce, and can be readily integrated with any microfluidic device. There are situations in microfluidics where one needs to control mixing of molecules and/or nanoparticles for a brief period of time. By using our method, one can assemble nanoparticles for a short instance of time, spectrally probe a mixing reaction, and release them back into the solution. This capability to trap, probe and release nanoparticles in a controlled way, especially using optical means, will have implications in driving optofluidic chemical and biochemical reactors. It is also worth mentioning that our methodology is not restricted to metal nanoparticles alone. One can trap two different kinds of samples, such as biological cells and nanoparticles in separate traps, and bring them together in close proximity to obtain a mixture. Since assembly and probing is done through optical means, one can also utilize the same optical fields to catalyse photochemical reactions.

To summarize, we have discussed how plasmon-assisted assembly and single-molecule SERS can be achieved with a single evanescent-wave excitation on an unstructured metal film. Such dual-function of plasmons at metal-fluid interface can have relevance in trace detection of molecules at interface without having to structure the metal surface. Furthermore, on the same platform, we have shown how nanoparticles can be reversibly assembled and manipulated with ease. This is also a unique method to prepare and optically manipulate SERS substrates at metal-fluid interface that is sensitive enough to detect single-molecule spectroscopic signatures. Interestingly, when we used two excitation beams in our experiments, we could create interacting nanoparticle assemblies. The cross-talk between the assemblies led to the formation of a nanoparticle bridge between the optical potentials paving a new way to assemble nanostructure at metal-fluid interface. We envisage that interacting optical potential can be further harnessed in large-area dynamic lithography of nanoparticles at metal-fluid interface. Such capability will of course find tremendous use in micro- and nano-plasmofluidic applications,

where plasmonic fields can drive, trap and probe nanoscale objects.

Chapter 5

Towards plasmofluidic dynamic lithography

Chapter 5 is an adaptation of the research article, '*Faraday Discussions, 186, 95-106 (2016).*' The article Shows that the evanescent-wave based plasmofluidic assembly technique can lead to a preamble of reconfigurable dynamic lithography of plasmonic nanostructures at metal fluid interface.

5.1 Introduction

Manipulation and reversible assembly of large number of nanoparticles in a fluid is of relevance in various aspects of microfluidic science and technology[134–140]. The assembly of nanoparticles, especially of noble metals, has also derived attention in self-assembled plasmonic metamaterials[141–147] that can control various parameters of light at sub-wavelength scales. An inherent challenge to overcome while handling nanoparticles in liquid is the Brownian motion. Various possible methods have been developed to overcome this hindrance, of which optical trapping has attracted significant attention[148–154]. Although laser-based conventional optical trapping has been very successful in trapping and manipulating sub-micron scale objects, it still needs powerful lasers to create gradient and scattering forces at a tightly focused location[155–158]. This requirement of large optical power is detrimental to trapping of soft nanomaterials, as they can severely damage the structure of the trapped object. An alternative method of trapping sub-micron scale objects with low power laser excitation is to utilize the surface plasmon polariton field generated through evanescent wave at

metal-dielectric interface[123, 159–164]. Surface plasmon polaritons, the collective oscillation of free electrons and light at metal-dielectric interface, can localize optical fields to sub-wavelength scale and propagate optical signals beyond diffraction limit[18, 72, 165–168]. This capability to localize and propagate light can be further harnessed to trap and manipulate large assemblies of nanoparticles, including resonant plasmonic nanoparticles[162, 169, 170], at metal-fluid interface. Such trapping methods which use plasmonic field in fluidic environments are generally called plasmofluidic traps[139], and can be harnessed to trap and manipulate nano and microscale objects in the presence of Brownian motions.

In the previous chapter, we discussed a method[171] to trap and manipulate plasmonic nanoparticles assembly at an unstructured metal-fluid interface. We showed that, by using single evanescent optical excitation, our trapping mechanism could not only manipulate nanostructures in a fluid, but also detect single-molecule Raman scattering signatures in the created trap. The same method was also shown to work with dual evanescent wave excitation, which was harnessed to show interaction between dynamic assemblies of nanoparticles. This method, in an essence, has expanded the capability of dynamic trapping and single-molecule assisted probing of nanoparticle assemblies using surface plasmon polaritons. Furthermore, there are still many interesting questions regarding our method that are to be addressed such as: a) what will be the effect of multiple evanescent plasmon excitation on dynamic assembly of plasmonic nanoparticles in fluids? Answering this question will lead to understanding of how nanoparticle assemblies interact with each other at metal-fluid interface, especially when the interaction is mediated by the near-field interference of surface plasmon polaritons. b) Can we extrapolate our method to trap anisotropic geometries such as plasmonic nanowires? The answer to this question will open a new possibility of manipulating and arranging nanowires in liquids, which can be further harnessed for nano-optical and nano-optoelectronic circuitry in liquids. In this chapter, we discuss the experiments that address the above-mentioned questions for some special cases. We show a) how three and four evanescent-optical excitations can lead to interesting assemblies of plasmonic nanoparticles at metal-fluid interface; and b) how plasmonic Ag nanowires can be trapped and aligned at unstructured and structured metal-fluid interface.

5.2 Experimental Section

5.2.1 Materials preparation

Preparation of unstructured and structured gold thin film:

The unstructured gold thin films were prepared by direct current (DC) plasma sputtering technique, already discussed in our previous chapter 4.2.1. The thickness of the film was (50 ± 5)nm for this work.

The structured gold thin films were produced by photolithography technique and followed by Au deposition through plasma sputtering. First, a glass substrate was thoroughly cleaned and heated at $80 - 100°$C. Then, it was coated with the photo-resist at 4000rpm for 3min. The photo-resist coated glass substrate was baked at $\sim 85°$C. Thereafter, the patterns were written using 405nm laser line. After developing the glass substrate, 50nm Au was deposited on to it by DC sputtering. Finally this was washed with acetone to remove the remaining photoresist to make ready for the assembly experiment. The geometry of the structured film was like periodic strips; each strip was of length-50μm, width-2μm, thickness-$50(\pm 5)$nm and the gap between two consecutive strips was 2μm.

Synthesis of Silver nanoparticles:

In this work we used aqueous phase silver colloidal nanoparticles, synthesized by citrate reduced method[102] discussed earlier (chapter 3, section 3.2.1).

Synthesis of Silver nanowires:

The silver nanowires were synthesized by polyol process[165, 172]. 3mL of each, 0.1M $AgNO_3$ solution and 0.6M polyvinylpyrrolidone (PVP, MW, 55000) solution in ethylene glycol (EG) were mixed together in room temperature. This mixture was then injected drop wise to 5mL preheated EG at $\sim 160°$C and kept it for 1hr. The nanowires were then washed in acetone and water. The final Ag nanowire suspension was made in water.

5.2.2 Finite difference time domain(FDTD) simulations:

The simulation set up consisted of a 50nm thin gold film placed on a glass slab and the medium above the metal film was modeled with refractive index of 1.34 (water). A vertical dipole (polarization perpendicular to the plane of metal film) of 532nm was placed at the interface of metal and glass for the excitation of SPPs on metal film. Two-dimensional (2D) frequency domain power monitor was set at the metal-water interface to record the near-field image. Perfectly matched layer (PML) boundary conditions were applied in the far-field domain to avoid reflections from the boundaries. For multiple excitations, equivalent numbers of vertical dipoles were placed at the appropriate (xy-plane) position at the metal-glass interface.

To model the structured film (metallic strip) experiment, simulations were done for a vertical dipole excitation at the center of a single strip (dimensions matching with experimental parameters) with periodic boundary condition in x-direction and PML on the other two axes. The difference in the excitation methods between the experiments and simulation was justified since only the z-component of electric-field (p-polarization) contributes to the SPP excitation.

5.3 Results and Discussion

5.3.1 Multiple-spot-excited plasmofluidic assembly of silver nanoparticles

We first addressed the issue of how to excite multiple evanescent-waves at metal-fluid interface to assemble metal nanoparticles. In order to do so we chose to excite multiple surface plasmon polariton waves on metal film in Kretschmann geometry. Choice of nanoparticles, metal film and wavelength of excitation are crucial, so we utilized the optimized parameters from our previous study[171].

The plasmon excitation set-up (figure 5.1 and 5.2a) consists of 532nm continuous-wave frequency-doubled Nd:YAG laser (maximum power up to 200mW) coupled with a Dove-prism (N-BK7, Refractive index, 1.519). A glass coverslip coated with gold thin film (50 ± 5nm) was used as the substrate. The p-polarized light was used at an

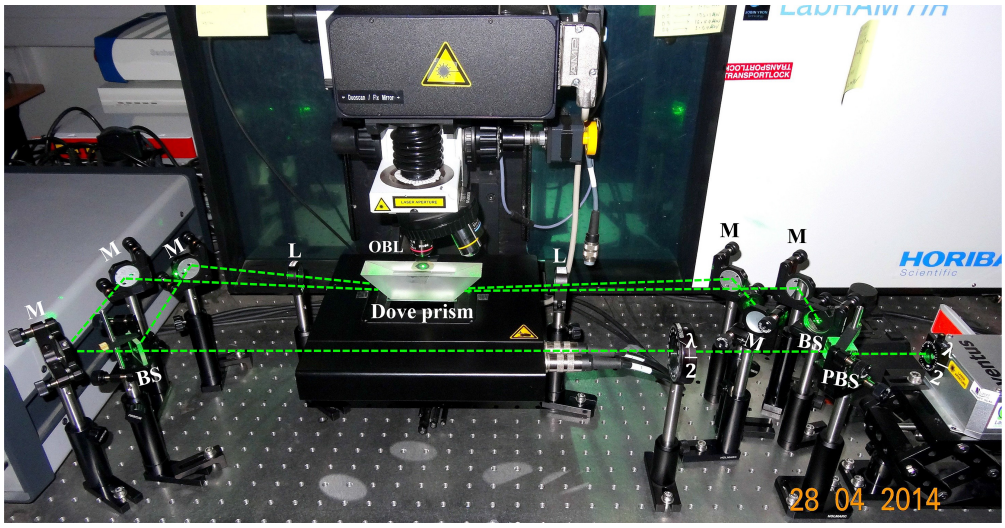

Figure 5.1: Photograph of the multi-spot-excitation evanescent field microscopy

incidence angle of $72.7°$ for the assembly process. The multiple beams with equal power were created by using $50 - 50$ beam splitters (BS), polarizing beam-splitters (PBS) and half-wave plates ($\lambda/2$). Four weakly focusing lenses of same focal length were used to focus the light. In such a geometry, the power density at the excitation spot arises as approximately 100 W/cm^2 which is very low compared to the conventional objective lens based excitation ($\sim$ 10^6 W/cm^2). To capture the real time assembly process, objective lenses (OBL) with magnification $\times 4$ and $\times 60$ were used. To capture bright field images a white light source was combined with the imaging system and a high pass filter (HPF) was introduced before the CCD camera to block the excitation beam. In figure 5.2b the dark-field image of the triple-spot-excited gold thin film is shown.

Onto this film 200μL Ag colloidal solution was drop-casted and the assembly process was recorded in real time and analyzed through snap-shot images. Figure 5.2c is a bright-field snap shot of the assembly process taken after 12 minutes of excitation. We observed that the nanoparticles were assembled at the excitation spots as well as at the orthocenter where there was no direct optical-excitation. In our earlier study,[171] we elaborately explained the role of hydrodynamic and optical forces in the assembly of nanoparticles at the single excitation spot. Here, convoluted effect of multiple excitations resulted in the formation of nanoparticles-assembly at the orthocenter and

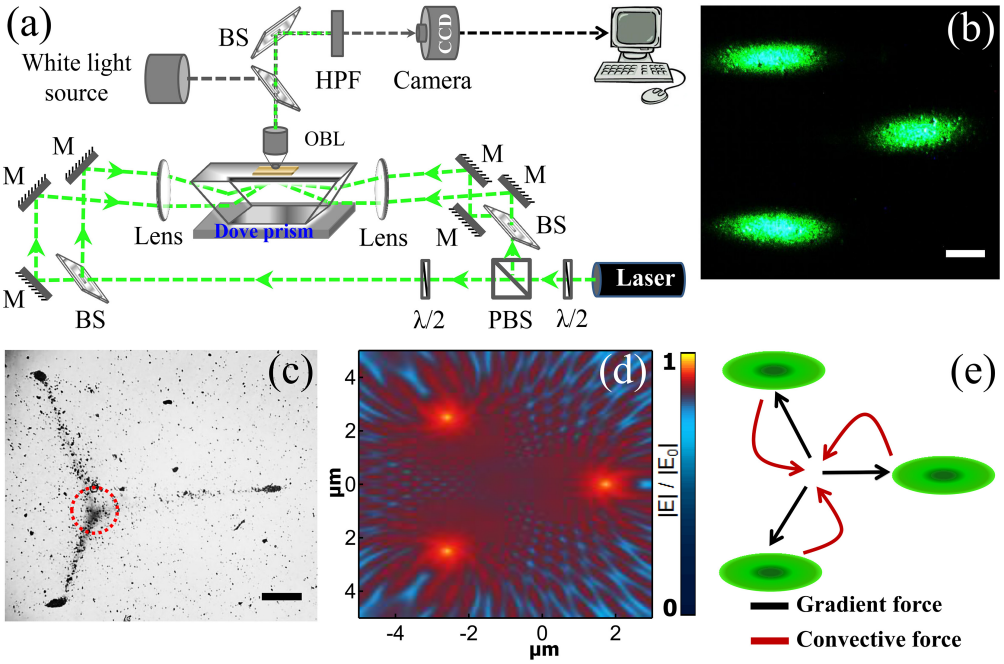

Figure 5.2: : (a) Schematic of the evanescent-wave multi-trap optical set-up used for plasmofluidic assembly of plasmonic nanoparticles. Acronyms: $\lambda/2$, half wave plate; PBS, polarizing beam splitter; BS, $50-50$ beam splitter; M, mirror; OBL, microscopic objective lens; HPF, high pass filter. (b) Optical dark-field image of the three, evanescently-excited 532nm laser spots on a gold film (50nm thick) optically coupled to the Dove prism. Scale bar is 200μm. We call this assembly as triple-trap configuration. (c) Optical bright-field image of plasmofluidic assembly of Ag nanoparticles at gold film-water interface due to excitation shown in figure 5.2b. The excitation laser was filtered before imaging. Scale bar is 200μm. Note that the assembly of nanoparticles is denser at the excitation points and at the orthocenter of the three excitation spots indicated by dotted circle. (d) Simulated electric near-field distribution of the three laser spots at gold-water interface. The geometry of the simulation was identical to the experimental configuration. (e) Schematic of the forces involved in the plasmofluidic trapping process.

excitation points.

To understand the assembly pattern, we mapped the electric fields at metal-fluid interface through full-wave 3-D FDTD simulations. The near-field |E| map is shown in figure 5.2d. We see that the electromagnetic fields from the propagating plasmons of the metal film interact with each other. The collective interference of SPP waves from three excitation points results in a unique pattern of nearfield at the metal-fluid interface, which in turn governs both optical and hydrodynamic forces on the nanoparticles. The schematic of the interaction of the forces is shown in figure 5.2e. At the orthocenter, two predominant forces get involved but in opposite directions: one is gradient force due to laser excitation and other is the convective force due to heating by the same[124,

173, 174]. Thus, the assembly at orthocenter is due to the balance between two counter steering forces in the plasmofluidic environment. To explain the nanoparticles chain formation, we primarily attribute the SPP interference (figure 5.2d) at the metal-fluid interface, though in such plasmofluidic systems all the effects are codependent and thus complex in nature.

5.3.2 Kinetics of triple-spot-excited plasmofluidic assembly of silver nanoparticles

To obtain further insight into the assembly process, we analyzed the variation of nanoparticles density and position with time. In figure 5.3a the growth kinetics of the nanoparticles assembly at the excitation points is shown. The growth plot fits well with a sigmoidal curve. It took only few minutes ($4 - 5$min) for the nanoparticles to assemble and after a particular time the assembly process seems to be saturated. This type of assembly kinetics was reported in our previous paper[171]. However, the scenario at the orthocenter is quite different as we envisage distinct forces involved in this assembly process. Figure 5.3b represents the growth kinetics at the orthocenter. It is evident from the plot that the saturation of the nanoparticle assembly had not been achieved within the experimental time limit i.e. ~ 15 minutes. As the assembly process at the orthocenter depends on the three excitation points and the balance between two counter steering forces, the assembly process is complicated. The effect of the complex nature of this process is perceived from the dynamics of the assembly process

It is also important to notice that significant number of nanoparticles escape from the orthocenter at regular intervals. Furthermore, tracing the central position of the nanoparticle-assembly shows (figure 5.3c) that, the assembly position at the orthocenter is not static, unlike at the excitation spots. The variations in position of the nanoparticles are compared in figure 5.3d and it is apparent that at the orthocenter the nanoparticles assembly fluctuates over a 100μm diameter whereas the assembly at the excitation points is very compact. So this analysis helped us to understand at least the basic mechanism behind the multiple-excitation plasmofluidic assembly process. Though the whole

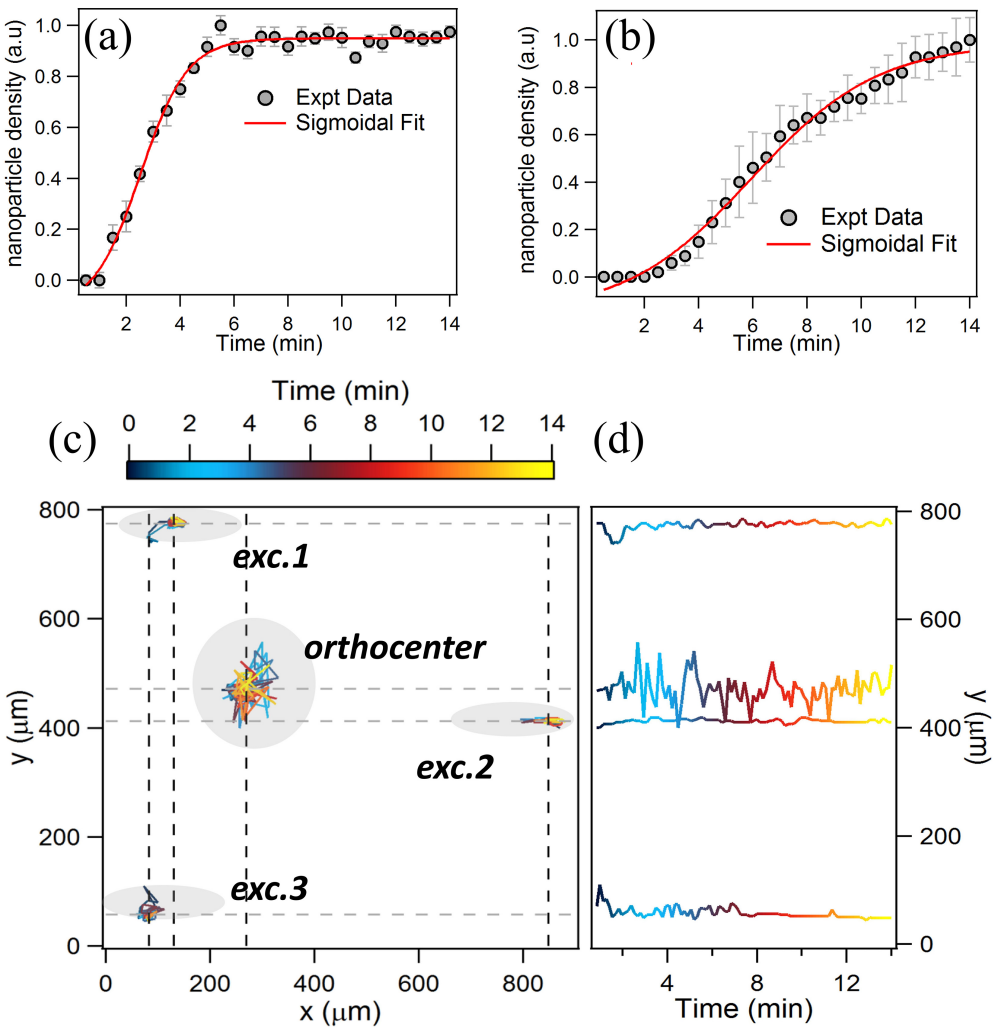

Figure 5.3: Kinetics of the nanoparticle assembly in the triple-trap configuration. (a) Variation of nanoparticle-density at an excitation point as a function of time. (b) Variation of the nanoparticle density at the orthocenter of the triple-trap. (c) Spatio-temporal variation of the center of nanoparticle assembly at four different locations: excitations 1, 2 and 3, and at the orthocenter. (d) Spatial variation of the same centers along y-axis as function of time. Note that the fluctuation of the center of the orthocenter is more pronounced compared to other locations.

process is byzantine to realize, still one can be curious enough to introduce one more excitation into our experimental configuration.

5.3.3 Quadruple-spot-excited plasmofluidic assembly of Ag nanoparticles

Thus we performed the assembly experiment with four-spot-excitation geometry. Figure 5.4a shows the dark-field image of the excitation geometry. In figure 5.4b the FDTD

simulation reveals the nearfield distribution due to excitation of four spots. We can see that the SPP interference forms a unique pattern on the plasmonic film, which in turn governs the formation of the nanoparticles chain. We would like to clarify that the length scales of the simulation (around 2μm$\times 2\mu$m) and the experiments (200μm scale bar in figure 5.4) were different. A large, millimetre scale 3D simulation is computationally expensive, and currently beyond our resources. The simulation results that we have shown are indicative of the kind of interference that we can expect when we have four-spot illumination. It is not the exact description of the field profile in the experiment.

In the context of the experiments, there are two components of the electric field. One is the localized plasmon field at the location of illumination, and the other is the propagating surface plasmon polariton field that is delocalized. The propagating fields originate from the four different excitations, and interfere with each other. This interaction leads to a complex field pattern, which can facilitate potential wells that are much deeper than the ones produced at the location of excitation.

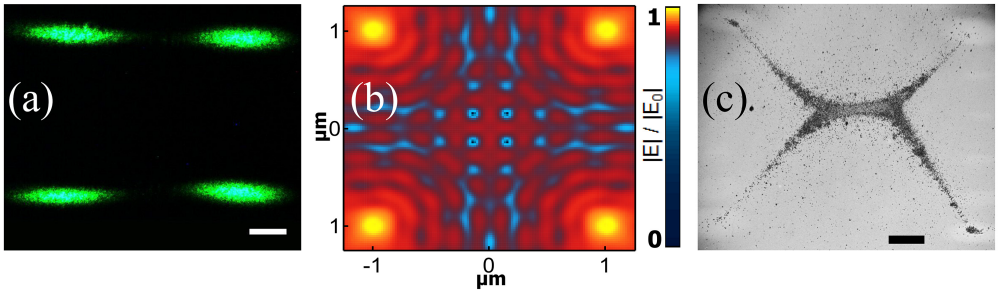

Figure 5.4: Plasmofluidic assembly of nanoparticles using quadruple-trap configuration. (a) Optical dark-field image of the four, evanescently-excited 532nm laser spots on a gold film (50nm thick) optically coupled to the Dove prism. Scale bar is 200μm. (b) Simulated electric near-field distribution of the four laser spots at gold-water interface. The geometry of the simulation was identical to the experimental configuration. Plasmonic interference patterns can be clearly observed. (c) Optical bright-field image of plasmofluidic assembly of Ag nanoparticles at gold film-water interface due to excitation shown in figure 5.4a. Scale bar is 200μm. The nanoparticle densities at the corners of the geometry are different due to small variance in the laser powers.

Figure 5.4c presents the bright-field image of the nanoparticle assembly with the excitation geometry shown in figure 5.4a. For such geometry the assembly process followed the same basic pattern of creating two types of assembly: one at the excitation

point and other at the central part. We emphasize here that there is some accumulation of nanoparticles at the point of excitation, but the in-plane field gradient is such that the majority of nanoparticles tend to assimilate at the location where the potential well is steeper. The difference in the nanoparticle density at the four excitation spots occurs due to slight inequality in power.

The extrapolation from three-spots-excitation to four-spots-excitation geometry in plasmofluidic field resulted in interesting patterns of the nanoparticles-assembly and can be further tailored by changing the excitation points. Since this assembly technique is reconfigurable in fluid phase, one can draw any desired sketch of nanoparticles-assembly on a single substrate by merely changing the excitation geometry.

5.3.4 Aligned assembly of silver nanowires in plasmofluidic field

Next we asked whether this method could be extrapolated to anisotropic nanogeometries. To test the versatility of our method, we implemented this technique to assemble one-dimensional nanostructures. Herein, we used Ag nanowires (prepared by polyol process[172].) suspended in aqueous medium; the assembly process was performed in dual spot excitation geometry and we observed not only the assembly of nanowires but their alignment too.

Figure 5.5a shows the dark field image of dual spot excitation of the unstructured thin film. The portion marked by dotted box was closely monitored by using $\times 60$-magnification objective lens. The FDTD simulation for similar excitation geometry reveals a typical SPP interference pattern with consecutive maxima and minima, shown in figure 5.5b. This type of SPP interference not only assembles the Ag nanowires, but also helps to align in a particular orientation. Figure 5.5c shows the aligned assembly of Ag nanowires on an unstructured film in dual excitation geometry. Thus, we see that the same SPP interference which was attributed to the formation of nanoparticles-chain can be utilized to align much heavier nanowires at the metal-fluid interface. Although the nanowires assembled around the illumination points, their alignment was not satisfactory.

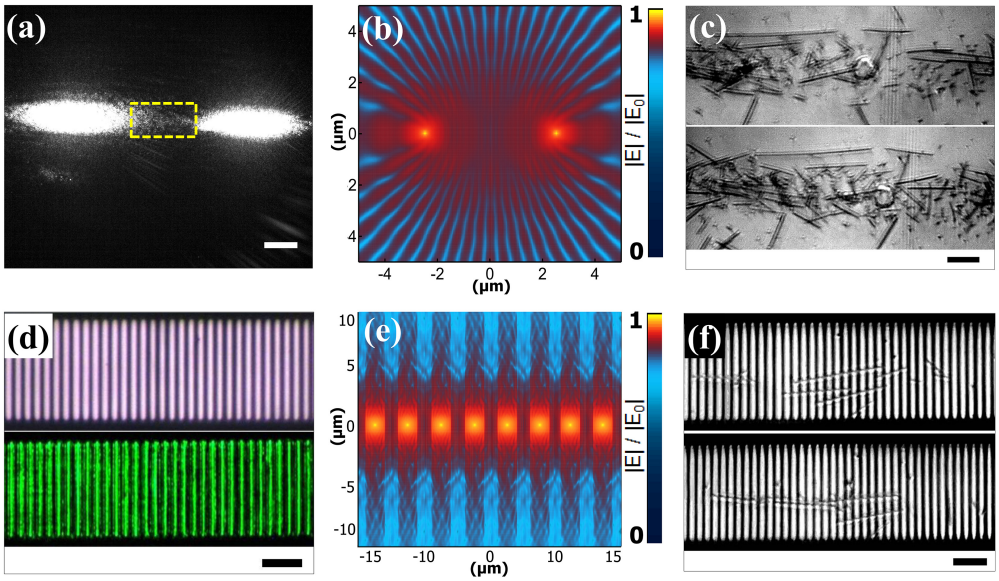

Figure 5.5: Assembling Ag nanowires using unstructured and structured plasmonic thin film. (a) Optical dark-field image of dual-trap configuration. The region marked with yellow dashed box is the region of interest in our experiments. Scale bar is 200 um. (b) Simulated electric near-field distribution of the two laser spots at gold-water interface. Plasmonic interference patterns can be clearly observed. (c) Optical bright field images at Ag nanowire assembly at two different instances. We found weak alignment of the longer nanowires. (d) Optical bright-field (top) and dark-field (bottom) images of structured gold film evanescently-excited using a single 532nm laser beam. The length of each Au strip was 50μm, width was 2μm and the thickness was 50nm; and the gap between two consecutive strips was 2μm. (e) Simulated electric near-field distribution of a single laser spot exciting the gold strip-water interface. (f) Optical bright-field snap-shots of the aligned nanowires at two different instances. We found the trap to be stiffer and confined to smaller area compared to dual-trap configuration. All scale bars are 20μm long. Note that experiments in first row of the figure 5.5a were performed using dual evanescent-excitation, whereas experiments in second row was performed using a single evanescent excitation.

This motivated us to repeat the experiment with a structured plasmonic film. The gold thin film was patterned as strips of 2μm width each and the gap between two consecutive strips was 2μm (see experimental section 5.2.1 for more details). In this experiment only a single-spot excitation was used. Figure 5.5d is the optical bright and dark-field images of the structured substrate. The nearfield distribution was simulated in FDTD (figure 5.5e) which revealed a pattern of consecutive field maxima and minima which actually aided the nanowire alignment. The bright field image of assembled Ag nanowires is shown in figure 5.5f. The clearly defined field pattern created by the structured thin film assembled and aligned the heavier nanowires with greater precision. The power density used for this experiment was approximately of 100W/cm^2. The two

important aspects of this aligned assembly are reversibility and ease. Thus, one can recreate this alignment of nanowires for multiple cycles of experiments with a very low power excitation.

5.4 Summary

The motivation behind this study was twofold. First, we wanted to explore the possibility of plasmonic-nanoparticle assemblies due to three and four evanescent-wave plasmon excitation at metal-fluid interface. Our results showed that for triple-trap configuration, nanoparticles assembled not only at the excitation points but also at the orthocentre of the triangle formed between the three excitation spots. The reason for such assembly was mainly due to the SPP interference from three different excitations. However, the convective forces resulting from plasmonic heating may also contribute towards assembly formation. Kinetic studies based on particle-tracking at various locations in the assembly indicated a dynamic equilibrium, with the assembly at the orthocentre exhibiting greater fluctuation in its position compared to the excitation spots. For the four-spot configuration, we observed interesting assembly patterns which were mainly governed by the plasmon interference patterns. Numerical simulations for both triple and four spot illuminations confirmed plasmon interference, and were in agreement with our experimental observations. The second motivation of our study was to explore the possibilities of assembling anisotropic plasmonic geometries, such as Ag nanowires, using our method. We found that dual-trap configuration can indeed assemble and weakly align nanowires in liquid, and the directionality of the alignment was governed by interference pattern of counter-propagating surface plasmon polaritons at metal-fluid interface. Interestingly, we also found that nanowires can also be assembled and aligned, with better efficiency, using structured metal films and a single evanescent-wave excitation of surface plasmon polaritons. All these experiments indicated that plasmon excitation and interference can be harnessed for micron to millimetre scale reversible-assembly of nanoparticles and elongated nanostructures at metal-fluid interface. There are new directions that our work can lead to, such as reconfigurable plasmonic metamaterials at metal-fluid interface, where control of various parameters

of light - intensity, polarization, phase, etc. can be controlled in fluids by tailoring the geometrical arrangements of nanoparticle assemblies. Such reconfigurable optical platforms can be further harnessed for nano and micro-optical circuits and devices in fluidic environments. In addition to that, nanoparticle assemblies may be harnessed as test-beds of various plasmofluidic effects where understanding the interaction between SPPs and the surrounding fluids is of fundamental interest.

Conclusion and Outlook

Controlling electromagnetic fields at nanoscale is an important aspect in nanoplasmonics[4, 25, 175]. At the same time, studying molecular properties at single copy limit has tremendous implications in chemical and biological sensing[16, 76, 176, 177] as well as in understanding such molecular properties that are averaged over in ensemble measurements[178–180]. Single-molecule surface-enhanced Raman scattering is a specific technique that connects both the areas together[175]. Therefore, single-molecule SERS has gained a lot of attention and been an active area of research from the last two decades[83]. Though unlike fluorescence technique, SMSERS has yet not been a routine single-molecule tool for practical applications, still it is true that in near future SMSERS has a greater prospect than any other single molecule spectroscopy techniques. However to harness SMSERS in its true capacity there is an imperative need to develop a reliable methodology as well as various SMSERS detection platforms.

In this thesis we mainly worked on the development of the SMSERS detection platform which includes the plasmonic substrate and microscopy system. However, to understand our SMSERS results properly, in chapter 2, we have given a brief description of the experimental strategies and the statistical methods, commonly utilised for SMSERS.

In chapter 3 we provided the experimental proof of the SMSERS sensitivity of Ag-core Au-shell (Ag@Au) bimetallic colloidal nanoparticles in fluid phase with conventional focused field SERS microscopy technique. Recently, to prepare nanoplasmonic substrates the top-down nanofabrication technique has been a popular practice as they can provide precise geometry as per application. But the disadvantage of such fabricated nanostructures is that they always need a substrate to hold themselves which is not much adoptable for many cases, especially to probe in vivo biological problems. Also in various chemical and biological platforms, for solution based SERS measurements

the colloidal plasmonic nanoparticles are crucial. Thus the necessity in the development of such colloidal nanostructures still persists. In this work our motto was to find a novel SMSERS substrate based on the bottom-up synthesis which can be an alternative to silver nanoparticles. Here we did not innovate these Ag@Au nanoparticles rather we introduced them for SMSERS study. The gold shell on the surface makes these nanoparticles biocompatible and this opens up a possibility of SMSERS applications in biological environment. Also the tunable LSPR property of Ag@Au nanoparticles can be utilized for sensing applications in a wide range of wavelength. Another prospect of these bimetallic nanoparticles is that by preparing hierarchical plasmonic structures using them, many existing applications as well as fundamental aspects can be revisited in a new light.

In the next project we introduced a new microscopy system for single-molecule SERS. Though the evanescent-field based microscopy has already been used for fluorescence[44, 181] as well as for SERS detection[182–184], it has never achieved that sophistication to detect SMSERS signals. In this work we have made this possible. We utilised the Kretschmann configuration to harness the SPP field for trapping a large number of the plasmonic nanoparticles at the metal-fluid interface. These assembled nanoparticles further led to the formation of plasmonic hot-spots. Fascinatingly, the formation of such hot-spots are reversible in nature i.e. in the presence of the SPP field, the nanoparticles get assembled, but while terminating the excitation the assembly collapses to the initial colloidal phase. This particular advantage can make this microscopy adoptable in various microfluidic based applications. By this approach we have breached the problem of irreversible-aggregation of nanoparticles by chemical means to facilitate hot-spots. Another advantage of this microscopy technique is that the excitation power density for SMSERS is much lower than the conventional focused-field excitation and that makes this platform compatible to biological applications. Besides trapping, using this technique the nanoparticles can be spatially manipulated at the film-water interface. Such precise control over the trapped nanoparticles can have implications in optofluidic chemical and biochemical reactors. Therefore in this work our contribution is not only limited to the SMSERS detection platform but also this can provide a mould to shape many new developments.

The last part of my thesis work is an interesting consequence of curiosity which is an important part of scientific research. We first divided the excitation beam and made two excitation spots to see the outcome. Interestingly we saw that the assembly of the nanoparticles took a certain distribution at the metal-fluid interface. This motivated us to investigate further. Then we stepped further with an additional excitation spot and we observed the unique phenomenon of patterned assembly. Structuring the excitation field not only gave a structured assembly, but also revealed a complex physical process within. After that we extended this investigation with four excitation spots. With all the observations we can consider this platform to be a preamble for plasmofluidic dynamic lithography of nanostructures. Furthermore, employing this technique one-dimensional nano-structures can be assembled and aligned. Note that, all the assembly patterns shown in this work were performed in fluid phase and were reconfigurable. Thus such work can further be utilized for fluid-phase micro and nano-optical circuits, reconfigurable metamaterials etc. Also this platform can be further improvised for trapping and precisely manipulating a single nano-object to uncover many more mysteries.

Since the time span of the PhD is limited we are bound by the deadline. I seek to walk further along the same path that I have already chosen half a decade ago.

Bibliography

[1]C. V. RAMAN and K. S. KRISHNAN, "A New Type of Secondary Radiation", Nature **121**, 501–502 (1928).

[2]C. Raman and K. Krishnan, "A new radiation", Indian Journal of Physics **2**, 387–398 (1928).

[3]R. Aroca, *Surface-Enhanced Vibrational Spectroscopy* (John Wiley and Sons, Chichester, 2006).

[4]E. C. L. Ru and P. G. Etchegoin, *Principles of Surface-Enhanced Raman Spectroscopy and related plasmonic effects,* (Elsevier, Amsterdam, 2009).

[5]W. Kiefer, "Recent Advances in linear and nonlinear Raman spectroscopy I", Journal of Raman Spectroscopy **38**, 1538–1553 (2007).

[6]L. A. Nafie, "Recent advances in linear and nonlinear Raman spectroscopy. Part VIII", Journal of Raman Spectroscopy **45**, 1326–1346 (2014).

[7]M. Fleischmann, P. Hendra, and A. McQuillan, "Raman spectra of pyridine adsorbed at a silver electrode", Chemical Physics Letters **26**, 163 –166 (1974).

[8]D. L. Jeanmaire and R. P. V. Duyne, "Surface raman spectroelectrochemistry: part i. heterocyclic, aromatic, and aliphatic amines adsorbed on the anodized silver electrode", Journal of Electroanalytical Chemistry and Interfacial Electrochemistry **84**, 1 –20 (1977).

[9]M. G. Albrecht and J. A. Creighton, "Anomalously intense raman spectra of pyridine at a silver electrode", Journal of the American Chemical Society **99**, 5215–5217 (1977).

[10]F. W. King, R. P. Van Duyne, and G. C. Schatz, "Theory of raman scattering by molecules adsorbed on electrode surfaces", The Journal of Chemical Physics **69**, 4472–4481 (1978).

[11]G. C. Schatz and R. P. Van Duyne, *Electromagnetic mechanism of surface-enhanced spectroscopy* (Wiley Online Library, 2002).

[12]M. Moskovits, "Surface-enhanced spectroscopy", Rev. Mod. Phys. **57**, 783–826 (1985).

[13]A. Campion and P. Kambhampati, "Surface-enhanced raman scattering", Chem. Soc. Rev. **27**, 241–250 (1998).

[14]P. L. Stiles, J. A. Dieringer, N. C. Shah, and R. P. V. Duyne, "Surface-enhanced raman spectroscopy", Annual Review of Analytical Chemistry **1**, 601–626 (2008).

[15]S. Schlücker, "Surface-enhanced raman spectroscopy: concepts and chemical applications", Angewandte Chemie International Edition **53**, 4756–4795 (2014).

[16]K. A. Willets and R. P. Van Duyne, "Localized surface plasmon resonance spectroscopy and sensing", Annu. Rev. Phys. Chem. **58**, 267–297 (2007).

[17]H. Raether, *Surface plasmons on smooth and rough surfaces and on gratings* (Springer, 1988).

[18]M. S. A., *Plasmonics: fundamentals and applications* (Springer, 2007).

[19]J. R. S. A. A. Maradudin and W. L. Barnes, *Modern plasmonics, Vol. 4* (Elsevier, 2014).

[20]W. L. Barnes, A. Dereux, and T. W. Ebbesen, "Surface plasmon subwavelength optics", Nature **424**, 824–830 (2003).

[21]P. Liao and A Wokaun, "Lightning rod effect in surface enhanced raman scattering", The Journal of Chemical Physics **76**, 751–752 (1982).

[22]J. Gersten and A. Nitzan, "Electromagnetic theory of enhanced raman scattering by molecules adsorbed on rough surfaces", The Journal of Chemical Physics **73**, 3023–3037 (1980).

[23]M. Kerker, D.-S. Wang, and H Chew, "Surface enhanced raman scattering (sers) by molecules adsorbed at spherical particles: errata", Applied Optics **19**, 4159–4174 (1980).

[24]M. Franken, C Poelma, and J Westerweel, "Nanoscale contact line visualization based on total internal reflection fluorescence microscopy", Optics express **21**, 26093–26102 (2013).

[25]L. Novotny and B. Hecht, *Principles of nano-optics* (Cambridge university press, 2012).

[26]P Sruthi, "Plasmonic and organic nanostructures in evanescent optical field", Master's Thesis (Indian Institute of Science Education and Rsearch, Pune, India, 2013).

[27]E. Kretschmann and H. Raether, "Radiative decay of non radiative surface plasmons excited by light", Zeits. fur Naturf. **23A**, 2135–2136 (1968).

[28]A. Otto, "Âşexcitation of nonradiative surface plasma waves in silver by the method of frustrated total refection", Zeits. fur Phys. A. **216**, 398–410 (2005).

[29]M Moskovits and D. DiLella, "Surface-enhanced raman spectroscopy of benzene and benzene-d6 adsorbed on silver", The Journal of Chemical Physics **73**, 6068–6075 (1980).

[30]M Moskovits, "Erratum: surface selection rules [j. chem. phys. 77, 4408 (1982)]", The Journal of Chemical Physics **79**, 1558–1558 (1983).

[31]G. R. Erdheim, R. L. Birke, and J. R. Lombardi, "Surface enhanced raman spectrum of pyrazine. observation of forbidden lines at the electrode surface", Chemical Physics Letters **69**, 495 –498 (1980).

[32]D.-Y. Wu, S. Duan, B. Ren, and Z.-Q. Tian, "Density functional theory study of surface-enhanced raman scattering spectra of pyridine adsorbed on noble and transition metal surfaces", Journal of Raman Spectroscopy **36**, 533–540 (2005).

[33]J. Creighton, "The resonance raman contribution to sers: pyridine on copper or silver in aqueous media", Surface Science **173**, 665 –672 (1986).

[34]J. I. Gersten, R. L. Birke, and J. R. Lombardi, "Theory of enhance i light scattering from molecules adsorbed at the metal-solution interface", Phys. Rev. Lett. **43**, 147–150 (1979).

[35]M. E. Lippitsch, "Ground-state charge transfer as a mechanism for surface-enhanced raman scattering", Phys. Rev. B **29**, 3101–3110 (1984).

[36]K. Kneipp, M. Moskovits, and H. Kneipp, *Surface-enhanced raman scattering: physics and applications*, Vol. 103 (Springer Science & Business Media, 2006).

[37]S. J. Lee, Z. Guan, H. Xu, and M. Moskovits, "Surface-enhanced raman spectroscopy and nanogeometry: the plasmonic origin of sers", The Journal of Physical Chemistry C **111**, 17985–17988 (2007).

[38]K. A. Willets, "Super-resolution imaging of sers hot spots", Chem. Soc. Rev **43**, 3854–3864 (2014).

[39]K. Kneipp, Y. Wang, H. Kneipp, I. Itzkan, R. R. Dasari, and M. S. Feld, "Population pumping of excited vibrational states by spontaneous surface-enhanced raman scattering", Phys. Rev. Lett. **76**, 2444–2447 (1996).

[40]T. L. Haslett, L. Tay, and M. Moskovits, "Can surface-enhanced raman scattering serve as a channel for strong optical pumping?", The Journal of Chemical Physics **113**, 1641–1646 (2000).

[41]L. R. E. C. Maher R.C., Etchegoin P. G. and C. L. F., "A conclusive demonstration of vibrational pumping under surface enhanced raman scattering conditions", The Journal of Physical Chemistry B **110**, 11757–11760 (2006).

[42]C. M. Galloway, E. C. Le Ru, and P. G. Etchegoin, "Single-molecule vibrational pumping in sers", Phys. Chem. Chem. Phys. **11**, 7372–7380 (2009).

[43]E. CortÃl's, P. G. Etchegoin, E. C. L. Ru, A. Fainstein, M. E. Vela, and R. C. Salvarezza, "Monitoring the electrochemistry of single molecules by surface-enhanced raman spectroscopy", Journal of the American Chemical Society **132**, 18034–18037 (2010).

[44]W. E. Moerner and D. P. Fromm, "Methods of single-molecule fluorescence spectroscopy and microscopy", Review of Scientific Instruments **74** (2003).

[45]A. Ahmed and R. Gordon, "Single molecule directivity enhanced raman scattering using nanoantennas", Nano letters **12**, 2625–2630 (2012).

[46]S. Nie and S. R. Emory, "Probing single molecules and single nanoparticles by surface-enhanced raman scattering", science **275**, 1102–1106 (1997).

[47]K. Kneipp, Y. Wang, H. Kneipp, L. T. Perelman, I. Itzkan, R. R. Dasari, and M. S. Feld, "Single molecule detection using surface-enhanced raman scattering (sers)", Phys. Rev. Lett. **78**, 1667–1670 (1997).

[48]M. Kreibig, U.; Vollmer, *Optical Properties of Metal Clusters,* (Springer: Berlin, 1995).

[49]A. B. Zrimsek, A.-I. Henry, and R. P. Van Duyne, "Single molecule surface-enhanced raman spectroscopy without nanogaps", The Journal of Physical Chemistry Letters **4**, 3206–3210 (2013).

[50]M. Michaels, Amy M. Nirmal and L. E. Brus, "Surface enhanced raman spectroscopy of individual rhodamine 6g molecules on large ag nanocrystals", Journal of the American Chemical Society **121**, 9932–9939 (1999).

[51]C. J. L. Constantino, T. Lemma, P. A. Antunes, and R. Aroca*, "Single-molecule detection using surface-enhanced resonance raman scattering and langmuir-blodgett monolayers", Analytical Chemistry **73**, 3674–3678 (2001).

[52]A. Weiss, and G. Haran*, "Time-dependent single-molecule raman scattering as a probe of surface dynamics", The Journal of Physical Chemistry B **105**, 12348–12354 (2001).

[53]E. C Ru*, M. Meyer, and P. G. Etchegoin*, "Proof of single-molecule sensitivity in surface enhanced raman scattering (sers) by means of a two-analyte technique", The Journal of Physical Chemistry B **110**, 1944–1948 (2006).

[54]J. A. Dieringer, K. L. Wustholz, D. J. Masiello, J. P. Camden, S. L. Kleinman, G. C. Schatz, and R. P. V. Duyne, "Surface-enhanced raman excitation spectroscopy of a single rhodamine 6g molecule", Journal of the American Chemical Society **131**, 849–854 (2009).

[55]M. Moskovits, "Surface-enhanced raman spectroscopy: a brief retrospective", Journal of Raman Spectroscopy **36**, 485–496 (2005).

[56]P. Bharadwaj, B. Deutsch, and L. Novotny, "Optical antennas", Advances in Optics and Photonics **1**, 438–483 (2009).

[57]L. Novotny and N. Van Hulst, "Antennas for light", Nature Photonics **5**, 83–90 (2011).

[58]A. Dasgupta, "Localized optical-fields and directional far-field emission from plasmonic nanojunctions", Doctoral Thesis (Indian Institute of Science Education and Rsearch, Pune, India, 2016).

[59]B. Luk'yanchuk, N. I. Zheludev, S. A. Maier, N. J. Halas, P. Nordlander, H. Giessen, and C. T. Chong, "The fano resonance in plasmonic nanostructures and metamaterials", Nature materials **9**, 707–715 (2010).

[60]J. B. Lassiter, H. Sobhani, J. A. Fan, J. Kundu, F. Capasso, P. Nordlander, and N. J. Halas, "Fano resonances in plasmonic nanoclusters: geometrical and chemical tunability", Nano letters **10**, 3184–3189 (2010).

[61]L. Chuntonov and G. Haran, "Trimeric plasmonic molecules: the role of symmetry", Nano letters **11**, 2440–2445 (2011).

[62]L. Chuntonov and G. Haran, "Effect of symmetry breaking on the mode structure of trimeric plasmonic molecules", The Journal of Physical Chemistry C **115**, 19488–19495 (2011).

[63]Y. Zhang, Y.-R. Zhen, O. Neumann, J. K. Day, P. Nordlander, and N. J. Halas, "Coherent anti-stokes raman scattering with single-molecule sensitivity using a plasmonic fano resonance", Nature communications **5** (2014).

[64]V. Aswathy, P. P. Patra, and G. P. Kumar, "Geometry-dependent anti-stokes sers radiation patterns from gold nanorod dimers", Journal of Optics **17**, 114011 (2015).

[65]V. K. Valev, J. J. Baumberg, C. Sibilia, and T. Verbiest, "Chirality and chiroptical effects in plasmonic nanostructures: fundamentals, recent progress, and outlook", Advanced Materials **25**, 2517–2534 (2013).

[66]S. Palomba, M. Danckwerts, and L. Novotny, "Nonlinear plasmonics with gold nanoparticle antennas", Journal of Optics A: Pure and Applied Optics **11**, 114030 (2009).

[67]K. Thyagarajan, S. Rivier, A. Lovera, and O. J. Martin, "Enhanced second-harmonic generation from double resonant plasmonic antennae", Optics express **20**, 12860–12865 (2012).

[68]K. Thyagarajan, J. Butet, and O. J. Martin, "Augmenting second harmonic generation using fano resonances in plasmonic systems", Nano letters **13**, 1847–1851 (2013).

[69]G. F. Walsh and L. Dal Negro, "Enhanced second harmonic generation by photonic–plasmonic fano-type coupling in nanoplasmonic arrays", Nano letters **13**, 3111–3117 (2013).

[70]K. Li, M. I. Stockman, and D. J. Bergman, "Self-similar chain of metal nanospheres as an efficient nanolens", Physical review letters **91**, 227402 (2003).

[71]B. Ding, Z. Deng, H. Yan, S. Cabrini, R. N. Zuckermann, and J. Bokor, "Gold nanoparticle self-similar chain structure organized by dna origami", Journal of the American Chemical Society **132**, 3248–3249 (2010).

[72]D. K. Gramotnev and S. I. Bozhevolnyi, "Plasmonics beyond the diffraction limit", Nature photonics **4**, 83–91 (2010).

[73]M. L. Brongersma, J. W. Hartman, and H. A. Atwater, "Electromagnetic energy transfer and switching in nanoparticle chain arrays below the diffraction limit", Physical Review B **62**, R16356 (2000).

[74]S. A. Maier, P. G. Kik, H. A. Atwater, S. Meltzer, E. Harel, B. E. Koel, and A. A. Requicha, "Local detection of electromagnetic energy transport below the diffraction limit in metal nanoparticle plasmon waveguides", Nature materials **2**, 229–232 (2003).

[75]A. Dasgupta and G. P. Kumar, "Palladium bridged gold nanocylinder dimer: plasmonic properties and hydrogen sensitivity", Applied optics **51**, 1688–1693 (2012).

[76]J. N. Anker, W. P. Hall, O. Lyandres, N. C. Shah, J. Zhao, and R. P. Van Duyne, "Biosensing with plasmonic nanosensors", Nature materials **7**, 442–453 (2008).

[77]J. W. Chon and K. Iniewski, *Nanoplasmonics: advanced device applications* (CRC Press, 2013).

[78]A. Ahmed, Y. Pang, G. Hajisalem, and R. Gordon, "Antenna design for directivity-enhanced raman spectroscopy", International Journal of Optics **2012** (2012).

[79]D. Wang, W. Zhu, M. D. Best, J. P. Camden, and K. B. Crozier, "Directional raman scattering from single molecules in the feed gaps of optical antennas", Nano letters **13**, 2194–2198 (2013).

[80]D. Wang, W. Zhu, Y. Chu, and K. B. Crozier, "High directivity optical antenna substrates for surface enhanced raman scattering", Advanced Materials **24**, 4376–4380 (2012).

[81]K Kneipp, G. Harrison, S. Emory, and S Nie, "Single-molecule raman spectroscopy: fact or fiction?", Chimia **53**, 35–37 (1999).

[82]E. J. Blackie, E. C. L. Ru, and P. G. Etchegoin, "Single-molecule surface-enhanced raman spectroscopy of nonresonant molecules", Journal of the American Chemical Society **131**, 14466–14472 (2009).

[83]E. C. Le Ru and P. G. Etchegoin, "Single-molecule surface-enhanced raman spectroscopy", Annual Review of Physical Chemistry **63**, 65–87 (2012).

[84]H. Xu, E. J. Bjerneld, M. Käll, and L. Börjesson, "Spectroscopy of single hemoglobin molecules by surface enhanced raman scattering", Physical review letters **83**, 4357 (1999).

[85]K. Kneipp, H. Kneipp, G. Deinum, I. Itzkan, R. R. Dasari, and M. S. Feld, "Single-molecule detection of a cyanine dye in silver colloidal solution using near-infrared surface-enhanced raman scattering", Applied spectroscopy **52**, 175–178 (1998).

[86]P Etchegoin, R. C. Maher, L. Cohen, H Hartigan, R. Brown, M. Milton, and J. Gallop, "New limits in ultrasensitive trace detection by surface enhanced raman scattering (sers)", chemical physics letters **375**, 84–90 (2003).

[87]P. J. Goulet, N. P. Pieczonka, and R. F. Aroca, "Mapping single-molecule serrs from langmuir–blodgett monolayers on nanostructured silver island films", Journal of raman spectroscopy **36**, 574–580 (2005).

[88]E Blackie, E. Le Ru, M Meyer, M Timmer, B Burkett, P Northcote, and P. Etchegoin, "Bi-analyte sers with isotopically edited dyes", Physical Chemistry Chemical Physics **10**, 4147–4153 (2008).

[89]A. B. Zrimsek, N. L. Wong, and R. P. Van Duyne, "Single molecule surface-enhanced raman spectroscopy: a critical analysis of the bianalyte versus isotopologue proof", The Journal of Physical Chemistry C **120**, 5133–5142 (2016).

[90]E. Le Ru, P. Etchegoin, and M Meyer, "Enhancement factor distribution around a single surface-enhanced raman scattering hot spot and its relation to single molecule detection", The Journal of chemical physics **125**, 204701 (2006).

[91]E. Le Ru, E Blackie, M. Meyer, and P. G. Etchegoin, "Surface enhanced raman scattering enhancement factors: a comprehensive study", The Journal of Physical Chemistry C **111**, 13794–13803 (2007).

[92]P. G. Etchegoin, M. Meyer, and E. Le Ru, "Statistics of single molecule sers signals: is there a poisson distribution of intensities?", Physical Chemistry Chemical Physics **9**, 3006–3010 (2007).

[93]J. A. Dieringer, R. B. Lettan, K. A. Scheidt, and R. P. Van Duyne, "A frequency domain existence proof of single-molecule surface-enhanced raman spectroscopy", Journal of the American Chemical Society **129**, 16249–16256 (2007).

[94]P. G. Etchegoin, M. Meyer, E Blackie, and E. C. Le Ru, "Statistics of single-molecule surface enhanced raman scattering signals: fluctuation analysis with multiple analyte techniques", Analytical chemistry **79**, 8411–8415 (2007).

[95]I. T. Jolliffe, *Principal Component Analysis* (JSpringer: Berlin, Germany, 2002).

[96]G. P. Kumar, "Plasmonic nano-architectures for surface enhanced raman scattering: a review", Journal of Nanophotonics **6**, 064503–1 (2012).

[97]C. Beer, R. Foldbjerg, Y. Hayashi, D. S. Sutherland, and H. Autrup, "Toxicity of silver nanoparticles-nanoparticle or silver ion?", Toxicology letters **208**, 286–292 (2012).

[98]M. E. Samberg, S. J. Oldenburg, and N. A. Monteiro-Riviere, "Evaluation of silver nanoparticle toxicity in skin in vivo and keratinocytes in vitro", Environmental health perspectives **118**, 407 (2010).

[99]R. A. Sperling, P. R. Gil, F. Zhang, M. Zanella, and W. J. Parak, "Biological applications of gold nanoparticles", Chemical Society Reviews **37**, 1896–1908 (2008).

[100]C. J. Murphy, A. M. Gole, J. W. Stone, P. N. Sisco, A. M. Alkilany, E. C. Goldsmith, and S. C. Baxter, "Gold nanoparticles in biology: beyond toxicity to cellular imaging", Accounts of chemical research **41**, 1721–1730 (2008).

[101]R. Shukla, V. Bansal, M. Chaudhary, A. Basu, R. R. Bhonde, and M. Sastry, "Biocompatibility of gold nanoparticles and their endocytotic fate inside the cellular compartment: a microscopic overview", Langmuir **21**, 10644–10654 (2005).

[102]P. Lee and D Meisel, "Adsorption and surface-enhanced raman of dyes on silver and gold sols", The Journal of Physical Chemistry **86**, 3391–3395 (1982).

[103]I. Srnová-Šloufová, F. Lednickỳ, A. Gemperle, and J. Gemperlová, "Core-shell (ag) au bimetallic nanoparticles: analysis of transmission electron microscopy images", Langmuir **16**, 9928–9935 (2000).

[104]Y. Cui, B. Ren, J.-L. Yao, R.-A. Gu, and Z.-Q. Tian, "Synthesis of agcoreaushell bimetallic nanoparticles for immunoassay based on surface-enhanced raman spectroscopy", The Journal of Physical Chemistry B **110**, 4002–4006 (2006).

[105]G. P. Kumar, S Shruthi, B Vibha, B. A. Reddy, T. K. Kundu, and C. Narayana, "Hot spots in ag core-au shell nanoparticles potent for surface-enhanced raman scattering studies of biomolecules", The Journal of Physical Chemistry C **111**, 4388–4392 (2007).

[106]B. L. Darby and E. C. Le Ru, "Competition between molecular adsorption and diffusion: dramatic consequences for sers in colloidal solutions", Journal of the American Chemical Society **136**, 10965–10973 (2014).

[107]A. Otto, A Bruckbauer, and Y. Chen, "On the chloride activation in sers and single molecule sers", Journal of molecular structure **661**, 501–514 (2003).

[108]G. Turrell and J. Corset, *Raman microscopy: developments and applications* (Academic Press, 1996).

[109]N. J. Everall, "Confocal raman microscopy: why the depth resolution and spatial accuracy can be much worse than you think", Applied Spectroscopy **54**, 1515–1520 (2000).

[110]R. H. Webb, "Confocal optical microscopy", Reports on Progress in Physics **59**, 427 (1996).

[111]M. E. Samberg, S. J. Oldenburg, and N. A. Monteiro-Riviere, "Evaluation of silver nanoparticle toxicity in skin in vivo and keratinocytes in vitro", Environmental health perspectives **118**, 407 (2010).

[112]P. G. Etchegoin and E. Le Ru, "A perspective on single molecule sers: current status and future challenges", Physical Chemistry Chemical Physics **10**, 6079–6089 (2008).

[113]W Grochala, A Kudelski, and J Bukowska, "Anion-induced charge-transfer enhancement in and spectra of on a sers serrs rhodamine 6g silver electrode: how important is it?", J. Raman Spectrosc **29**, 681–685 (1998).

[114]R. C. Maher, L. Cohen, and P Etchegoin, "Single molecule photo-bleaching observed by surface enhanced resonant raman scattering (serrs)", Chemical physics letters **352**, 378–384 (2002).

[115]R. W. Taylor, T.-C. Lee, O. A. Scherman, R. Esteban, J. Aizpurua, F. M. Huang, J. J. Baumberg, and S. Mahajan, "Precise subnanometer plasmonic junctions for sers within gold nanoparticle assemblies using cucurbit [n] uril ãăijglueâăi", ACS nano **5**, 3878–3887 (2011).

[116]S. Kasera, F. Biedermann, J. J. Baumberg, O. A. Scherman, and S. Mahajan, "Quantitative sers using the sequestration of small molecules inside precise plasmonic nanoconstructs", Nano letters **12**, 5924–5928 (2012).

[117]S. Lal, J. H. Hafner, N. J. Halas, S. Link, and P. Nordlander, "Noble metal nanowires: from plasmon waveguides to passive and active devices", Accounts of chemical research **45**, 1887–1895 (2012).

[118]L. Tong, M. Righini, M. U. Gonzalez, R. Quidant, and M. Kall, "Optical aggregation of metal nanoparticles in a microfluidic channel for surface-enhanced raman scattering analysis", Lab Chip **9**, 193–195 (2009).

[119]P. P. Patra and G. P. Kumar, "Single-molecule surface-enhanced raman scattering sensitivity of ag-core au-shell nanoparticles: revealed by bi-analyte method", The journal of physical chemistry letters **4**, 1167–1171 (2013).

[120]M Ploschner, T Cizmar, M Mazilu, A Di Falco, and K Dholakia, "Bidirectional optical sorting of gold nanoparticles", Nano letters **12**, 1923–1927 (2012).

[121]K. Wang, E. Schonbrun, and K. B. Crozier, "Propulsion of gold nanoparticles with surface plasmon polaritons: evidence of enhanced optical force from near-field coupling between gold particle and gold film", Nano letters **9**, 2623–2629 (2009).

[122]A Cuche, A Canaguier-Durand, E Devaux, J. Hutchison, C Genet, and T. Ebbesen, "Sorting nanoparticles with intertwined plasmonic and thermo-hydrodynamical forces", Nano letters **13**, 4230–4235 (2013).

[123]V Garces-Chavez, R Quidant, P. Reece, G Badenes, L Torner, and K Dholakia, "Extended organization of colloidal microparticles by surface plasmon polariton excitation", Physical Review B **73**, 085417 (2006).

[124]J. S. Donner, G. Baffou, D. McCloskey, and R. Quidant, "Plasmon-assisted optofluidics", Acs nano **5**, 5457–5462 (2011).

[125]P. Aravind and H. Metiu, "Use of a perfectly conducting sphere to excite the plasmon of a flat surface. 1. calculation of the local field with applications to surface-enhanced spectroscopy", The Journal of Physical Chemistry **86**, 5076–5084 (1982).

[126]P. Aravind, R. Rendell, and H. Metiu, "A new geometry for field enhancement in surface-enhanced spectroscopy", Chemical Physics Letters **85**, 396–403 (1982).

[127]J. J. Mock, R. T. Hill, A. Degiron, S. Zauscher, A. Chilkoti, and D. R. Smith, "Distance-dependent plasmon resonant coupling between a gold nanoparticle and gold film", Nano letters **8**, 2245–2252 (2008).

[128]J. J. Mock, R. T. Hill, Y.-J. Tsai, A. Chilkoti, and D. R. Smith, "Probing dynamically tunable localized surface plasmon resonances of film-coupled nanoparticles by evanescent wave excitation", Nano letters **12**, 1757–1764 (2012).

[129]S. Mubeen, S. Zhang, N. Kim, S. Lee, S. KraÌĺmer, H. Xu, and M. Moskovits, "Plasmonic properties of gold nanoparticles separated from a gold mirror by an ultrathin oxide", Nano letters **12**, 2088–2094 (2012).

[130]A. Farhang, N. Bigler, and O. J. Martin, "Coupling of multiple lsp and spp resonances: interactions between an elongated nanoparticle and a thin metallic film", Optics letters **38**, 4758–4761 (2013).

[131]L. Li, T. Hutter, U. Steiner, and S. Mahajan, "Single molecule sers and detection of biomolecules with a single gold nanoparticle on a mirror junction", Analyst **138**, 4574–4578 (2013).

[132]S.-Y. Chen, J. J. Mock, R. T. Hill, A. Chilkoti, D. R. Smith, and A. A. Lazarides, "Gold nanoparticles on polarizable surfaces as raman scattering antennas", ACS nano **4**, 6535–6546 (2010).

[133]P. B. Johnson and R.-W. Christy, "Optical constants of the noble metals", Physical review B **6**, 4370 (1972).

[134]A Rida and M. Gijs, "Manipulation of self-assembled structures of magnetic beads for microfluidic mixing and assaying", Analytical chemistry **76**, 6239–6246 (2004).

[135]A. Jahn, W. N. Vreeland, M. Gaitan, and L. E. Locascio, "Controlled vesicle self-assembly in microfluidic channels with hydrodynamic focusing", Journal of the American Chemical Society **126**, 2674–2675 (2004).

[136]H. Lee, A. M. Purdon, V. Chu, and R. M. Westervelt, "Controlled assembly of magnetic nanoparticles from magnetotactic bacteria using microelectromagnets arrays", Nano letters **4**, 995–998 (2004).

[137]L. Huang, S. J. Maerkl, and O. J. Martin, "Integration of plasmonic trapping in a microfluidic environment", Optics express **17**, 6018–6024 (2009).

[138]H. Hwang and J.-K. Park, "Optoelectrofluidic manipulation of nanoparticles and biomolecules", Advances in OptoElectronics **2011** (2011).

[139]J. Kim, "Joining plasmonics with microfluidics: from convenience to inevitability", Lab on a Chip **12**, 3611–3623 (2012).

[140]O. D. Velev and K. H. Bhatt, "On-chip micromanipulation and assembly of colloidal particles by electric fields", Soft Matter **2**, 738–750 (2006).

[141]B. Gong, X. Zhao, Z. Pan, S. Li, X. Wang, Y. Zhao, and C. Luo, "A visible metamaterial fabricated by self-assembly method", Scientific reports **4** (2014).

[142]N. I. Zheludev, "A roadmap for metamaterials", Optics and Photonics News **22**, 30–35 (2011).

[143]J. Dintinger, S. Muehlig, C. Rockstuhl, and T. Scharf, "A bottom-up approach to fabricate optical metamaterials by self-assembled metallic nanoparticles", Optical Materials Express **2**, 269–278 (2012).

[144]S Muhlig, C Rockstuhl, V Yannopapas, T Burgi, N Shalkevich, and F Lederer, "Optical properties of a fabricated self-assembled bottom-up bulk metamaterial", Optics express **19**, 9607–9616 (2011).

[145]J. A. Fan, C. Wu, K. Bao, J. Bao, R. Bardhan, N. J. Halas, V. N. Manoharan, P. Nordlander, G. Shvets, and F. Capasso, "Self-assembled plasmonic nanoparticle clusters", science **328**, 1135–1138 (2010).

[146]S. Muhlig, A. Cunningham, J. Dintinger, T. Scharf, T. Burgi, F. Lederer, and C. Rockstuhl, "Self-assembled plasmonic metamaterials", Nanophotonics **2**, 211–240 (2013).

[147]Q. Liu, Y. Cui, D. Gardner, X. Li, S. He, and I. I. Smalyukh, "Self-alignment of plasmonic gold nanorods in reconfigurable anisotropic fluids for tunable bulk metamaterial applications", Nano letters **10**, 1347–1353 (2010).

[148]G. Volpe, R. Quidant, G. Badenes, and D. Petrov, "Surface plasmon radiation forces", Physical review letters **96**, 238101 (2006).

[149]A. Ashkin, J. Dziedzic, J. Bjorkholm, and S. Chu, "Observation of a single-beam gradient force optical trap for dielectric particles", Optics letters **11**, 288–290 (1986).

[150]R. Agarwal, K. Ladavac, Y. Roichman, G. Yu, C. Lieber, and D. Grier, "Manipulation and assembly of nanowires with holographic optical traps", Optics Express **13**, 8906–8912 (2005).

[151]O. M. Marago, P. H. Jones, P. G. Gucciardi, G. Volpe, and A. C. Ferrari, "Optical trapping and manipulation of nanostructures", Nature nanotechnology **8**, 807–819 (2013).

[152]D. G. Grier, "A revolution in optical manipulation", Nature **424**, 810–816 (2003).

[153]A. S. Urban, S. Carretero-Palacios, A. A. Lutich, T. Lohmuller, J. Feldmann, and F. Jackel, "Optical trapping and manipulation of plasmonic nanoparticles: fundamentals, applications, and perspectives", Nanoscale **6**, 4458–4474 (2014).

[154]J. R. Moffitt, Y. R. Chemla, S. B. Smith, and C. Bustamante, "Recent advances in optical tweezers", Biochemistry **77**, 205 (2008).

[155]Z. Yan, J. Sweet, J. E. Jureller, M. J. Guffey, M. Pelton, and N. F. Scherer, "Controlling the position and orientation of single silver nanowires on a surface using structured optical fields", ACS nano **6**, 8144–8155 (2012).

[156]Z. Yan, M. Pelton, L. Vigderman, E. R. Zubarev, and N. F. Scherer, "Why single-beam optical tweezers trap gold nanowires in three dimensions", ACS nano **7**, 8794–8800 (2013).

[157]Z. Yan, J. E. Jureller, J. Sweet, M. J. Guffey, M. Pelton, and N. F. Scherer, "Three-dimensional optical trapping and manipulation of single silver nanowires", Nano letters **12**, 5155–5161 (2012).

[158]O. Brzobohatỳ, M. Šiler, J. Trojek, L. Chvátal, V. Karásek, A. Paták, Z. Pokorná, F. Mika, and P. Zemánek, "Three-dimensional optical trapping of a plasmonic nanoparticle using low numerical aperture optical tweezers", Scientific reports **5** (2015).

[159]K. Wang and K. B. Crozier, "Plasmonic trapping with a gold nanopillar", ChemPhysChem **13**, 2639–2648 (2012).

[160]W. Zhang, L. Huang, C. Santschi, and O. J. Martin, "Trapping and sensing 10 nm metal nanoparticles using plasmonic dipole antennas", Nano letters **10**, 1006–1011 (2010).

[161]Y. Zhang, J. Wang, J. Shen, Z. Man, W. Shi, C. Min, G. Yuan, S. Zhu, H. P. Urbach, and X. Yuan, "Plasmonic hybridization induced trapping and manipulation of a single au nanowire on a metallic surface", Nano letters **14**, 6430–6436 (2014).

[162]K. Wang, E. Schonbrun, P. Steinvurzel, and K. B. Crozier, "Trapping and rotating nanoparticles using a plasmonic nano-tweezer with an integrated heat sink", Nature communications **2**, 469 (2011).

[163]C. Min, Z. Shen, J. Shen, Y. Zhang, H. Fang, G. Yuan, L. Du, S. Zhu, T. Lei, and X. Yuan, "Focused plasmonic trapping of metallic particles", Nature communications **4** (2013).

[164]M. L. Juan, M. Righini, and R. Quidant, "Plasmon nano-optical tweezers", Nature Photonics **5**, 349–356 (2011).

[165]R. Chikkaraddy, D. Singh, and G. P. Kumar, "Plasmon assisted light propagation and raman scattering hot-spot in end-to-end coupled silver nanowire pairs", Applied Physics Letters **100**, 043108 (2012).

[166]G. P. KUMAR, D. Singh, P. P. Patra, and A. Dasgupta, "Subwavelength propagation and localization of light using surface plasmons: a brief perspective", Pramana **82**, 59–70 (2014).

[167]A. Dasgupta, D. Singh, S. Tandon, R. P. Tripathi, and G. P. Kumar, "Remote-excitation surface-enhanced raman scattering with counter-propagating plasmons: silver nanowire-nanoparticle system", Journal of Nanophotonics **8**, 083899–083899 (2014).

[168]A. V. Zayats, I. I. Smolyaninov, and A. A. Maradudin, "Nano-optics of surface plasmon polaritons", Physics reports **408**, 131–314 (2005).

[169]K. Toussaint, M Liu, M Pelton, J Pesic, M. Guffey, P Guyot-Sionnest, and N. Scherer, "Plasmon resonance-based optical trapping of single and multiple au nanoparticles", Optics express **15**, 12017–12029 (2007).

[170]T. Shoji and Y. Tsuboi, "Plasmonic optical tweezers toward molecular manipulation: tailoring plasmonic nanostructure, light source, and resonant trapping", The journal of physical chemistry letters **5**, 2957–2967 (2014).

[171]P. P. Patra, R. Chikkaraddy, R. P. Tripathi, A. Dasgupta, and G. P. Kumar, "Plasmofluidic single-molecule surface-enhanced raman scattering from dynamic assembly of plasmonic nanoparticles", Nature communications **5** (2014).

[172]Y. Sun, Y. Yin, B. T. Mayers, T. Herricks, and Y. Xia, "Uniform silver nanowires synthesis by reducing agno3 with ethylene glycol in the presence of seeds and poly (vinyl pyrrolidone)", Chemistry of Materials **14**, 4736–4745 (2002).

[173]P. M. Bendix, S. N. S. Reihani, and L. B. Oddershede, "Direct measurements of heating by electromagnetically trapped gold nanoparticles on supported lipid bilayers", ACS nano **4**, 2256–2262 (2010).

[174]N. J. Hogan, A. S. Urban, C. Ayala-Orozco, A. Pimpinelli, P. Nordlander, and N. J. Halas, "Nanoparticles heat through light localization", Nano letters **14**, 4640–4645 (2014).

[175]M. D. Sonntag, J. M. Klingsporn, A. B. Zrimsek, B. Sharma, L. K. Ruvuna, and R. P. Van Duyne, "Molecular plasmonics for nanoscale spectroscopy", Chemical Society Reviews **43**, 1230–1247 (2014).

[176]S. Lal, S. Link, and N. J. Halas, "Nano-optics from sensing to waveguiding", Nature photonics **1**, 641–648 (2007).

[177]S. S. Acimovic, M. P. Kreuzer, M. U. González, and R. Quidant, "Plasmon near-field coupling in metal dimers as a step toward single-molecule sensing", Acs Nano **3**, 1231–1237 (2009).

[178]F. Kulzer and M. Orrit, "Single-molecule optics", Annu. Rev. Phys. Chem. **55**, 585–611 (2004).

[179]W. Moerner, "A dozen years of single-molecule spectroscopy in physics, chemistry, and biophysics", The Journal of Physical Chemistry B **106**, 910–927 (2002).

[180]S. Nie and R. N. Zare, "Optical detection of single molecules", Annual review of biophysics and biomolecular structure **26**, 567–596 (1997).

[181]T Tachikawa and T Majima, "Single-molecule fluorescence imaging techniques for the detection of reactive oxygen species", Modern Research and Educational Topics in Microscopy, Spain: Formatex, 651–659 (2007).

[182]Y. Chen, W. Chen, and E Burstein, "Surface-electromagnetic-wave-enhanced raman scattering by overlayers on metals", Physical Review Letters **36**, 1207 (1976).

[183]M Futamata, P Borthen, J Thomassen, D Schumacher, and A Otto, "Application of an atr method in raman spectroscopy", Applied spectroscopy **48**, 252–260 (1994).

[184]S. A. Meyer, E. C. Le Ru, and P. G. Etchegoin, "Combining surface plasmon resonance (spr) spectroscopy with surface-enhanced raman scattering (sers)", Analytical chemistry **83**, 2337–2344 (2011).